AD_______________

Award Number: W81XWH-04-1-0190

TITLE: Magnetic Resonance Spectroscopy: An Objective Technique for the Quantification of Prostate Cancer Pathologies

PRINCIPAL INVESTIGATOR: Leo L. Cheng, Ph.D.

CONTRACTING ORGANIZATION: Massachusetts General Hospital
Boston, Massachusetts 02114-2698

REPORT DATE: February 2005

TYPE OF REPORT: Annual

PREPARED FOR: U.S. Army Medical Research and Materiel Command
Fort Detrick, Maryland 21702-5012

DISTRIBUTION STATEMENT: Approved for Public Release;
Distribution Unlimited

REPORT DOCUMENTATION PAGE

Form Approved
OMB No. 074-0188

1. AGENCY USE ONLY ***(Leave blank)***	***2. REPORT DATE*** February 2005	***3. REPORT TYPE AND DATES COVERED*** Annual (12 Jan 2004 - 11 Jan 2005)

4. TITLE AND SUBTITLE
Magnetic Resonance Spectroscopy: An Objective Technique for the Quantification of Prostate Cancer Pathologies

5. FUNDING NUMBERS
W81XWH-04-1-0190

6. AUTHOR(S)
Leo L. Cheng, Ph.D.

7. PERFORMING ORGANIZATION NAME(S) AND ADDRESS(ES)
Massachusetts General Hospital
Boston, Massachusetts 02114-2698

E-Mail: cheng@nmr.mgh.harvard.edu

8. PERFORMING ORGANIZATION REPORT NUMBER

9. SPONSORING / MONITORING AGENCY NAME(S) AND ADDRESS(ES)
U.S. Army Medical Research and Materiel Command
Fort Detrick, Maryland 21702-5012

10. SPONSORING / MONITORING AGENCY REPORT NUMBER

11. SUPPLEMENTARY NOTES

12a. DISTRIBUTION / AVAILABILITY STATEMENT
Approved for Public Release; Distribution Unlimited

12b. DISTRIBUTION CODE

13. ABSTRACT (Maximum 200 Words)

In the past year, since the activation of the award, according to our proposed Statement of Work, we devoted our efforts on the collection of specimens from prostate cancer patients, and spectroscopic and histopathological measurements of these samples for the construction of metabolic markers aimed at tumor diagnosis based on HRMAS 1HMR evaluation. Significant progress has also been achieved in these efforts. In the mean time, eight peer-reviewed publications related to the project have been either published, accepted for publication, or under revision processes. In addition, one NIH R01 grant has been submitted as a direct result of research activities supported by this award. These advancements will assist us to better understand tumor metabolism observed with MR spectroscopy, and contribute to better patient treatments in the future.

14. SUBJECT TERMS
Ex vivo magnetic resonance spectroscopy, quantitative pathology cellular metabolic markers, prostatectomy

15. NUMBER OF PAGES
116

16. PRICE CODE

17. SECURITY CLASSIFICATION OF REPORT Unclassified	***18. SECURITY CLASSIFICATION OF THIS PAGE*** Unclassified	***19. SECURITY CLASSIFICATION OF ABSTRACT*** Unclassified	***20. LIMITATION OF ABSTRACT*** Unlimited

NSN 7540-01-280-5500

Standard Form 298 (Rev. 2-89)
Prescribed by ANSI Std. Z39-18
298-102

Table of Contents

Introduction

In the past year, since the activation of the award, according to our proposed Statement of Work, we devoted our efforts on the collection of specimens from prostate cancer patients, and spectroscopic and histopathological measurements of these samples for the construction of metabolic markers aimed at tumor diagnosis based on HRMAS 1HMR evaluation. Significant progress has also been achieved in these efforts. These advancements will assist us to better understand tumor metabolism observed with MR spectroscopy.

Summary of Research Accomplishments

We will first summarize our achievements according to an overview of our proposed Statement of Work. In this summary, we will use **bold** typeface to indicate a sub-task that has been completed, and use *italic* typeface to represent the on-going efforts, and use regular typeface to list sub-tasks that have yet to start according to our proposed time line. At the end of the list of each sub-task, our related references published after the application for the award are given. Among these reference, those acknowledged this award as a grant support source are listed in **bold** typeface.

STATEMENT OF WORK

Task 1: Establish Procedures and Protocols.

A. **Comparison of HRMAS 1HMRS spectra and degradation rates of fresh tissue specimen with those obtained from snap-frozen samples from the same cases (20 specimen total).** (Appendix I)

B. **Preparation of detailed protocols for HRMAS 1HMRS examination and establishment of criteria for conducting homo- and heteronuclear correlation examinations.** (Appendices II, **IV, VI**)

C. *Evaluation of histopathological integrity of specimen after HRMAS measurement by the primary project pathologist (50 cases).* (Appendix I)

D. **Establishment of detailed protocols for quantitative histopathology and computer-aided histopathological image analysis.** (Appendix **III**)

Task 2: Establish Correlations Between MRS and Histopathology. (Specific Aim 1)

A. In Progress & Months 1-30:
Collection of prostate samples from i) 180-200 prostatectomies (among them 80-100 from African-Americans), "pseudo-biopsies" (6 tissue cores) and "permanent section" (20 samples) will be performed on removed prostate, yielding 1200-1600 samples/year), *and ii) normal controls from autopsy subjects (6 cases from each of 3 age groups, 18 cases total).*

B. In Progress & Months 1-30:
Performance of HRMAS 1HMRS analysis of i) tumor specimen, and ii) autopsy specimen. (Appendix V)

C. Months 3-33:
Histopathological quantification of tissue specimens analyzed with MRS under Task 2B. (Appendix **III**)

Task 3: Determine Metabolite Markers for Prostate Cancer. (Specific Aim 2)

A. In Progress & Months 1-18:
Establishment of metabolite profiles for different prostate zones in normal controls. (Appendix V)

B. Months 6-35:
i). Performance of multivariate analysis on MRS data to identify metabolic markers that correlate with quantitative histopathology (from Task 2C), and with clinical data;
ii). Evaluation of the sensitivity and specificity of metabolite markers for detecting the presence of cancer cells and predicting the quantity of each pathological component; (Appendix V)
iii). Evaluation of the statistical significance of metabolite markers identified by samples from both pseudo-biopsy and permanent section; examination of the sensitivity and specificity of these

markers for their ability to suggest the pathologic stage of prostate cancer by using only pseudo-biopsy samples.

C. Month 36:

Test of the sensitivity of these markers in reflecting the high disease occurrence among African-Americans; conclusion of findings and the clinical implications thereof, and the submission of final report.

Task 4: Develop a Clinically Adaptable MRS Protocol. (Specific Aim 3)

A. Months 18-30:

Identification of metabolite markers that can divide the Gleason score 5, 6(3+3) and 7(3+4) group into subgroups. (Appendix V)

B. Months 31-36:

Preliminary evaluation and modification of the database markers (from Task 4A) in connection with the updated clinical information on patient outcome, and design of a clinical protocol that can be executed, objectively, by a technician without extensive training.

Details of Key Research Accomplishments

Now, we wish to report our progress and achievements in details.

1. Collection of human prostate cancer specimens for the project.

As a translational clinical research project studying human prostate cancer, the success in our proposed tasks relays exclusively on our achievements in collecting human specimens. Without these samples, none of our proposed task can be conducted. In this aspect, we can report with satisfaction that to this date, we have already collected **642** samples, from **247** cases of prostactomies and five cases from autopsies. This activity has greatly exceeded our planed rate of samples acquisition outlined in Task 2A. Amount these samples, we have analyzed **421** samples from **173** cases with both NMR spectroscopy and quantitative pathology according to visual estimations provided by project pathologists.

2. Developments in NMR spectroscopy analysis of intact tissue samples.

Measurements of spinning spectra at reduced spinning rates. The HRMAS study of PCa proposed for the awarded project allows spectroscopy and quantitative pathology to be performed sequentially on the same tissue specimen. This permits pathological results to constitute an important parameter in establishing cancer metabolic markers. As such, any compromise to tissue pathology weakens a fundamental premise of this study. A potential source of tissue damage arises from tissue mechanical rotation performed at a high spinning rate. When the rate is reduced, however, spinning sidebands (SSB), produced primarily by tissue water resonance, severely impede metabolite observation. We have studied slow HRMAS with various SSB suppression methodologies, including rotor-synchronized DANTE, rotor-synchronized WATERGATE, 1D-TOSS, and 2D-PASS sequences. Among these, we found that the rotor-synchronized DANTE sequence at spinning rates of 600 and 700 Hz can be used for SSB suppression (Appendix II).

Recently, we further developed a novel scheme, (A+B-|A-B|), or Min(A, B), by using the smaller value of two water-suppressed spectra (A, B) of different low spinning rates to generate a sideband free spectrum. This approach works only if the following experimental conditions are fulfilled: 1) the two spectra (A and B) are obtained from the same sample, under the same experimental conditions, other than spinning rate; 2) the line-width for an individual resonance is the same (within the measurement error) in the two spectra; 3) the two spinning rates are decided, such that there are no SSB overlap points in the regions-of-interest in the two spectra; and 4) there are no negative resonances in the spectra. Therefore, without SSB, the two spectra would be nearly identical. Furthermore, compared with the DANTE method, optimized mainly for elimination of SSB from water and external standard (STD), the Min(A, B) editing procedure can produce more accurate results than the DANTE approach for cases in which, not only SSB of water and/or STD, but SSB from either cellular metabolites or other contaminants are also of concern. We will use this simplified slow-spinning method for the proposed study (Appendix **IV**).

Evaluation of Freeze-thawing Effect on Tissue Spectral Profiles. Some researchers have speculated that improvement in the spectral resolution of intact tissue with HRMAS is due in part to freeze-thawing artifacts resulting from tissue storage, as discussed in a rodent renal cortex study. Since its publication, a number of studies have cited the findings as a concern and have evaluated the issue. We analyzed 12 human prostate tissue specimens on a 600 MHz spectrometer at 3°C with the previously discussed DANTE method, at HRMAS rates of 600 and 700 Hz. One sample from each specimen was measured fresh and another thawed, following 12-16 hours of freezing. In addition, we measured one sample from each specimen first fresh, then freeze-thawed. The spectral resolutions represented by line-widths and obtained from fresh and frozen samples were identical for most metabolites. Although metabolite intensities from fresh and freeze-thawed spectra were not identical, the differences were less drastic than those reported in the rodent study (Appendix I).

Quantification of HRMAS Spectra with an External Standard. Using the intensity of the external STD in the sample rotor, we were able to linearly correlate sample weights of a metabolite agarose gel-solution with the relative spectral intensity of [metabolites]/[STD]. Further, using this gel-solution, we were able to linearly correlate the relative intensity with the estimated metabolite concentration. This linear relationship is critical for the use of STD in the estimation of metabolite concentrations in intact tissue from spectra for which water presaturation is applied to improve the detectability of endogenous metabolites. This linear relationship allowed us to estimate the measured metabolite concentrations at both 600Hz and 3kHz spinning rates for human prostate tissues, based on their relative intensities (/[STD]) from water presaturated spectra. Since these linear regressions were constructed with the 3.0 kHz data on the horizontal, and the Min(A, B) results on the vertical axis, if the Min(A, B) value of a particular metabolite is identical to that measured at 3.0 kHz, the slope of the linear regression will be 1 and the intercept, 0. Alternately, a slope less than 1 indicates that the integrated intensity of the metabolite measured at 3 kHz has a higher value than that determined with Min(A, B) at 600-700 Hz. For almost all evaluated metabolites, higher apparent concentrations were observed under the 3.0 kHz measurement conditions. This was not surprising, because it is widely acknowledged that an increase in spinning rate can potentially increase the observable amount of a metabolite, effected by the minimization of bulk magnetic susceptibility effects and other physical, environmental effects, such as viscosity. However, this should not affect the diagnostic ability of tissue metabolic profiles, as long as the database profiles and the case measurements were acquired at the same spinning rate (Appendix IV).

3. Developments in quantitative pathology analysis of tissue after NMR analysis.

Computer-aided Image Analysis (CAIA) on Prostate Tissue After Spectroscopy Analysis. The success of our aims to develop a biochemistry-based pathology standard for PCa relies heavily on the establishment of a 1:1 relationship between tissue metabolites readily quantifiable through HRMAS 1HMRS and quantitative pathology features residing in a sample. This places a great demand on the accuracy of quantitative histopathology. Recently, we developed a CAIA protocol for H/E stained prostate tissues with the assistance of an Olympus BX41 Microscope Imaging System in conjunction with image analyzer MicroSuite™ (Soft Imaging System Corp., Lakewood, CO). **Figure 1** shows an example of the CAIA classification scheme performed on a cross-section of human prostate tissue containing both normal and cancerous glands. Stroma, normal glandular epithelium (red), and normal glandular lumen (yellow) were particularly evident in (b). Image (c) shows the result of cancer cells and lumen, in blue and light blue, respectively.

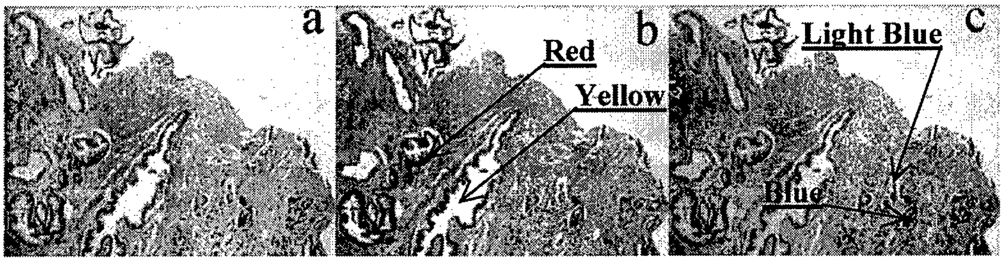

Figure 1. Identification of (b) normal epithelial glands and lumens and (c) cancer glands and lumens with the CAIA protocol.

With this protocol, we analyzed thirty-eight samples from 29 prostatectomy cases that had been studied with HRMAS 1HMRS. After spectroscopy analysis, samples were serial-sectioned, stained and visually assessed by pathologists. Cross-sections from these samples were then measured with the CAIA protocol. Results showed that human visual assessments overestimated the area percentages of tissue pathologies. Statistically significant correlations were found between both metabolites indicative of normal epithelium and those indicative of PCa and the CAIA quantitative results. CAIA based quantitative pathology proved to be more accurate than human visual assessment in establishing correlations useful for disease diagnosis between prostate pathology and metabolic concentrations (Appendix III).

4. Progress in the proposed project.

Analysis of Prostate Metabolic Profiles with Principal Component Analysis. To date, we have collected and incorporated more than 160 surgical cases (~350 specimens) into our study. From these specimens, we have measured ~300 samples with HRMAS 1HMRS, and finished preliminary quantitative pathology. We have used the above introduced DANTE slow-spinning (600, 700 Hz) scheme in a study of 199 samples from 82 cases. For each sample, the fractions containing the most commonly observed pathological features of PCa – normal-looking epithelium, cancer and stroma – were recorded.

The 36 most intense resonance peaks/groups assigned to specific metabolites were subjected to Principal Component Analysis (PCA), and all components with eigenvalues greater than 0.5 (PC1 to PC15) were examined (see **Table 1**), which included each eigenvalue as a percent of the total variability (36) for the 36 standardized metabolite resonances, as well as the cumulative percent of variation represented by this and all previous PCs. It is clear from this table that the 15 components can account for more than 88% of variation for the 36 resonances. Linear regression analysis of the three measured pathology features vs. the PCs revealed that the 2nd and 13th/14th PCs are positively correlated with the fraction of normal epithelium and cancer, respectively. The correlations (r) and their p-values are listed in Table 1.

	EigenValue	Percent	CumPercent	Epithelium (r, p)		Cancer (r, p)		Stroma (r, p)	
PC1	9.7438	27.066	27.066	0.2322	0.0010	0.0438	0.5392	-0.2216	.00017
PC2	**5.9318**	**16.477**	43.543	**0.3813**	**<0.0001**	-0.0166	0.8163	**-0.3033**	**<0.0001**
PC3	2.9470	8.1861	51.729	0.0962	0.1767	0.0335	0.6380	-0.1023	0.1503
PC4	2.5294	7.0260	58.755	-0.0701	0.3255	-0.0913	0.1997	0.1204	0.0903
PC5	1.6851	4.6809	63.436	-0.0377	0.5968	-0.0843	0.2363	0.0889	0.2116
PC6	1.4127	3.9242	67.360	-0.0036	0.9602	0.095	0.1819	-0.0681	0.3393
PC7	1.3347	3.7075	71.068	-0.0203	0.7756	0.1368	0.0540	-0.077	0.2795
PC8	1.2062	3.3506	74.419	-0.1156	0.1039	0.0548	0.4424	0.0579	0.4169
PC9	1.0260	2.8501	77.269	0.057	0.4235	-0.2202	0.0018	0.1039	0.1442
PC10	0.85141	2.3650	79.634	-0.0355	0.6191	-0.1175	0.0984	0.1098	0.1226
PC11	0.78303	2.1751	81.809	-0.139	0.0503	-0.0034	0.9616	0.117	0.0998
PC12	0.71392	1.9831	83.792	-0.1536	0.0303	0.1022	0.1508	0.0567	0.4267
PC13	**0.67150**	**1.8653**	85.657	0.0652	0.3599	**0.1457**	**0.0401**	**-0.1537**	**0.0302**
PC14	**0.55362**	**1.5378**	87.195	-0.1302	0.0668	**-0.1597**	**0.0243**	**0.2169**	**0.0021**
PC15	0.50906	1.4141	88.609	0.063	0.3768	-0.0922	0.1954	0.0112	0.8751

Table 1. Results of PCA for the first 8 PCs on intensities of 40 resonances from 190 prostate tissue specimens. Percent: each eigenvalue as a percent of the total eigenvalue; CumPercent: the cumulative percent of variation represented by this and all the previous PCs. For Epithelium, Cancer and Stroma columns: numbers are correlation r and p values.

The apparent difference in the correlations (0.38 and 0.15 for epithelium with PC2 and cancer with PC13/14, respectively) may be a result of the relative sample sizes. Varying fractions of epithelium were observed in 174 samples, while cancer cells were detected for only 20/199 samples. This could also account for the difference between the two eigenvalues, of which PC2 (epithelium) represents 16.5% of the total variability, while PC13/14 (cancer) only 1.9%/1.5%. PC1 reflects mostly the total resonance intensities.

Prostate Zones and Metabolite Differences. We have acquired multiple tissue samples from different zones of surgically removed prostates. In fact, the PCA results described in the last section can be used to analyze possible zone-related metabolite differences, using one-way ANOVA evaluations of PC2 (epithelium) for samples from different zones. Among the 179 cancer-negative samples, 49 were from the central zone (CZ), 59 from the peripheral zone (PZ), and 55 from the transition zone (TZ). In **Figure 2**, our results for PC2 show that there are measurable differences in epithelial metabolic profiles between TZ and CZ, as well as between TZ and PZ. No differences were detected between CZ and PZ. However, since PC2 was positively correlated with the vol% of normal epithelium (Table 1), our results seem to indicate that the zone-differentiating capability of PC2 may reflect the differences of epithelial content in the measured groups (see **Figure 3**).

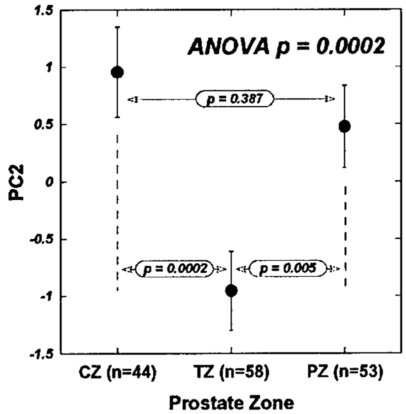

Figure 2. PC2 detects significant epithelium related differences between prostate zones: TZ vs. CZ, TZ vs. PZ.

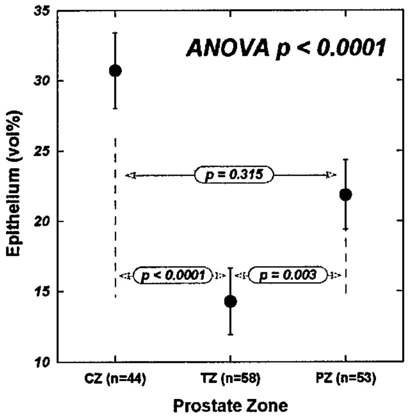

Figure 3. Epithelium differences among the measured samples of different prostate zones.

Identification of Cancer Containing Samples with Metabolic Profiles. By examining the eigenvectors (i.e. the coefficients in the linear combinations of the original metabolites predicting each component) for PC2, it was found that PC2 is associated with above average levels of inositols, spermine, creatine, and citrate, all of which are associated with epithelial cells. Similar examination of PC13/14 revealed their association with above average levels of taurine, PCh, choline, and lipids, and below average levels of inositols, citrate, and valine. This observation agrees with common knowledge of tumor metabolism. The sensitivity of correlations between PCs and pathological features relies on the collective variation of a number of metabolites. Nevertheless, the sensitivities of the individual metabolites depicted by their eigenvectors of PC13/14 as cancer-correlated were tested with paired Student's t-tests for differentiating cancer from non-cancerous tissues, obtained from the same 13 surgical cases. Results indicate that PCh, choline and lactate can distinguish cancer from non-cancer with statistical significance (**Figure 4**).

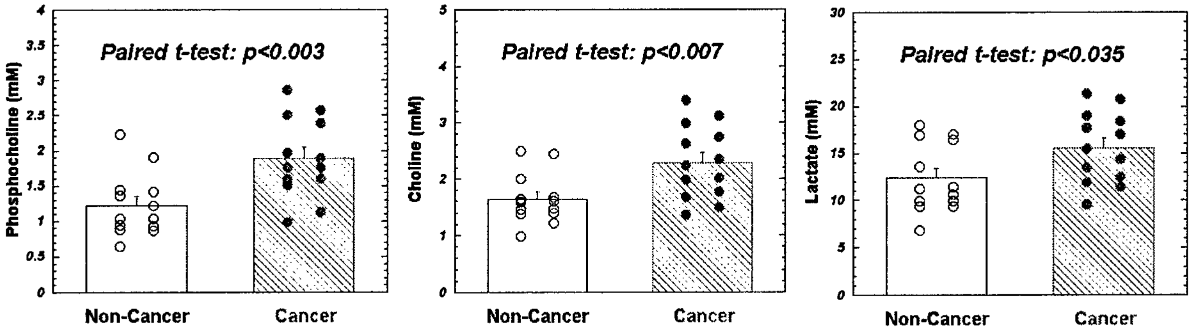

Figure 4. Metabolite concentrations of PCh and choline, suggested by PC13/14 to be cancer correlated, as well as of lactate, can differentiate cancer from non-cancer tissue obtained from the same patients by using paired Student's t-test.

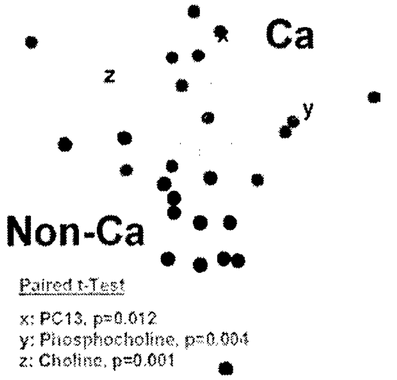

Figure 5. 3D plot of Principal Component 13 (PC13) vs. phosphocholine vs. choline. Cancerous and non-cancerous tissue samples from 13 patients can be separated in a projection of this 3D plot. PC13 correlates with vol% of PCa in tissue. The paired Student's t-test (cancer vs. non-cancer from the same patients) results are listed in the figure.

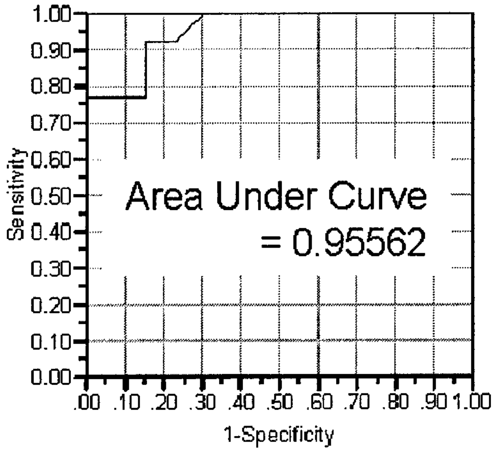

Figure 6. A ROC curve for the vertical direction of the 2D projection of Figure 8.

Furthermore, we can separate cancerous from non-cancerous samples using a 2D projection of a 3D (**Figure 5**) of PC13 (x-axis) vs. phosphocholine (y-axis) and choline (z-axis). An ROC (receiver operating characteristic) curve for the vertical direction of the 2D projection revealed overall 95.6% accuracy, shown in **Figure 6**.

Correlating Patient Serum PSA Levels with Metabolic Profiles. From the 82 prostatectomy cases studied, we identified 59 cases for which results of patients' serum PSA tests prior to surgeries were available. Among these cases, 111 non-cancerous tissue samples from different prostate zones (central, transitional, and peripheral, with no more than one sample per each zone for each case) were identified. We evaluated the relationship between PSA levels and tissue metabolic profiles and found that PC2 was linearly correlated, with statistical significance, to PSA results as shown in **Figure 7**. Since, as we previously presented, PC2 is linearly correlated with the vol% of non-cancerous epithelial cells, we verified that there was no coincidental correlation between PSA levels and epithelial vol% among these measured samples.

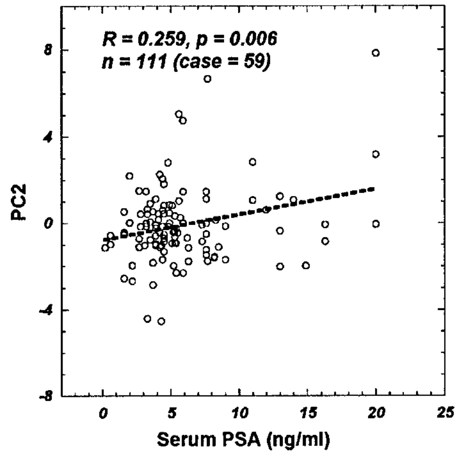

Figure 7. Statistically significant correlation between patient serum PSA levels before prostatectomy and metabolic profiles represented by PC2 measured from 111 cacner-absent prostate tissue samples from 59 prostatectomy cases of PCa.

Metabolic Profiles Are More Sensitive Than Histopathology. Morphological changes of cancer cells represent the last step in a cascade of genetic and molecular transformations of malignancy. These structural transformations are accompanied, and even preceded by, various metabolic variations. Since metabolites reflect disease-related biochemical activity, it may precede noticeable morphological presentations of disease. Thus, the measurement of metabolic profiles will provide more sensitive and earlier information than can be achieved by approaches that rely on changes in cellular morphology. This conceptual framework, based on accepted principles of oncology and tumor biology, has been the strongest motivation for our research efforts, as well as for many of our colleagues and predecessors. Previously, we considered the above assumptions intuitively reasonable; now, we can provide preliminary experimental evidence to support their validity.

We examined correlations between PCs and pathological tumor stage [AJCC/TNM staging system (6th ed.)]. With all samples included (n=199), we observed the following with statistical significance: PC2 can differentiate T2c cancer (prostate-confined; both lobes) from T3 (invading extraprostatic tissue) and T2ab (prostate-confined; one lobe). PC5 (reflects changes in lactate, choline, inositol, lipids, etc.) can differentiate T2ab cancer from T2c and T3 (**Figures 8a** and **b**). PC2 correlates with vol% of epithelium, verifying that observed differentiation among tumor stages was independent of epithelial content (e.g. T2ab: 21.88±2.59%; T2c: 20.21±1.91%). Upon analysis of samples (n=179) defined as "cancer-absent" according to histopatholgy, similar differentiations persisted for both PCs (**Figures 8c** and **d**). Furthermore, when the same PCs were applied to cancer-absent samples of GS 6 and 7 (n=162), both PCs distinguished the least aggressive tumor (i.e. GS 6 and T2ab tumors) from those in more aggressive groups (GS 6 T2c, GS 6 T3, and GS 7 tumors) (**Figures 8e** and **f**). For the last group, the ROC curve analysis of PC5 indicated that the overall accuracy (area under the curve, AUC) for identifying (GS6, T2ab) tumors (n=42) from (GS6, T2c), (GS6, T3) and (GS7) tumors (n=120) was 65.4%. By further restricting the ROC analysis to include only samples from patients of PSA levels ≤10.0 ng/ml (n=95), the AUC level increased to 71.5% (**Figure 9**). These AUC levels were very close to current literature values (62.7-73.8%) in predictions of patient pathological stages with Gleason scores at biopsy based on large patient populations (from 114 to 1283).

It is of note that, in contrast to published works relying on observation and evaluation of cancer cells in specimens, our results are based on chemical analyses of histopathologically-defined "cancer-absent" tissues from PCa patients.

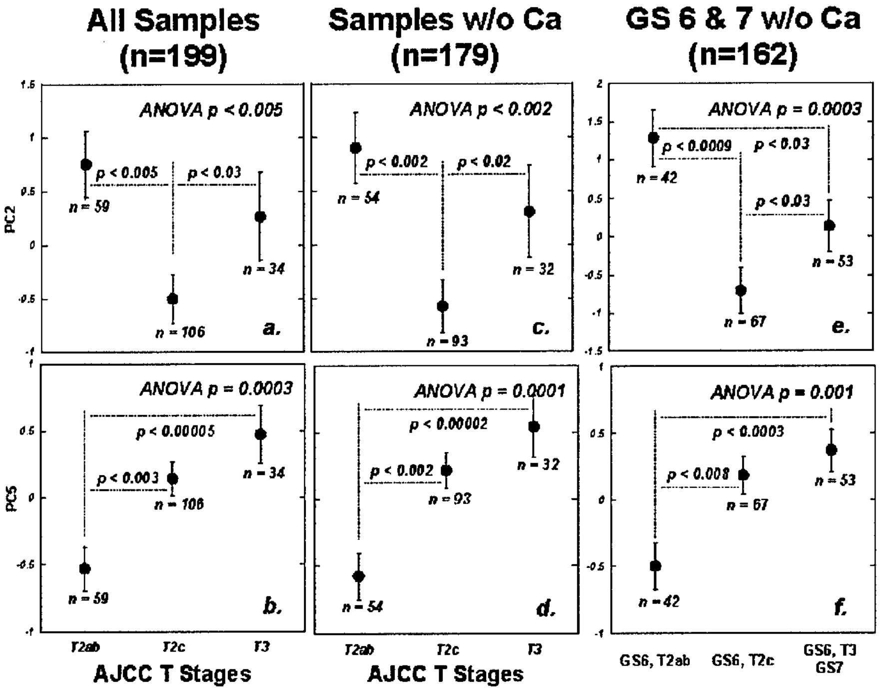

Figure 8. Principal Component 2 (PC2) and Principal Component 5 (PC5) as predictors of tumor stage: (**a.**) PC2 can differentiate T2c stage tumors from T2ab and T3 tumors as defined by AJCC/TNM staging system (6th ed.) with all samples analyzed; while (**b.**) PC5 can differentiate T2ab from T2c and T3 stages. Similar capabilities exist with cancer-absent samples (**c**, **d**), "*w/o Ca*" *indicating no cancer cells detected by histopathology*; and with cancer absent GS 6 and 7 samples (**e**, **f**). In the latter, PC2 and PC5 can differentiate among three tumor groups: 1) GS 6, T2ab, 2) GS 6, T2c, and 3) GS 6, T3 plus GS 7 tumors.

In addition to the pathological stages, we noticed that, although not yet incorporated in AJCC/TMN staging, tumor perineural invasion (TPNI) indicates prostate tumor aggressiveness and therefore may inform treatment. Unfortunately, tumor heterogeneity may prevent visualization of invasion in biopsy samples. Our evaluation yielded a statistically significant correlation between PC14 levels and TPNI status for all samples (n=199) (**Figure 10a**), the 179 cancer-absent samples (**Figure 10b**), and more interestingly, the 42 cancer-absent samples from GS 6/T2ab tumors (**Figure 10c**). This last observation, combined with results shown in Figures 11e, and f may have great clinical significance in identifying and managing less aggressive GS 6 tumors.

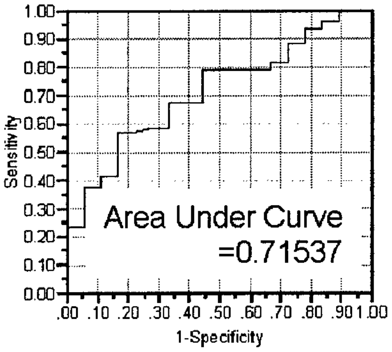

Figure 9. An ROC curve identifying (GS6, T2ab) tumors for PSA ≤10.0 ng/ml patients.

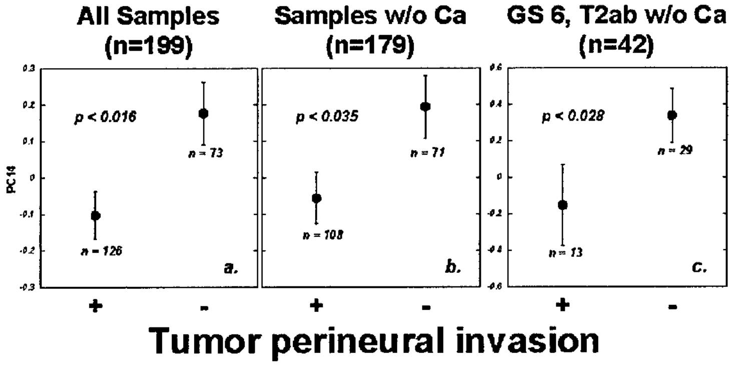

Figure 10. Principal Component 14 (PC14) as a predictor for TPNI. PC14, linearly correlated with volume % of cancer cells in tissue samples, can predict TPNI status with statistical significance particularly among GS 6 and T2ab samples (c).

Parts of the above reported results have been included in a manuscript that has been accepted for publication in Cancer Research as a Priority Report (Appendix V).

Reportable Outcome

Publications:

Since our application of the reported award, in direct relation to the proposed project, we have published three articles:

1. Taylor JL, Wu CL, Cory D, Gonzalez RG, Bielecki A, Cheng LL. High-resolution magic angle spinning proton NMR analysis of human prostate tissue with slow spinning rates. *Magn Reson Med* 2003;**50**:627-632.
2. Wu CL, Taylor JL, He WL, Zepeda AG, Halpern EF, Bielecki A, Gonzalez RG, Cheng LL. Proton high resolution magic angle spinning nmr analysis of fresh and previously frozen tissue of human prostate. *Magn Reson Med* 2003;**50**:1307-1311.
3. Burns MA, He W, Wu CL, Cheng LL. Qunatitative pathology in tissue MR spectroscopy based human prostate metabolomics. *Tech. Cancer Res. Treat.* 2004;**3**:591-598.

We have two more articles been accepted for publication and one manuscript under revision:

4. Burns MA, Taylor JL, Wu CL, Zepeda AG, Bielecki A, Cory D, Cheng LL. Reduction of spinning sidebands in proton NMR of human prostate tissue with slow high resolution magic angle spinning. *Magn Reson Med* 2005, In press.
5. Cheng LL, Burns MA, Taylor JL, He WL, Halpern EF, McDougal WS, Wu, CL. Metabolic characterization of human prostate cancer with tissue magnetic resonance spectroscopy. *Cancer Res.* 2005; In press.
6. Loening NM, Chamberlin AM, Zepeda AG, Gonzales RG, Cheng LL. Quantification of phosphocholine and glycerophosphocholine with ^{31}P edited ^{1}H NMR spectroscopy. *NMR Biomed.* Pending revision.

In addition, we have been requested to provide two peer-reviewed review articles of NMR studies of human malignancies:

7. Cheng LL, Burns MA, Lean CL. High resolution magic angle spinning (HRMAS) proton MRS of surgical specimens. Modern Magne Reson. In press.
8. Lentz MR, Taylor JL, Feldman DA, Cheng LL. Current Clinical Applications of *in vivo* Magnetic Resonance Spectroscopy and Spectroscopic Imaging. Curr Med Imag Rev. Pending.

Grant Application:

With the reported significant results, we have submitted a NIH R01 grant titled: Characterizing prostate cancer by ex vivo MRS signatures (R01CA115746). It is now in the peer-review process.

Conclusion

In the past year, we have achieved significant progress with the support of this award. Our results from our work this year further suggest that in the future we are likely to be successful with the direct testing of the hypothesis that prostate metabolic changes measured with HRMAS 1HMRS can correlate well with tumor types and grades, and thus may be used as diagnostic markers for human prostate cancer. With our achievements, we are increasingly confident that our efforts will contribute to the better understanding of prostate tumor biology, its relationship with disease diagnosis, and patient prognostication. Since our efforts and results to date have been in close agreement with our proposed Statement of Work, we do not expect any alterations from it in our research activities in the coming year.

Appendices

1. Wu CL, Taylor JL, He WL, Zepeda AG, Halpern EF, Bielecki A, Gonzalez RG, Cheng LL. Proton high resolution magic angle spinning nmr analysis of fresh and previously frozen tissue of human prostate. *Magn*

Reson Med 2003;**50**:1307-1311.

2. Taylor JL, Wu CL, Cory D, Gonzalez RG, Bielecki A, Cheng LL. High-resolution magic angle spinning proton NMR analysis of human prostate tissue with slow spinning rates. *Magn Reson Med* 2003;**50**:627-632.
3. Burns MA, He W, Wu CL, Cheng LL. Qunatitative pathology in tissue MR spectroscopy based human prostate metabolomics. *Tech. Cancer Res. Treat.* 2004;**3**:591-598.
4. Burns MA, Taylor JL, Wu CL, Zepeda AG, Bielecki A, Cory D, Cheng LL. Reduction of spinning sidebands in proton NMR of human prostate tissue with slow high resolution magic angle spinning. *Magn Reson Med* 2005, In press.
5. Cheng LL, Burns MA, Taylor JL, He WL, Halpern EF, McDougal WS, Wu, CL. Metabolic characterization of human prostate cancer with tissue magnetic resonance spectroscopy. *Cancer Res.* 2005; In press.
6. Loening NM, Chamberlin AM, Zepeda AG, Gonzales RG, Cheng LL. Quantification of phosphocholine and glycerophosphocholine with ^{31}P edited ^{1}H NMR spectroscopy. *NMR Biomed.* Pending revision.

Magnetic Resonance in Medicine 50:1307–1311 (2003)

Proton High-Resolution Magic Angle Spinning NMR Analysis of Fresh and Previously Frozen Tissue of Human Prostate

Chin-Lee Wu,[1] Jennifer L. Taylor,[1] Wenlei He,[1] Andrea G. Zepeda,[1] Elkan F. Halpern,[2] Anthony Bielecki,[3] R. Gilberto Gonzalez,[2] and Leo L. Cheng[1,2*]

The previously observed improvement in spectral resolution of tissue proton NMR with high-resolution magic angle spinning (HRMAS) was speculated to be due largely to freeze-thawing artifacts resulting from tissue storage. In this study, 12 human prostate samples were analyzed on a 14.1T spectrometer at 3°C, with HRMAS rates of 600 and 700 Hz. These samples were measured fresh and after they were frozen for 12–16 hr prior to thawing. The spectral linewidths measured from fresh and previously frozen samples were identical for all metabolites except citrate and acetate. The metabolite intensities of fresh and freeze-thawed samples depend on the quantification procedures used; however, in this experiment the differences of means were <30%. As expected, it was found that tissue storage impacts tissue quality for pathological analysis, and HRMAS conditions alone are not sufficiently destructive to impair pathological evaluation. Furthermore, although storage conditions affect absolute metabolite concentrations in NMR analysis, relative metabolite concentrations are less affected. Magn Reson Med 50:1307–1311, 2003. © 2003 Wiley-Liss, Inc.

Key words: HRMAS; proton NMR; human prostate; tissue freezing; intact tissue

Shortly after high-resolution magic angle spinning (HRMAS) was introduced for intact-tissue, ex vivo, proton NMR for biomedical research, investigators examining rodent renal cortex tissue cautioned that the improvement in spectral resolution obtained with HRMAS might be a result of artifacts due to freeze-thawing processes in tissue storage (1). They reported that a large number of cellular metabolites were only visible or had drastically increased intensities (as much as 300%) after freeze-thawing (1). Although the authors of that study did not question the contribution of HRMAS in achieving a high spectral resolution that had not been observed previously with intact tissue (regardless of the type and/or storage process used) prior to the development of HRMAS, they did bring up an issue of great clinical relevance. The authors warned that if HRMAS were to be used in clinical evaluations, any possible perturbing effect resulting from sample storage (particularly the freeze-thawing process commonly used in the research phase of preclinical studies) should be carefully evaluated. Since the publication of that initial study, a number of researchers have expressed similar concerns and have attempted to address this issue (2–4).

The physics supporting this speculation are well understood. If the freeze-thawing process alters the physical state of tissue cellular metabolites, their NMR parameters might change, and therefore their spectral profiles might be different. It is important to evaluate such potential artifacts in order to establish disease-based tissue cellular metabolite databases for future clinical use. To confirm and measure these artifacts (if they exist), and demonstrate the harmlessness of the tissue-freezing process on measurable NMR cellular metabolites, careful measurements may need to be conducted individually for each tissue type of interest.

Our interest in the study of human prostate cancer prompted us to design this study to evaluate possible freeze-thawing effects on NMR measurements of human prostate tissue.

METHODS

Tissue Protocol

For the current study, NMR analysis of human prostate surgical specimens was approved by the Institutional Review Board of the Massachusetts General Hospital. Twelve human prostate specimens were collected in the operating room during five prostatectomies, representing different prostate zones (central, transitional, and peripheral). Each specimen (~50 mg) was divided into four pieces of approximately equal size. Sample 1 was directly fixed in 10% buffered formalin for histopathology; sample 2 was snap-frozen and stored at −80°C for spectroscopy analysis the next day; and samples 3 and 4 were kept in closed vials, placed on ice, and measured by HRMAS proton NMR within 2 hr after tissue resection. After NMR analysis, sample 3 was fixed in formalin; sample 4 was frozen at −80°C for 12–16 hr, and was spectroscopically reevaluated the next day. Whenever possible, sample 4 was directly frozen in the HRMAS rotor to avoid sample loss during the unpacking and repacking processes. Upon completion of HRMAS NMR analyses for samples 2 and 4 on the second day, they were also formalin-fixed for histopathology. According to this design, samples 2 and 3 represent frozen and fresh tissue, respectively, and in sample 4 the freeze-thawing effects were evaluated in the same sample. Lastly, sample 1 mimicked a routine clinical pathology procedure, and was used as a reference for evaluating tissue

---

[1] Department of Pathology, Massachusetts General Hospital, Harvard Medical School, Boston, Massachusetts.

[2] Department of Radiology, Massachusetts General Hospital, Harvard Medical School, Boston, Massachusetts.

[3] Francis Bitter Magnet Laboratory, Massachusetts Institute of Technology, Cambridge, Massachusetts.

Grant sponsor: PHS/NIH; Grant numbers: CA77727; CA80901; RR00995.

Chin-Lee Wu and Jennifer L. Taylor contributed equally to this work.

*Correspondence to: Leo L. Cheng, Pathology Research, CNY-7, 149 13th St., Charlestown, MA 02129. E-mail: cheng@nmr.mgh.harvard.edu

Received 20 March 2003; revised 31 July 2003; accepted 7 August 2003.

DOI 10.1002/mrm.10645

histopathological conditions influenced by freeze-thawing and spinning processes.

HRMAS Proton NMR

The NMR experiments were carried out on a Bruker (Billerica, MA) AVANCE spectrometer operating at 600 MHz (14.1T). A 4-mm zirconia rotor was used with Kel-F plastic inserts, which created a spherical sample space of ~10 μl located at the center of the detection coil. A small (~0.1 mg) silicone rubber sample was permanently fixed inside one of the Kel-F spacers, positioned within the detection coil but not in contact with the sample, to function as an external standard for both frequency reference (0.06 ppm from TMS) and quantification. Approximately 1.0 μl of D_2O was added into the rotor with the tissue sample for ^{2}H field locking. Within 3 min after tissue packing, the rotor containing the tissue sample and D_2O was introduced into the probe, precooled to 3°C, and spectroscopically measured. All NMR measurements were carried out at 3°C to ensure better tissue preservation. The rotor spinning rate was regulated by a MAS controller (Bruker) and verified by measuring inter-SSB distances from the spectra, with an accuracy of ±1.0 Hz. A TR of 5 s, and 32 transients were used to acquire each spectrum.

Spectra were collected with spinning rates of 600 and 700 Hz, and with or without a rotor synchronized DANTE sequence of 1000 DANTE pulses of 1.5 μs (8.4° flip angle) (5). A rotor-synchronized CPMG filter (10 ms) was included in the pulse sequence after the execution of the DANTE frequency-selective pulses to reduce broad resonances associated with probe background, rotor, and/or macromolecules. Spectra measured at 600 Hz spinning without DANTE were used to quantify the total NMR signal intensity, including tissue water, its sidebands, and all of the metabolites $[M_0]$.

The spectroscopic data were processed with Nuts software (Acorn NMR Inc., Livermore, CA) according to the following procedure: All free induction decays (FIDs) were subjected to 1 Hz apodization before Fourier transformation, baseline correction, and phase adjustment. The resonance intensities reported here represent integrals of curve-fittings with Lorentzian-Gaussian lineshapes. Resonance intensities, which depended on the particular spectral regions, were analyzed from one of the two spectra where there was no effect of water spinning sidebands (SSBs) and DANTE suppression, as previously described (5). About 50 of the most intensive resonance peaks in the spectral region between 0.5–4.5 ppm were thus quantified. The sum of these resonances was used to estimate the total metabolite intensity $[M_{\mathrm{met}}]$. The absolute concentration for metabolite a, $[M_a]$, was estimated according to the metabolite intensity measured in DANTE spectra $[M_{a\mathrm{DANTE}}]$, the total NMR signal intensity $[M_0]$ from the single pulse measurement, and the intensities of rubber standard measured under both conditions, $[\mathrm{STD}_0]$ and $[\mathrm{STD}_{\mathrm{DANTE}}]$, respectively, by using: $[M_a] = ([M_{a\mathrm{DANTE}}]/[\mathrm{STD}_{\mathrm{DANTE}}])*([\mathrm{STD}_0]/[M_0])$. The relative metabolite intensity $[M_{a\_\mathrm{rel}}]$ was calculated by: $[M_{a\_\mathrm{rel}}] = [M_{a\mathrm{DANTE}}]/[M_{\mathrm{met}}]$.

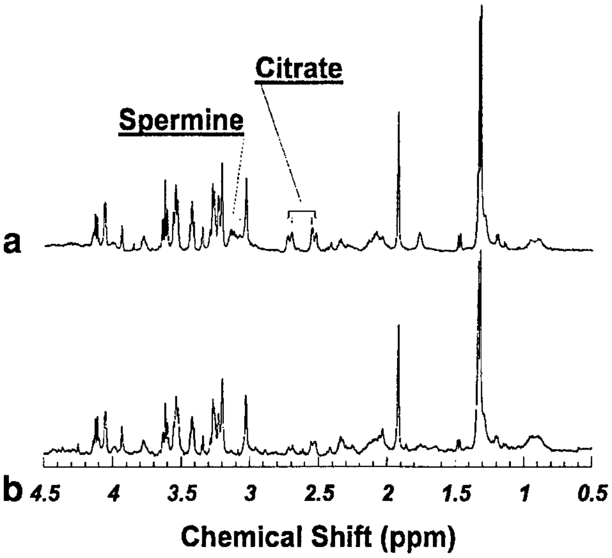

FIG. 1. Human prostate tissue HRMAS proton spectra measured (**a**) fresh, and (**b**) thawed after being frozen overnight. Both spectra are from the same sample.

Histopathology

In this study we focused on the effects of the tissue freeze-thawing process and HRMAS on the quality of histopathological images. Fixed tissue samples were cut into 7-μm sections and stained with hematoxylin and eosin. A set of three individual cuts, 100 μm apart, was obtained from each sample. Histopathological images of four sample sets from each specimen were compared by a genitourinary pathologist in random order and blinded fashion to determine the quality of the images on a scale of 1 to 5, with 5 being the best. The pathologist graded the histological quality by examining nuclear and cytologic features. Scale 5 is equivalent to the quality of routine, fresh clinical pathology samples that are fixed in formalin. Scale 3 is equivalent to the quality of a routine frozen-section slide of snap-frozen tissue. Scale 4 indicates a quality between scales 3 and 5. Scale 2 represents quality that is inferior to scale 3 but is sufficient for recognizing cell types and architecture. Scale 1 indicates histology that is insufficient for cell and tissue recognition.

RESULTS

Figure 1 shows the composite spectra (5) generated from DANTE spectra obtained with HRMAS rates of 600 and 700 Hz for one tissue sample (sample 4) that was both fresh and freeze-thawed, as described previously. Figure 1a displays the composite spectrum of fresh tissue, and Fig. 1b shows the same tissue thawed after being frozen overnight. The resolution values of the spectra are similar; however, close evaluation reveals that there may be some reduction in resonance intensity for certain metabolites (such as spermine and citrate) and the broad peak at 1.68–1.78 ppm after the freeze-thaw process. In addition, there appear to be alterations in the resonance profiles at the spectral region of 2.01–2.37 ppm as a result of the freeze-thaw process.

We compared the spectral resolution in terms of changes in linewidths for different metabolites before and after the

Table 1
Linear Correlations Between Absolute Metabolite Concentrations Measured Before and After Sample Freeze ($N = 12$)

Metabolite Resonance (ppm)	*P* value[a]	R^2	Slope[b]		Intercept[b]	
			Mean	SE	Mean	SE
Lac(4.10–4.14)	0.0045	0.57	**1.10**	**0.30**	**−0.96**	**4.12**
mI(4.06)	0.024	0.41	0.58	0.22	6.21	2.72
3.60–3.63[c]	0.0008	0.69	0.69	0.14	5.45	3.59
3.34	0.0075	0.57	0.74	0.22	1.67	1.65
3.26–3.27	0.016	0.49	0.55	0.19	**0.14**	**2.88**
Pch(3.22)	0.0019	0.68	**0.81**	**0.19**	**2.49**	**2.78**
Chol(3.20)	0.10	0.24	0.41	0.23	11.6	4.40
Spm(3.05–3.14)	<0.0001	0.86	0.55	0.07	**−1.07**	**4.64**
Cr(3.03)	0.0021	0.63	0.59	0.14	4.17	2.17
Cit(2.52–2.71)	<0.0001	0.86	0.67	0.09	**1.47**	**3.03**
2.31–2.37	0.037	0.40	**0.85**	**0.35**	**3.41**	**3.55**
2.01–2.14	0.0075	0.57	0.74	0.22	9.21	9.17
Acet(1.92)	<0.0001	0.97	**0.98**	**0.05**	**−0.28**	**0.65**
1.68–1.78	0.0001	0.82	0.57	0.09	2.34	2.47
Ala(1.47–1.49)	0.0004	0.73	**0.85**	**0.16**	**1.13**	**1.22**
Lac(1.32–1.34)	0.0004	0.73	**1.04**	**0.20**	**−3.74**	**16.67**
1.19–1.20	0.0003	0.75	**1.03**	**0.19**	**−0.17**	**0.59**
1.04–1.05	<0.0001	0.90	0.82	0.09	**0.23**	**0.28**
Lipid(0.90)	0.0022	0.63	1.38	0.34	**−2.63**	**5.00**

[a] Linear analyses conducted by plotting intensity after freezing (vertical) against that of fresh (horizontal), a slope of <1.0 indicated a reduction in intensity after sample freeze.

[b] Bold faced data in the table indicate either slopes are statistically indifferent (considering the range of Mean based on ± SE) from 1, or the intercepts are indifferent from 0.

[c] Resonance peaks not yet positively identified with metabolites.

freeze-thawing process. We found that except for two metabolites—citrate (19% reduction in linewidth after freeze-thawing, $N = 92$, one-way ANOVA, $P < 0.04$) and acetate (36% reduction, $N = 32$, one-way ANOVA, $P < 0.05$)—there was no indication that freeze-thawing improved spectral resolution, i.e., there was no statistically significant line-narrowing effect associated with tissue freezing (as determined by ANOVA) that would support the concerns raised by previous studies (1).

The changes observed in metabolite intensities in the same tissue samples before and after freezing (sample 4 type) are summarized in Tables 1 and 2. Table 1 shows the results of linear regression analyses on the estimated absolute metabolite concentrations (6). These linear analyses were conducted by plotting intensity after freezing (vertical) against that of fresh (horizontal). Therefore, a slope of <1.0 indicates a reduction in intensity after the sample was frozen. The boldface data in the table indicate slopes that are not statistically different (considering the range of mean based on ±SE) from one, or intercepts that are not different from zero. The data in the table appear to indicate that freezing resulted in reductions (20–45%) in absolute metabolite concentrations $[M_a]$ for more than half of the analyzed metabolites, while only one resonance peak (lipid at 0.9 ppm) showed a slight increase in concentration (with a slope of 1.38 ± 0.34). Similar (but slightly better) correlation results obtained from analyses of the relative metabolite intensities $[M_{a\_rel}]$ before and after the freeze-thawing process were observed, as shown in Table 2.

The current histopathological evaluations of tissues (fresh from surgery, and analyzed by HRMAS NMR without freezing and after freeze-thaw treatment) were aimed at identifying the effects of these processes on histopathological integrity, as illustrated by an image-quality index on a scale of 1 to 5. The results indicate that fresh tissues that were spun at 600 Hz (<25 min) and then at 700 Hz (<5 min) produced high-quality images that were indistinguishable from those of the original tissue (indices: 4.75 ± 0.16 vs. 4.58 ± 0.19) (Fig. 2). However, freezing the tissue compromises the quality of the resulting images (3.75 ± 0.26), which agrees with the accepted wisdom in clinical pathology.

DISCUSSION AND CONCLUSIONS

Sample-freezing processes can potentially alter the physical state of tissue cellular metabolites, as well as the environment of tissue water. For instance, the freezing process may interrupt the linkages of metabolites and water with cell membranes and/or macromolecules, such as proteins. A change in the physical state of a metabolite and/or tissue water viscosity may lead to a change in NMR-related physical parameters, such as relaxation times and diffusion coefficients. Ultimately, the observed spectral profiles may be different. Therefore, the freeze-thawing effects previously observed in the rodent renal cortex were neither a surprise nor an issue unique to HRMAS NMR analysis (1). This may indicate that such effects, if they exist, may not be observable at low spectral resolution with conventional NMR without the assistance of HRMAS.

An evaluation of possible freeze-thawing effects on intact-tissue HRMAS spectra may include the following two aspects: spectral resolution and resonance intensities. Our results from human prostate tissue (see Fig. 1) suggest that for most analyzed metabolites there are no obvious in-

Table 2
Linear Correlations Between Relative Metabolite Intensities Measured Before and After Sample Freeze (N = 12)

Metabolite Resonance (ppm)	P value[a]	R^2	Slope[b]		Intercept[b]	
			Mean	SE	Mean	SE
Lac(4.10–4.14)	0.0041	0.62	0.76	0.20	1.55	0.89
mI(4.06)	0.0003	0.75	1.28	0.23	**−0.16**	**0.94**
3.60–3.63[c]	0.0047	0.57	0.76	0.21	2.09	1.70
3.34	0.0046	0.61	**0.88**	**0.24**	**0.45**	**0.57**
3.26–3.27	0.028	0.40	0.60	0.23	1.82	0.92
Pch(3.22)	0.0008	0.73	**0.84**	**0.17**	**0.98**	**0.78**
Chol(3.20)	0.0020	0.63	**0.87**	**0.21**	1.97	1.38
Spm(3.05–3.14)	<0.0001	0.89	0.70	0.08	**−0.15**	**1.13**
Cr(3.03)	<0.0001	0.80	0.86	0.13	0.67	0.57
Cit(2.52–2.71)	0.0002	0.76	**0.88**	**0.16**	**−0.12**	**1.31**
2.31–2.37	0.078	0.31	**0.83**	**0.42**	1.72	1.45
2.01–2.14	0.0002	0.80	1.30	0.21	**−2.22**	**2.89**
Acet(1.92)	<0.0001	0.95	1.31	0.10	**−0.28**	**0.32**
1.68–1.78	0.0029	0.64	0.57	0.14	1.41	0.82
Ala(1.47–1.49)	0.0004	0.74	0.81	0.15	0.58	0.35
Lac(1.32–1.34)	0.0023	0.62	**0.80**	**0.20**	6.56	5.46
1.19–1.20	0.0009	0.69	**0.93**	**0.20**	**0.07**	**0.24**
1.04–1.05	0.0002	0.77	0.72	0.13	0.14	0.12
Lipid(0.90)	0.0008	0.69	1.30	0.27	**−0.33**	**1.55**

[a] Linear analyses conducted by plotting intensity after freezing (vertical) against that of fresh (horizontal), a slope of <1.0 indicated a reduction in intensity after sample freeze.

[b] Bold faced data in the table indicate either slopes are statistically indifferent (considering the range of Mean based on ± SE) from 1, or the intercepts are indifferent from 0.

[c] Resonance peaks not yet positively identified with metabolites.

creases in spectral resolution associated with tissue freezing, i.e. the resonance linewidths for these metabolites do not become narrower after the tissue is freeze-thawed compared to those measured in fresh tissue. However, such reductions were indeed observed with citrate and acetate, which indicates that these metabolites may have increased mobility after the freeze-thawing process. This observation is very important because citrate is a well-recognized prostate metabolite marker (7–11). Further studies of citrate (for example, including measurements of associated relaxation times) are warranted. If this finding is confirmed, it may increase our understanding of citrate, and its function and associations within prostate cells (12,13).

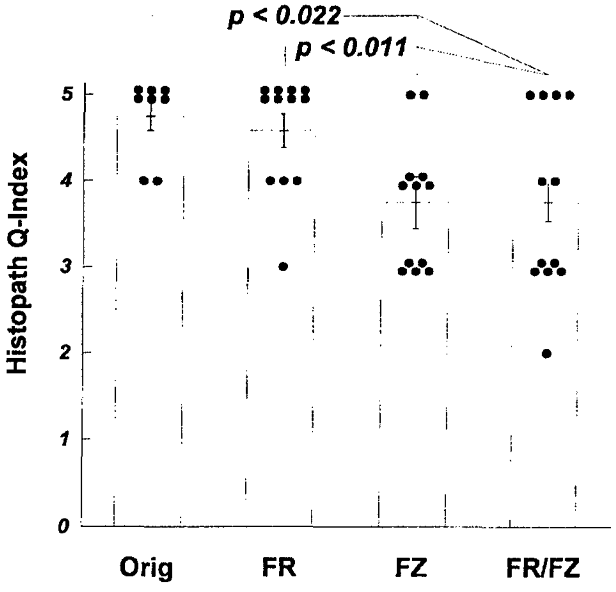

FIG. 2. Histopathological evaluations of tissues fresh from surgery (Orig) and analyzed by HRMAS NMR without freezing (FR) and after freeze-thaw treatment (FZ + FR/FZ). The histopathological images were graded on a scale of 1 to 5, with 5 indicating best quality.

The calculation of resonance intensity is a more complicated process than the measurement of resonance linewidth. We explored two different types of calculations: absolute concentration and relative intensity. Clearly, the calculation of the absolute metabolite concentration depends on the assumption of an important factor that is believed to be "absolute," measurable, and constant. Normally, the sample weight is used as such a factor. For this study, we considered using sample weight; however, in our particular situation, measurements of sample weight were found to be less practical because of the small size of the tested tissue (~10 mg) and the associated measurement error. It was not difficult to estimate the measurement error in the sample weight, since the sample was packed into the sample rotor, which weighed about 10^3 times more than the sample. In addition, we could not let tissue samples be exposed to air for an extended amount of time (minutes) for multiple measurements because that would certainly have resulted in a loss of tissue water. We therefore chose to use the total spectral intensity, including water and its SSB [M_0] measured at 600 Hz spinning rate, and without the DANTE pulse sequence, to calculate the metabolite concentrations (Table 1).

The measurements of slopes and intercepts presented in Table 1 indicate that the degradation of tissue caused by the freeze-thaw process may modify the environment of metabolites to various degrees, and cause the NMR parameters associated with these metabolites to change. However, the data in this table suggest that there is a general reduction for almost all of the analyzed metabolites after tissue freeze-thawing, with the mean for the mean values of the slopes being 0.79 ± 0.05. These calculated values may be skewed because of the change in the water environment of the tissue, i.e., the $[M_0]$ values were increased, perhaps due to the reduction of water viscosity after freeze-thawing. This speculation was supported to a certain degree by our data regarding the relative metabolite intensity $[M_{a\_rel}]$ in Table 2, where $[M_0]$ values were not entered into the calculations. The slopes in Table 2 are closer to 1.0 than those in Table 1. In fact, the mean for the mean values of the slopes is now 0.89 ± 0.05. Overall, the results presented in both tables indicate that even if there were metabolite changes associated the freeze-thaw process, these changes (increase or decrease) were <50% of the values measured with fresh tissues for all of the analyzed metabolites. Although these changes may present a significant issue for researchers seeking absolute metabolic quantifications, they are certainly much smaller than the worrisome reported increases of as much as 300% (1).

Finally, our histopathology data indicate that there is a measurable difference between fresh and freeze-thawed prostate tissue in terms of the quality of the histopathological images. These data confirm our previous observation that mechanical spinning of human prostate tissue in a 4-mm rotor at a rate of ≤700 Hz for ~30 min does not produce tissue damage that compromises the integrity of the tissue histopathology (5).

In conclusion, we have shown that the freeze-thaw process in tissue does not appear to change the overall spectral resolutions measured by resonance linewidths. However, there were a few exceptions (such as citrate and acetate), which warrant further investigation. We have also shown that while there are differences in metabolite intensities between fresh and freeze-thawed samples, these differences are more pronounced with absolute concentrations than with relative intensities. The possible freeze-thawing effect on the measured concentration of an individual metabolite of clinical interest should be evaluated and accounted for in practice to further the utility of ex vivo HRMAS in clinical applications.

ACKNOWLEDGMENT

The authors thank Dr. Eva Ratai for her careful reading of the manuscript.

REFERENCES

1. Middleton DA, Bradley DP, Connor SC, Mullins PG, Reid DG. The effect of sample freezing on proton magic-angle spinning NMR spectra of biological tissue. Magn Reson Med 1998;40:166–169.
2. Garrod S, Humpfer E, Spraul M, Connor SC, Polley S, Connelly J, Lindon JC, Nicholson JK, Holmes E. High-resolution magic angle spinning 1H NMR spectroscopic studies on intact rat renal cortex and medulla. Magn Reson Med 1999;41:1108–1118.
3. Waters NJ, Garrod S, Farrant RD, Haselden JN, Connor SC, Connelly J, Lindon JC, Holmes E, Nicholson JK. High-resolution magic angle spinning (1)H NMR spectroscopy of intact liver and kidney: optimization of sample preparation procedures and biochemical stability of tissue during spectral acquisition. Anal Biochem 2000;282:16–23.
4. Sitter B, Sonnewald U, Spraul M, Fjosne HE, Gribbestad IS. High-resolution magic angle spinning MRS of breast cancer tissue. NMR Biomed 2002;15:327–337.
5. Taylor JL, Bielecki A, Wu CL, Gonzalez RG, Cheng LL. Ex vivo HRMAS MRS analysis of intact tissue at slow sample spinning rates. In: Proceedings of the 10th Annual Meeting of ISMRM, Honolulu, 2002. p 135.
6. Cheng LL, Ma MJ, Becerra L, Ptak T, Tracey I, Lackner A, Gonzalez RG. Quantitative neuropathology by high resolution magic angle spinning proton magnetic resonance spectroscopy. Proc Natl Acad Sci USA 1997;94:6408–6413.
7. Lynch MJ, Nicholson JK. Proton MRS of human prostatic fluid: correlations between citrate, spermine, and myo-inositol levels and changes with disease. Prostate 1997;30:248–255.
8. Zaider M, Zelefsky MJ, Lee EK, Zakian KL, Amols HI, Dyke J, Cohen G, Hu Y, Endi AK, Chui C, Koutcher JA. Treatment planning for prostate implants using magnetic-resonance spectroscopy imaging. Int J Radiat Oncol Biol Phys 2000;47:1085–1096.
9. Mueller-Lisse UG, Vigneron DB, Hricak H, Swanson MG, Carroll PR, Bessette A, Scheidler J, Srivastava A, Males RG, Cha I, Kurhanewicz J. Localized prostate cancer: effect of hormone deprivation therapy measured by using combined three-dimensional 1H MR spectroscopy and MR imaging: clinicopathologic case-controlled study. Radiology 2001;221:380–390.
10. Swanson MG, Vigneron DB, Tran TK, Sailasuta N, Hurd RE, Kurhanewicz J. Single-voxel oversampled j-resolved spectroscopy of in vivo human prostate tissue. Magn Reson Med 2001;45:973–980.
11. Kurhanewicz J, Swanson MG, Nelson SJ, Vigneron DB. Combined magnetic resonance imaging and spectroscopic imaging approach to molecular imaging of prostate cancer. J Magn Reson Imaging 2002;16:451–463.
12. Costello LC, Franklin RB. Testosterone and prolactin regulation of metabolic genes and citrate metabolism of prostate epithelial cells. Horm Metab Res 2002;34:417–424.
13. Costello LC, Franklin RB, Narayan P. Citrate in the diagnosis of prostate cancer. Prostate 1999;38:237–245.

Magnetic Resonance in Medicine 50:627–632 (2003)

High-Resolution Magic Angle Spinning Proton NMR Analysis of Human Prostate Tissue With Slow Spinning Rates

Jennifer L. Taylor,[1] Chin-Lee Wu,[1] David Cory,[2] R. Gilberto Gonzalez,[3]
Anthony Bielecki,[4] and Leo L. Cheng[1,3*]

The development of high-resolution magic angle spinning (HR-MAS) NMR spectroscopy for intact tissue analysis and the correlations between the measured tissue metabolites and disease pathologies have inspired investigations of slow-spinning methodologies to maximize the protection of tissue pathology structures from HR-MAS centrifuging damage. Spinning sidebands produced by slow-rate spinning must be suppressed to prevent their complicating the spectral region of metabolites. Twenty-two human prostatectomy samples were analyzed on a 14.1T spectrometer, with HR-MAS spinning rates of 600 Hz, 700 Hz, and 3.0 kHz, a repetition time of 5 sec, and employing various rotor-synchronized suppression methods, including DANTE, WATERGATE, TOSS, and PASS pulse sequences. Among them, DANTE, as the simplest scheme, has shown the most potential in suppression of tissue water signals and spinning sidebands, as well as in quantifying metabolic concentrations. Magn Reson Med 50: 627–632, 2003. © 2003 Wiley-Liss, Inc.

Key words: HR-MAS; proton MRS; human prostate; slow spinning

The use of ex vivo high-resolution magic angle spinning (HR-MAS) in proton NMR studies of intact tissue results in highly resolved spectra comparable to those observed with solutions of tissue chemical extractions (1–8). However, unlike destructive chemical extractions, the HR-MAS method largely preserves histopathological structures intact, granting the opportunity for samples to be histopathologically examined after NMR measurement, which is extremely important, particularly for studies of human neoplastic diseases because of the well-known heterogeneous characteristics within individual tumors.

The HR-MAS method achieves high spectral resolution from biological tissues by eliminating spectral broadening largely caused by magnetic susceptibility. In the frequency domain of an NMR spectrum, spinning splits the broad resonance into a center peak at the isotropic resonance frequency and a number of spinning sidebands (SSBs) separated by the spinning rate. If the spinning frequency is greater than the frequency region of cellular metabolites, the SSB will be pushed outside of the region of interest, so that the region consists of only individual isotropic resonance peaks. In studies of biological cells and/or tissues, water, arising from either the media or the tissue itself, is the most intense resonance and the component contributing to the largest observed SSB. To eliminate the complication of water SSB on spectra of cellular metabolites, spinning rates that are equal to or above 5 ppm (3.0 kHz at 14.1T) have commonly been employed.

It has also been noted experimentally that spectral broadening primarily induced by bulk magnetic susceptibility can be substantially reduced with a sample-spinning rate of a few hundred Hz. In other words, if the complex issue of water SSB could be resolved, HR-MAS proton NMR spectra for most intact tissue could be measured at a spinning rate at least an order of magnitude lower than is commonly used. A reduction in sample spinning rates by 5–10-fold represents a 25–100-fold decrease in spinning-induced centrifugal stress. Since centrifugal stress may damage the organizational structure of connective tissue, although perhaps not disrupt cells, reducing spinning centrifugal stress can better preserve tissue pathological structures, which will translate into a more accurate evaluation of their pathologies (9).

We studied slow HR-MAS with various SSB suppression methodologies on human prostate tissues. We evaluated and compared rotor-synchronized DANTE (delays alternating with nutations for tailored excitation) (10,11), rotor-synchronized WATERGATE (water suppression by gradient-tailored excitation) (12), 1D-TOSS (total sideband suppression) (13), and 2D-PASS (phase-adjusted spinning sidebands) (14) sequences with presaturation for water suppression. Among these techniques, we found the rotor-synchronized DANTE sequence to be the most robust technique in terms of the reproducibility of SSB suppression and simplicity in concept and execution. Results of DANTE measurements at spinning rates of 600 and 700 Hz are reported here.

MATERIALS AND METHODS

Tissue Protocol

Samples from 22 prostatectomy cases were used in the study. Among them, for the first 13 cases two samples from each case were analyzed separately at low speeds (600, then 700 Hz) or at high speed (3.0 kHz), and the histopathological integrity of each sample was compared with the integrity observed from the adjacent tissue that was not subjected to spinning. For the remaining nine

---

[1] Department of Pathology, Massachusetts General Hospital, Harvard Medical School, Boston, Massachusetts.

[2] Department of Nuclear Engineering, Massachusetts Institute of Technology, Cambridge, Massachusetts.

[3] Department of Radiology, Massachusetts General Hospital, Harvard Medical School, Boston, Massachusetts.

[4] Francis Bitter Magnet Laboratory, Massachusetts Institute of Technology, Cambridge, Massachusetts.

Grant sponsor: PHS/NIH; Grant numbers: CA77727; CA80901; RR00995.

*Correspondence to: Leo L. Cheng, Pathology Research, CNY-7, 149 13th Street, Charlestown, MA 02129. E-mail: cheng@nmr.mgh.harvard.edu.

Received 28 October 2002; revised 2 May 2003; accepted 2 May 2003.
DOI 10.1002/mrm.10562

cases, one sample from each case was measured both at low (600, then 700 Hz) and then at high (3.0 kHz) spinning rates in order to evaluate the observed metabolite intensities from the same tissue under different rates of spinning.

HR-MAS Proton NMR

The NMR experiments were carried out on a Bruker (Billerica, MA) AVANCE spectrometer operating at 600 MHz (14.1T). A 4 mm zirconia rotor was used with Kel-F plastic inserts which created a spherical sample space of ~10 μl located at the center of the detection coil. A small (~10^{-1} mg) silicone rubber sample was permanently affixed inside one of the Kel-F spacers, positioned within the detection coil but not in contact with the sample, to function as an external standard for both frequency reference (0.06 ppm from TMS) and quantification. Tissue samples, ~8–10 mg, were used directly from freezers without further preparation. Sample packing was performed on a metal surface covered with gauze and resting on dry ice. Approximately 1.0 μl of D_2O was added into the rotor for ^2H field locking. Within less than 3 min after the completion of tissue packing, the rotor containing the tissue sample and D_2O was introduced into the probe precooled to 3°C. After waiting an additional ~3 min for temperature equilibration, the NMR spectra were measured. All NMR measurements were carried out at 3°C for better tissue preservation. At this temperature, spectral line-width of tissue water and the D_2O lock solvent indicated that the sample was not in a frozen state. While the freezing point of D_2O is nominally 3.8°C, its freezing point is evidently depressed by dispersal in tissue fluids. The rotor-spinning rate was regulated by a MAS controller (Bruker), and verified by measurements of inter-SSB distances from spectra with an accuracy of ±1.0 Hz. Each spectrum was acquired with 32 transients and a repetition time of 5 sec.

The DANTE pulse sequence achieves resonance selectivity based on the timing of RF pulses. We used rotor-synchronized DANTE, i.e., the interpulse spacings were set equal to the rotor cycle time. This has the effect of suppressing signal components spaced at intervals of the rotor frequency and centered on the spectrometer frequency. In our experiments, we set the spectrometer frequency on the water resonance. The water peak and all of its SSBs are therefore suppressed, but so, too, are any other resonances that occur close to those frequencies. A rotor-synchronized CPMG filter (10 ms) was included in the pulse sequence after the execution of the DANTE pulses to reduce broad resonances associated with probe background, rotor, and/or macromolecules. One thousand DANTE pulses of 1.5 μs (8.4° flip angle) were used. Figure 1 shows the diagram of the pulse sequence, including both CPMG and DANTE components.

Spectroscopic data were processed by using the Nuts software (Acorn NMR, Livermore, CA) according to the following procedures. All free induction decays were subjected to 1 Hz apodization before Fourier transformation, baseline correction, and phase adjustment. Resonance intensities reported here represent integrals of curve-fittings with Lorentzian-Gaussian line-shapes.

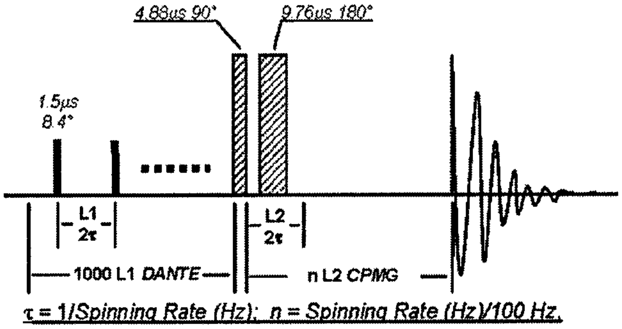

FIG. 1. A diagram of the rotor-synchronized CPMG-DANTE pulse sequence used in the study.

Histopathology

In this study, evaluation of tissue histopathology was focused on the comparison of varying HR-MAS-induced spinning centrifugal stresses on the resulting histopathology integrity. To achieve this aim with the first 13 cases, as previously described, both high rate and low rate HR-MAS experiments were conducted on separate but adjacent tissue samples. Specifically, specimens of ~30 mg from each case were cut with a surgical blade into three approximately equal portions. While one sample was used directly for histopathology evaluation, the other two were used to measure HR-MAS spectra at different spinning rates at 3°C. One sample was spun at 600 Hz for about 45 min, then at 700 Hz for about 15 min, while the other was spun at 3.0 kHz for 1 hr. These two spun samples, as well as the nonspinning sample, were processed according to routine histopathological procedures, cut into 7-μm sections on a cryotome, and stained with hematoxylin and eosin. A set of three individual cuts spaced 100 μm apart was obtained from each sample. These three sets of histopathological images from each case were compared by the pathologist in a random order to determine the effect of HR-MAS rates on the pathology structures. The pathologist was blinded from the history of samples and asked simply to identify the worst tissue quality among the three sets for each case in terms of tissue histopathological integrity by visual examination.

RESULTS

Spinning Effects on Tissue Histopathological Appearance

Figure 2 shows an example of the effects of HR-MAS stress on tissue morphology. All three images were obtained with the same clinical case, from adjacent tissue, and under the same magnification. Figure 2a shows a histopathological image of human prostate tissue that was obtained directly from frozen sample without being subjected to a spinning test. The image shows normal glandular structures with well-defined epithelial cells. Figure 2b shows the adjacent tissue of the same specimen after an HR-MAS experiment of slow spinning rates (600, 700 Hz). The image exhibits morphological structures similar to that of the original sample (Fig. 2a). Figure 2c shows another adjacent sample of the same specimen after its HR-MAS analysis at a higher spinning frequency of 3.0 kHz.

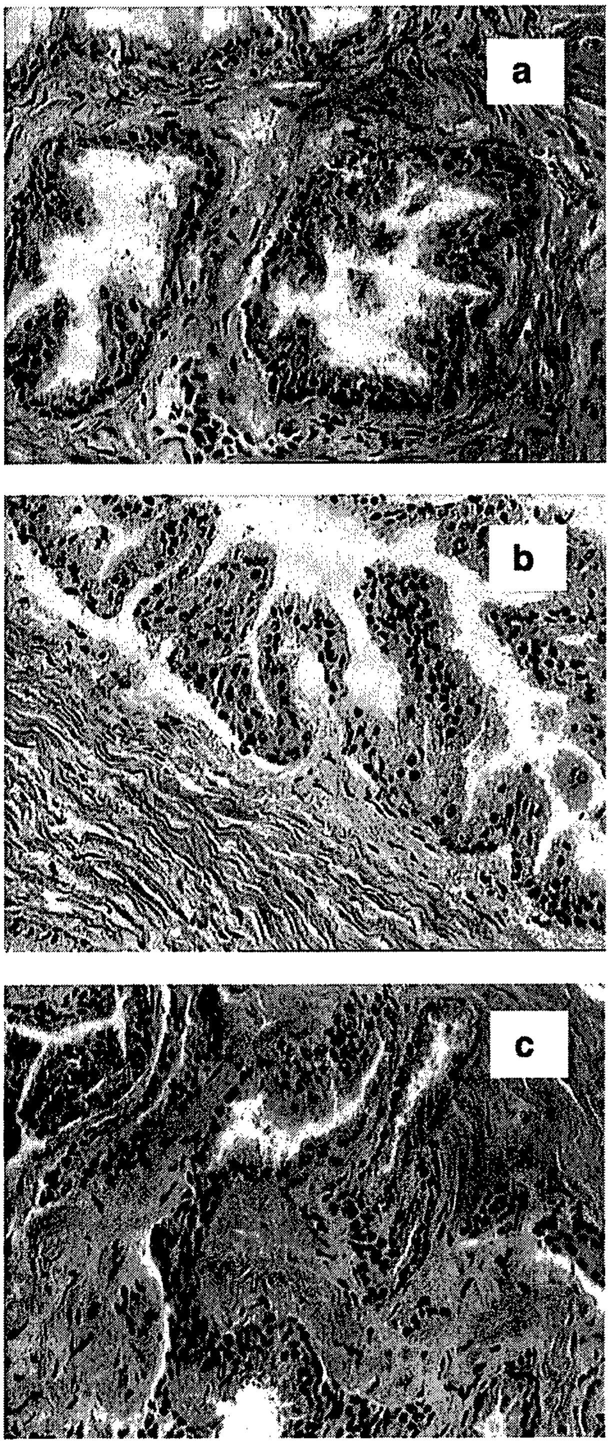

FIG. 2. The effects of HR-MAS stress on tissue morphology. **a:** A human prostate tissue sample taken directly from a tissue bank without HR-MAS testing. The tissue showed highly organized ductal cellular structures with well-defined epithelial layers. **b:** Another sample from the same patient but after an HR-MAS experiment, which involved spinning at 600 Hz for 45 min and then 700 Hz for 15 min. The tissue still exhibits a normal ductal structure that cannot be differentiated from the original sample (a). **c:** A sample, again from the same clinical case, after MAS analysis at higher spinning frequency, 3.0 kHz, for 1 hr. The tissue ductal structures are visibly distorted compared with the natural specimens. (Images presented at the same magnification.)

The distortion of ductal epithelial structures is visible when compared with ducts in Fig. 2a,b. Similar spinning effects on prostate tissue and the compromised histopathological integrity with 3.0 kHz spinning frequency were observed consistently with all 13 cases. Specifically, the pathologist always identified the tissue set after 3.0 kHz spinning to be the worst in pathological integrity for all cases. However, it should also be pointed out that such a compromise in histopathological structures did not hinder the pathologist's ability to differentiate, for instance, cancer from normal cells at cellular levels. Only the macrostructures, such as estimation of the amount of normal epithelial ducts, are affected by the fast spinning.

DANTE Spectra

At slow spinning rates, such as 600 Hz, HR-MAS single-pulse proton spectra of tissues are dominated by a large water peak and its SSB, typically with large amplitudes over a range of several ppm, as shown in Fig. 3a. The water centerband can be suppressed reasonably well with presaturation (with 5-sec CW during recycle delay time and a power level of 60 dB reduction from that of excitation pulses). Presaturation also reduces the SSB intensities, but these reductions were not sufficient to create clean spectra for metabolite quantification (see Fig. 3b). With DANTE pulses, as shown in Fig. 4a,b, although residual water SSB are still observable, they are reasonably small compared with those shown in Fig. 3. In either the 600 or 700 Hz spectrum, DANTE suppression leaves invalid regions that cannot be used for metabolite measurement. These two spin rates were selected to meet the following criteria: 1) the difference between the spin rates (100 Hz) is much greater than the water and metabolite linewidths (<10 Hz), and also greater than the width of the spectral regions attenuated by the DANTE pulse sequence (42 Hz); 2) arbitrary multiples of the two spin rates approach no closer than the difference between spin rates, except at their least

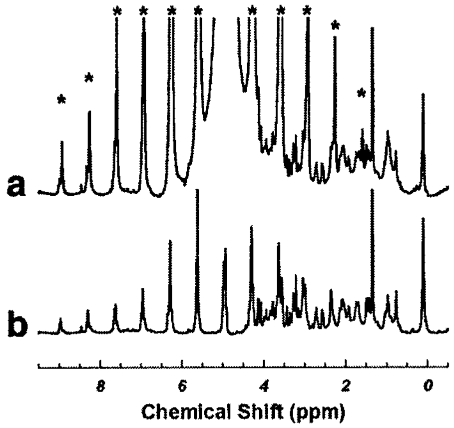

FIG. 3. **a:** An HR-MAS single-pulse proton spectrum of prostate tissue dominated by a large water peak and its SSB at 600 Hz. **b:** Suppression of water centerband with presaturation. Presaturation also reduces the SSB intensities, but these reductions were not sufficient to create clean spectra for metabolite quantification. Asterisk denotes spinning sidebands in this figure and in those that follow.

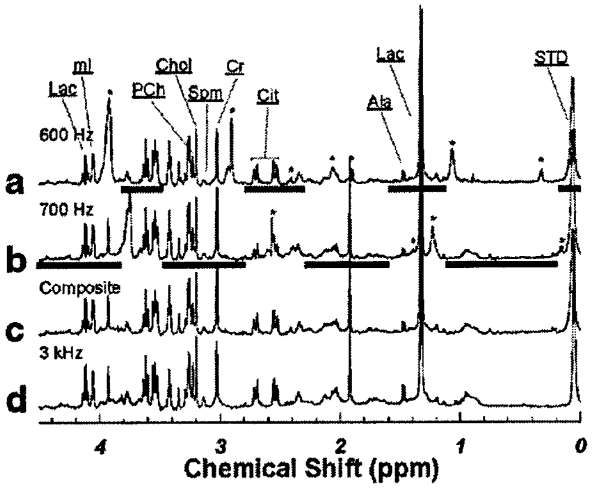

FIG. 4. Human prostate rotor-synchronized DANTE spectra at spinning rates of (**a**) 600 Hz, and (**b**) 700 Hz. **c:** A spectrum composed from (**a**) and (**b**) to be visually compared with (**d**) a spectrum obtained at spinning rate of 3.0 kHz. Abbreviations: Lac, lactate; mI, myo-inositol; PCh, phosphorylcholine; Chol, choline; Spm, spermine; Cr, creatine; Cit, citrate; Ala, alanine; STD, rubber standard. Spectral regions of **a** and **b** used to generate **c** are labeled with horizontal bars beneath them. The following symbols are used to denote SSB: "*," tissue water; "+," STD; and "#," Lac at 1.33 ppm.

common multiple; 3) the least common multiple of the two spin rates (4.2 kHz, or 7 ppm) is greater than the width of the region of water and metabolite peaks (3.0 kHz, or 5 ppm); and 4) the two spinning rates are close enough that the intensities of a particular tissue metabolite measured from both spectra are identical. These criteria ensure that every point in the region-of-interest will be free of water SSB and DANTE holes in at least one of the two spectra. Thus, the two spectra together may be used to estimate intensities for each metabolite peak, except for a small region near the water centerband. However, this issue of the distortion of spectral regions near the water centerband is common with any scheme of water suppression.

Figure 4c shows a composite spectrum, which was assembled simply by cutting and pasting valid regions of the 600 and 700 Hz HR-MAS spectra. These valid regions were free of SSB from tissue water and the external standard, as indicated by the horizontal bars under Fig. 4a,b, respectively. Figure 4c shows a close similarity to the 3.0 kHz spectrum, shown in Fig. 4d. Here we wish to point out that, in our experience studying human prostate samples, we have not seen severe spectral complication due to SSB from metabolites (except lactate at 1.33 ppm; cf. Fig. 4a,b). This phenomenon further proves that the primary effect of HR-MAS in biological tissue analysis is to average magnetic susceptibility of mobile cellular metabolites, rather than to overcome solid effects of metabolite molecules as in the case of solid-state NMR. However, should visible SSBs from metabolites present, the currently identified spectral regions under the tested spinning rates may still contain metabolite SSB. Nevertheless, we consider that Fig. 4c serves only as a visual illustration of a complete, sideband-free spectrum. A quantitative evaluation of a particular metabolite can be carried out directly from at least one of the two original spectra at a 600 or 700 Hz spinning rate, where SSBs do not overlap with the resonance of interest. Therefore, although the cutting and pasting process plays a helpful role for visualization of the results, it is not a necessary or a recommended method for the quantification of tissue metabolites. It should always be possible, by selecting a certain spinning rate, to quantify a defined metabolic marker (or markers) with a single DANTE-CPMG spectrum.

Metabolite Intensities

The accuracy of cellular metabolite intensities measured at slow HR-MAS rates can be evaluated by comparing them with those measured at "traditional" or high HR-MAS spinning rates. Figure 5 plots the sum of metabolite intensities identified in Fig. 4 as a function of sample weights, measured at slow spinning rates (600, 700 Hz), as well as 3.0 kHz, under otherwise identical experimental conditions (DANTE presaturation time and T_2 filter time). Only samples with weight <11 mg are included in the figure because the sample space created by the spherical inserts is ~10 μl. For samples with weights much more than 10 mg, we observed that some of the tissue and/or fluids were squeezed out of the space into the well of the sealing screw in the upper insert. Figure 5 shows that the linear relationship under slow spinning condition passes much closer to the origin. Therefore, the correlation between sample weights and the total resonance intensity is better preserved under slow spinning conditions.

We next compared the intensities of individual metabolite resonances measured at slow spinning rates (600, 700 Hz) with those at 3.0 kHz for the same tissue samples from nine clinical cases. Linear regression results (slow rates: vertical, vs. 3.0 kHz rate: horizontal) of the comparisons for selected metabolite intensities normalized by the intensities of the external rubber standard (STD) measured at 600 Hz and 3.0 kHz are listed in Table 1. By adjusting

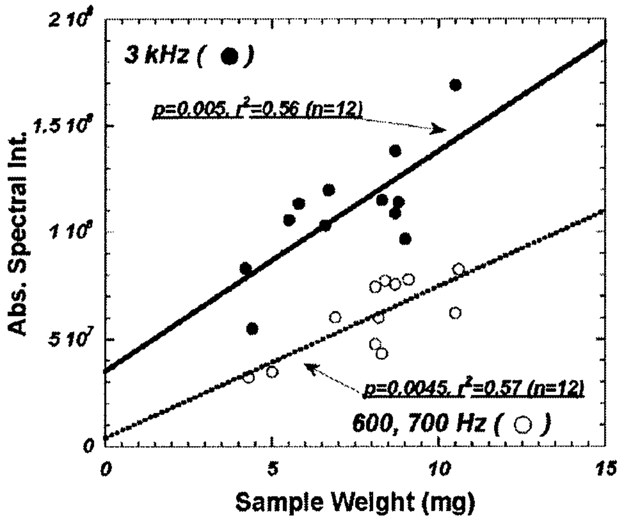

FIG. 5. Results of the total spectral intensities (i.e., the sum of metabolites labeled in Fig. 4) as a function of sample weights, measured at spinning rates of 600, 700 Hz, and 3.0 kHz.

Table 1
Comparison of Linear Regressions (Slow Rates: Vertical, vs. 3.0 kHz Rate: Horizontal) for Selected Metabolites Normalized by the Intensities of the External Rubber Standard (STD)

Met. reson. (ppm)	*P* value	R^2	Slope[a] Mean	Slope[a] SE	Intercept Mean	Intercept SE
Lac (4.10–4.14)	0.0013	0.97	1.27	0.25	−0.11	0.07
mI (4.06)	0.0002	0.88	**1.00**[b]	**0.14**	**0.00**	**0.02**
Pch (3.22)	0.0025	0.75	**1.24**	**0.27**	**−0.02**	**0.03**
Chol (3.20)	<0.0001	0.95	1.20	0.11	−0.05	0.03
Spm (3.10–3.14)	0.0055	0.69	0.48	0.12	**0.01**	**0.01**
Cr (3.03)	0.055	0.43	0.65	0.28	**0.04**	**0.04**
Cit (2.52–2.71)	<0.0001	0.86	0.67	0.09	0.06	0.03
Acet (1.92)	<0.0001	0.97	0.65	0.04	0.06	0.03
Ala (1.47–1.49)	0.0002	0.87	**0.95**	**0.14**	−0.02	0.01
Lac (1.32–1.34)	0.0004	0.86	0.77	0.12	**−0.05**	**0.15**

[a] Statistically significant linear correlations with slopes close to 1 are observed with some metabolites, while slopes deviating from unity are observed with the others, for which the 3.0 kHz spinning rate produces slightly higher intensities.

[b] Boldface data in the table indicate either slopes are statistically indifferent (considering the range of mean based on ±SE) from 1, or the intercepts are indifferent from 0.

the gain of the spectrometer receiver, the absolute STD intensities at both spinning rates are approximately the same ($2.6 \pm 0.3 \times 10^7$ for 600 Hz, and $2.8 \pm 0.4 \times 10^7$ for 3.0 kHz). Statistically significant linear correlations with slopes close to 1.0 are observed with some metabolites, while slopes deviating from unity are observed with the others in which 3.0 kHz spinning rate produces slightly higher intensities. Histopathological analysis on these nine samples indicated a similarity in their pathological compositions (14.0 ± 5.1% epithelium and 86.0 ± 5.1% stroma).

DISCUSSION AND CONCLUSIONS

There are several possible mechanisms by which HR-MAS may alter tissue morphologies. However, regardless of the mechanisms involved with a particular type of biological tissue, or in an individual sample, the faster the spinning rate, the larger the effect on the destruction of tissue morphology. Drastic morphological changes can also affect tissue MR-related physical parameters, such as T_1, T_2, and diffusion coefficients, etc., that in turn will require different instrumental parameters, or will affect signal intensities. Therefore, a reduction in HR-MAS rate can potentially result in better preservation of both tissue morphological structures and MR parameters. Although the DANTE experiment can be measured at any slow rate of spinning, the reduction of HR-MAS rate is limited by the linewidth of tissue static spectra, i.e., the spinning rates in Hz needs to be higher (larger) than the static resonance linewidth in order for the principle of HR-MAS to be effective. On the other hand, as in vivo methods continue to improve, it will become increasingly necessary to correlate ex vivo results with in vivo observations. It follows logically that: the slower the spinning rate of the ex vivo tests, the higher the accuracy for the in vivo comparison.

In general, there can be quantitation errors at low spinning rates, due to either slow molecular tumbling, diffusion in inhomogeneous fields, or residual (incompletely averaged) dipolar couplings and/or chemical shift anisotropy. Slow tumbling and residual couplings are more likely to be problematic for large molecules like lipids, while diffusion is more significant for small molecules.

Our results in Fig. 5 indicate that spinning either fast or slow gives spectral intensities that are proportional (within the data scatter) to sample mass, and therefore quantitation should be possible under either spinning condition. The data obtained with faster spinning generally has higher intensity. This is expected, since faster HR-MAS rotation tends to reduce the effects of field inhomogeneities and dipolar couplings further, leading to the increase of the observed metabolic intensities.

Similar differences in individual metabolites measured at different HR-MAS rates and normalized by the STD intensity measured at the same spinning rate can be seen in Table 1. Since the absolute signal intensity of the rubber standard measured at 3.0 kHz is three times higher (3.06 ± 0.23) than its value obtained at 600 Hz under the same receiver gain, slopes smaller than 1.0 indicate that the metabolite intensities of these metabolites increased more than three times when the spinning rate increased from 600 Hz to 3.0 kHz. The observed differences in metabolite slopes should reflect the intrinsic differences in the physical state among these metabolites.

In conclusion, our results indicate that the rotor-synchronized DANTE sequence appears to be a useful method for generating HR-MAS spectra of human tissue with the simplicity and reproducibility valuable for disease diagnosis in a clinical setting.

ACKNOWLEDGMENTS

The authors thank Dr. Eva Ratai for careful reading of the manuscript.

REFERENCES

1. Sitter B, Sonnewald U, Spraul M, Fjosne HE, Gribbestad IS. High-resolution magic angle spinning MRS of breast cancer tissue. NMR Biomed 2002;15:327–337.
2. Waters NJ, Holmes E, Waterfield CJ, Farrant RD, Nicholson JK. NMR and pattern recognition studies on liver extracts and intact livers from rats treated with alpha-naphthylisothiocyanate. Biochem Pharmacol 2002;64:67–77.

3. Tzika AA, Cheng, LL, Goumnerova L, Madsen JR, Zurakowski D, Astrakas LG, Zarifi MK, Scott RM, Anthony DC, Gonzalez RG, Black PM. Biochemical characterization of pediatric brain tumors by using in vivo and ex vivo magnetic resonance spectroscopy. J Neurosurg 2002;96: 1023–1031.
4. Morvan D, Demidem A, Papon J, De Latour M, Madelmont JC. Melanoma tumors acquire a new phospholipid metabolism phenotype under cystemustine as revealed by high-resolution magic angle spinning proton nuclear magnetic resonance spectroscopy of intact tumor samples. Cancer Res 2002;62:1890–1897.
5. Chen JH, Enloe BM, Fletcher CD, Cory DG, Singer S. Biochemical analysis using high-resolution magic angle spinning NMR spectroscopy distinguishes lipoma-like well-differentiated liposarcoma from normal fat. J Am Chem Soc 2001;123:9200–9201.
6. Griffin JL, Williams HJ, Sang E, Nicholson JK. Abnormal lipid profile of dystrophic cardiac tissue as demonstrated by one- and two-dimensional magic-angle spinning (1)H NMR spectroscopy. Magn Reson Med 2001;46:249–255.
7. Schiller J, Naji L, Huster D, Kaufmann J, Arnold K. 1H and 13C HR-MAS NMR investigations on native and enzymatically digested bovine nasal cartilage. Magma 2001;13:19–27.
8. Barton SJ, Howe FA, Tomlins AM, Cudlip SA, Nicholson JK, Bell BA, Griffiths JR. Comparison of in vivo 1H MRS of human brain tumours with 1H HR-MAS spectroscopy of intact biopsy samples in vitro. Magma 1999;8:121–128.
9. Wind RA, Hu JZ, Rommereim DN. High-resolution (1)H NMR spectroscopy in organs and tissues using slow magic angle spinning. Magn Reson Med 2001;46:213–218.
10. Bodenhausen G, Freeman R, Morris GA. A simple pulse sequence for selective excitation in Fourier transform NMR. J Magn Reson 1976;23: 171–175.
11. Morris GA, Freeman R. Selective excitation in Fourier transform nuclear magnetic resonance. J Magn Reson 1978;29:433–462.
12. Piotto M, Saudek V, Sklenar V. Gradient-tailored excitation for single-quantum NMR spectroscopy of aqueous solutions. J Biomol NMR 1992; 2:661–665.
13. Dixon WT. Spinning-sideband-free and spinning-sideband-only NMR spectra in spinning sample. J Chem Phys 1982;77:1800–1809.
14. Antzutkin ON, Shekar SC, Levitt MH. Two-dimensional sideband separation in magic-angle-spinning NMR. J Magn Reson 1995;115A: 7–19.

Technology in Cancer Research & Treatment
ISSN 1533-0346
Volume 3, Number 6, December (2004)

Quantitative Pathology in Tissue MR Spectroscopy Based Human Prostate Metabolomics[§]

www.tcrt.com

Melissa A. Burns, B.A.[1]
Wenlei He, M.D., Ph.D.[1,2]
Chin-Lee Wu, M.D., Ph.D.[1,2]
Leo L. Cheng, Ph.D.[1,3,*]

Departments of:
[1]Pathology
[2]Urology
[3]Radiology
Massachusetts General Hospital
Harvard Medical School
Pathology Research
CNY-7, 149, 13th Street
Charlestown, MA 02129 USA

At present, the clinical utility of metabolomic profiles of human prostate tissue relies on the establishment of correlations between metabolite data and clinical measurements, particularly pathological findings. Because metabolomics is a quantitative study, its clinical value can be rigorously investigated by determining its association with other quantitative measures. The human visual assessment of prostate tissue, however, introduces both inter- and intra-observer biases that may limit the reliability of its quantitations, and therefore, the strength of its correlations with metabolomic profiles. The aim of this study was to develop a simple, feasible protocol for the computer-aided image analysis (CAIA) of prostate pathology slides in order to achieve quantitative pathology from tissue samples, following metabolomic measurement with high-resolution magic angle spinning (HRMAS) magnetic resonance spectroscopy (MRS). Thirty-eight samples from 29 prostatectomy cases were studied with HRMAS MRS. After spectroscopy analysis, samples were serial-sectioned, stained and visually assessed by pathologists. Cross-sections from these samples were then measured with the CAIA protocol. Results showed a two-fold difference between human visual assessments of the area percentages of tissue pathologies and CAIA area percentages obtained for the same features. Linear correlations were found between both metabolites indicative of normal epithelium and those indicative of prostate cancer, and the CAIA quantitative results. CAIA based quantitative pathology is more reliable than human visual assessment in establishing correlations useful for disease diagnosis between prostate pathology and metabolite concentrations.

Key words: Image analysis, Pathology, Human prostate, Computer-Aided, Magnetic resonance, Metabolomics.

Introduction

The emergence of the fields of human genomics, proteomics and metabolomics has aided the discovery of potential molecular markers for disease, thus defining the diagnostics and prognostics of the current era of molecular pathology.

Genomic advancements, such as the identification of gene mutations, contribute to the understanding of genetic markers of disease and disease risks. However,

* Corresponding Author:
L. L. Cheng, Ph.D.
Email: cheng@nmr.mgh.harvard.edu

Abbreviations: MRS, Magnetic resonance spectroscopy; CAIA, Computer-aided image analysis; HRMAS, High-resolution magic angle spinning; PSA, Prostate-specific antigen; PCa, Prostate cancer; GU, Genitourinary; IRB, Institutional Review Board; STD, External standard; ROI, Regions of interest; H&E, Hematoxylin and eosin; Cit, Citrate; Cho, Choline; PCh, Phospocholine.

[§] We wish to dedicate this work to the memory of Mr. Randall K. "Randy" Burns, the beloved father of M. A. Burns, who died of prostate cancer on February 21, 2004, at age 57.

such knowledge may not reflect the present clinical status and the biochemical activity of disease, or the potential capacity of this activity to forecast patient prognosis and disease progression, particularly in oncogenesis (1, 2).

Proteomics, however, has produced molecular biological knowledge that may be more relevant to the cancer clinic. Currently, tests which detect and quantify a single protein, such as prostate-specific antigen (PSA) present in blood, have been used in prostate cancer (PCa) screening. However, these screening tests are known to be of low specificity, though this may be improved by combining them with other evaluations such as biopsy (3-7) in order to reduce the incidence of false-positives generated by the presence of benign conditions (8, 9). Furthermore, even with the aid of biopsy, current molecular screenings used in the PCa clinic are unable to determine virulent from indolent cancers, which may result in the over-treatment (*i.e.*, interventions for tumors that would otherwise go unnoticed in a patient's lifetime) of as many as 30% of PCa cases (10, 11).

Metabolomics, in studying the complement of all measurable metabolites, seeks to define the levels, activities, interactions, and regulation of all metabolites in a biological system, and to investigate any changes in these quantities or activities in response to internal and external stimuli, such as disease processes. Metabolomic changes can be considered the ultimate response, a kind of molecular phenotype, of biological systems to both genetic and environmental stimuli. As such, it is expected that metabolomic changes most often occur before the manifestation of any morphological changes. Thus, metabolomic evaluation can be extremely useful, especially in the diagnosis and prognosis of human malignancies, where prognostic factors may be more strongly determined by the patient, the treatment, and the environment than by the tumor itself (12). At present, metabolomic technologies are represented almost entirely by magnetic resonance spectroscopy (MRS) and, to some extent by mass spectrometry. MRS is an objective technique, able to detect and quantify biochemical species, thereby capable of generating metabolomic profiles of normal tissue and of disease (13). High-resolution magic angle spinning (HRMAS) proton MRS for intact tissue analysis generates tissue spectra well enough resolved to allow the identification and quantification of individual metabolites from unaltered human specimens, while preserving tissue pathological structure, so that MRS results can be correlated directly with subsequent histopathological measurements.

Metabolomic studies have made evident the difference in emphasis between the pathological evaluations in the current era of molecular pathology, and those of the morphological pathology of the past century. The traditional morphology-based pathology, reporting mostly the presence or absence of certain pathological features, has been the gold standard in the diagnosis of human malignancies. However, its analysis is limiting to the interpretation of results measured in the fields of "-omics," because parameters measured by proteomics and metabolomics are continuous, proportional to the mass of the analyzed sample, and in flux throughout the development and progression of disease. Therefore, the quantitative evaluation of pathological features is particularly appropriate to the study of tissue metabolomics, and is required in order to maximize the utility of spectroscopic results.

Computer-aided image analysis (CAIA) has been recognized in the era of molecular pathology as a useful tool for providing objective and quantitative data. While most studies employing CAIA have focused on its ability to detect subtle changes in cell nuclear morphology that may not be visible to the human eye, CAIA is able also to identify and quantify cellular components, with objectivity and virtual independence from inter- and intra-observer variabilities.

In this study, we tested a CAIA protocol developed for differentiating and quantifying cellular components (normal glands, stroma, and cancer glands) of H/E stained prostate tissue sections. We examined correlations of the quantitative results obtained using the CAIA protocol, with those obtained by the visual assessments of experienced GU pathologists. More importantly, we demonstrated that the results of CAIA pathology correlated more strongly than the pathologists' visual quantifications with tissue metabolic intensities, measured with HRMAS proton MRS from the same specimens. Therefore, the development and implementation of CAIA procedures for quantitative pathology may be critical to the further realization of tissue metabolomic's potential for understanding and diagnosing disease.

Materials and Methods

Tissue Protocol

MRS analysis and histopathological evaluation of human prostate samples were approved by the Institutional Review Board (IRB) at the Massachusetts General Hospital.

Tissue samples (n=38 from 29 prostatectomy cases) were snap frozen in liquid nitrogen and stored at -80 °C until spectroscopic analysis. Following spectroscopic analysis, tissue samples were fixed in 10% formalin, embedded in paraffin, cut into 5-micron sections at either 100 (20/38 samples), or 200 (18/38 samples) micron intervals, and stained with hematoxylin and eosin (H&E). The percentages of areas (area%) representing normal epithelial glands (including lumen), stroma, and cancer glands (including lumen) in each cross-section were estimated independently to the nearest 5% by two GU pathologists, who had neither prior knowledge of the spectroscopic results nor the other pathologist's reading. The independent readings were then averaged to obtain an area% for each cross-section.

CAIA was then applied to the tissue cross-sections. Of the 38 tissue samples selected for CAIA tests, the 15 cancer-negative samples were selected randomly from more than 200 measured samples, while the 23 cancer-positive samples represent all cancer-positive samples observed before the manuscript was prepared. All samples had undergone the same spectroscopy and histopathology procedures before they were used to test CAIA. Prostate cancer cases were selected for CAIA after cancer was diagnosed by the participating pathologists; however, CAIA results were generated independently from the quantitative measurements given by the pathologists.

High Resolution Magic Angle Spinning (HRMAS) Proton MRS

The MRS experiments were carried out on a Bruker (Bruker BioSpin Corp., Billerica, MA) AVANCE spectrometer operating at 600 MHz (14.1T). The sample was placed in a 4 mm zirconia rotor with Kel-F plastic inserts which created a spherical sample space of ~10 µl located at the center of the detection coil. A small (~0.1 mg) silicone rubber sample was permanently fixed inside one of the Kel-F spacers, positioned within the detection coil but not in contact with the sample, to function as an external standard (STD) for both frequency reference (0.06 ppm from TMS) and quantification. Prostate tissue samples (8-10 mg) were used directly from freezers without further preparation. Approximately 1.0 µl of D_2O was added to each sample for ^2H field locking. The sample was introduced into the probe pre-cooled to 3 °C for HRMAS MRS measurements at that temperature. The rotor spinning rate accuracy (±1.0 Hz) was controlled with an MAS controller and verified with the positions of spinning sidebands in the spectra.

Spectra were acquired with the spectrometer frequency set exactly on the water resonance. Of the 15 cancer-negative samples reported for correlations between CAIA and human visual assessment, 12 were measured under the same spectroscopic conditions with a spinning rate of 3kHz, and thus were selected for the analysis of correlations between quantitative pathology and tissue metabolite concentrations. Similarly, 19 of the 23 cancer-positive samples, reported for correlations between CAIA and human visual assessment, were analyzed using a rotor-synchronized Carr-Purcell-Meibom-Gill sequence with a total of 20ms delay after the 90° excitation pulse, and with a spinning rate of 700Hz. These 19 spectra also were selected for tissue metabolic concentration analysis. Each spectrum was acquired with 32 transients and a repetition time of 5s.

Spectroscopic data were processed using the Nuts software (Acorn NMR Inc., Livermore, CA) according to the following procedures. All free induction decays were subjected to 0.5 Hz apodization before Fourier transformation, baseline correction, and phase adjustment. Resonance intensities reported here represent integrals of curve-fittings with Lorentzian-Gaussian line-shapes normalized by the STD intensity measured for each sample. All intensities reported here in the context of quantification were area intensities obtained from curve fitting. Tissue cellular metabolite concentrations were calculated based on the intensity ratios of metabolites over the intensity of the H_2O peak at ~5.0ppm.

Computer Aided Image Analysis

Quantitative pathological analysis was applied using an Olympus BX41 Microscope Imaging System (Olympus American, Inc., Melville, NY) in conjunction with image analyzer MicroSuite™ (Soft Imaging System Corp., Lakewood, CO). Digital photographs were taken of each cross-section at 10× magnification. It was necessary to take multiple photographs in order to capture the entire cross-section. The multiple image alignment feature, available in MicroSuite™, confirmed that the entire cross-section had been captured without overlapping regions.

For each image of normal prostate tissue, regions of interest (ROI) were selected and initial color thresholds set for the differential detection of stroma, glandular epithelium, and glandular lumen. Using these color thresholds, the classification type "3Phases" was created. In addition, the "define measurement, detection, and classification settings" were specified as follows: minimum pixel size: 100 pixels, border particles: truncated, search area: ROI, pixel connectivity includes "diagonals [8]." Criterion set at "Phases," classification set at "3Phases," filled style, and ID particle > 100 pixels. Each image underwent the above "3Phases" detection protocol with RGB/HSI filters and ROI were adjusted in each case for optimal detection. Using the "Measure Area/Perimeter" tool, the total area of the image was calculated. All data generated from images within an individual cross-section were summed to generate the total area, and the area and area% stroma, glandular epithelium, and glandular lumen of each cross-section. Similarly, all data from individual cross-sections within a sample were summed, thus establishing a total representative volume, and the volume and volume percentage (vol%) of each individual component.

For cancerous tissues (determined by human visual assessment) a distinct classification system was created. ROI were selected within a cancerous tissue cross-section that, in general, were representative of expected prostate cancer tissue characteristics. Initial color thresholds were set using these ROI to detect both cancerous cells and their respective lumenal area, creating the classification type "cancer glands." All "define measurement, detection, and classification settings" were the same as for normal tissues except classification type was set at "cancer glands," and minimum pixel size and ID particle size > were set at 50 pixels in order to accommodate small cancerous foci. As with the normal tissue, when the "cancer glands" classification protocol was applied to an image, ROI were manually selected, and RGB/HSI filters were adjusted for optimal detection of cancerous glands. Data from individual images within a cross-section and separately, data from individual cross-sections within a sample, were summed in order to calculate the area and area%, and volume and volume%, respectively, of cancer cells and lumen.

Due to the lengthy procedure for analyzing images of cancerous, H&E-stained samples, not all cross-sections of a case were measured individually; instead images from each sample were selected on the basis of the area% cancer determined by the pathologists, such that a new cross-section was selected for analysis for every difference greater than 10%. In general, two to three cross-sections were selected from each sample consisting of between six and thirteen cross-sections. The volume% of cancer cells and lumen for the sections that were not measured with CAIA were estimated based on results of adjacent and quantified sections.

Results

Determining Optimal Frequency of Pathology Serial-sectioning Using CAIA

Figure 1, an example of "3Phases" CAIA, and "cancer glands," shows the results of the CAIA classification scheme applied to a cross-section of human prostate tissue containing both normal and cancerous glands. Particularly, stroma, normal glandular epithelium (red), and normal glandular lumen (yellow) were identified using "3Phases" classification protocol, as seen in (b). Image (c) shows an image of a tissue section that underwent "cancer glands" classification, with cancer cells and lumen labeled in blue and light blue, respectively.

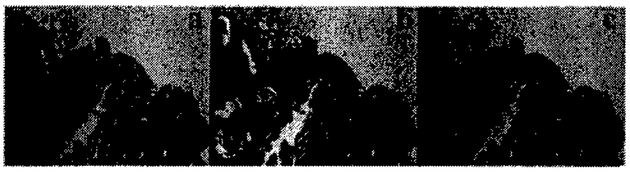

Figure 1: A digital photograph of the upper right quadrant of a cross section of prostate tissue with both cancerous and normal glands was taken using an Olympus BX41 Microscope Imaging System (Olympus American, Inc., Melville, NY) with 10× magnification (**a**). Using image analyzer MicroSuite™ (Soft Imaging System Corp., Lakewood, CO) "3Phases" classification analysis was performed on the image, resulting in the labeling of all normal glands (**b**) and stroma (not labeled in the image). In addition, the "cancer glands" classification scheme was also applied; image (**c**). For clarification regarding "3Phases" and "cancer glands" classification analyses, refer to ***Materials and Methods*** section of text.

To determine the effect of reducing the frequency of pathology serial sectioning on the reconstructions of volume percentages of tissue features, all slides from the 15 cancer-negative human prostate tissue samples were analyzed using the "3Phases" classification scheme. Ten samples were cut at intervals of 200 μm, while the remaining five were cut at 100 μm intervals. In Figure 2, vol% of epithelium (from CAIA) with and without lumen of every sample were plotted (on the horizontal axis) against vol% epithelium with and without lumen, calculated using only odd-numbered sections (on the vertical axis) for both 100 μm (a, b) and 200 μm (c, d) interval sections. The linearity of all four plots indicates that sections cut at 100 μm intervals were not remarkably different from those cut at 200 μm intervals, and similarly, vol% components from those cut at 200 μm intervals varied little when examined at 400 μm intervals. Hence, Figure 2 illustrates that CAIA may be used to estimate the optimal frequency of serial sectioning for the quantification of tissue pathologies. In this case, the results showed that for analyzing normal tissues using CAIA, a frequency of 400 μm would be sufficient for the calculation of the vol% of cellular components. It is possible that cancerous glands may be smaller and shallower than normal glands. However, visual assessment of adjacent pathology images suggests that similar area% were

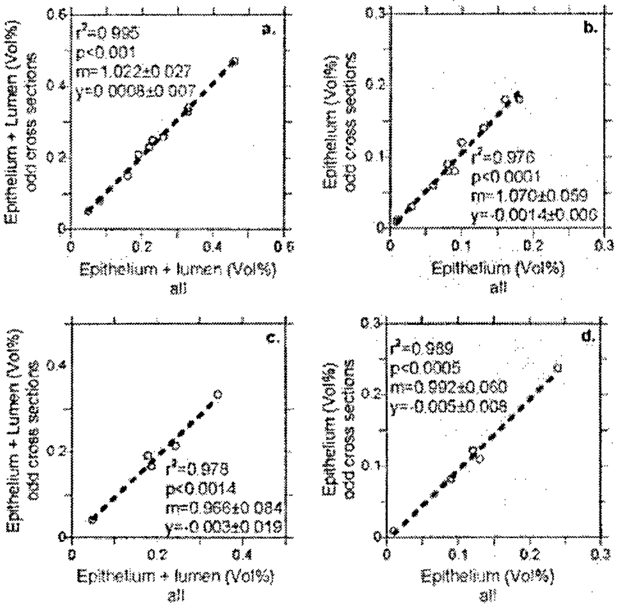

Figure 2: Highly significant direct correlations were observed between both total vol% of normal epithelium and lumen and vol% of normal epithelium and lumen, calculated using only odd cross-sections at intervals of both 200 microns and 400 microns, (**a**) and (**c**) respectively. Similarly, (**b**) and (**d**) show that slopes of virtually m=1 were also observed between total vol% and odd cross-section vol% of normal epithelium only cut at intervals of 200 and 400 microns, respectively. Essentially, this suggests that sectioning need only occur at 400 micron intervals, as there exist no appreciable differences in percent composition at 100, 200, or 400 micron intervals.

seen at sequential intervals both for cross-sections cut every 100 μm and those cut every 200μm.

CAIA Determinations of the Percentages of Areas/Volumes of Prostate Tissue Features are Strongly Correlated with the Determinations of Human Visual Assessment

Despite the linear correlations between results of CAIA and human estimations, it was found that there were significant differences between human pathological assessment of the area% of pathological features of interest and CAIA quantification of the same feature areas. This is shown in Figures 3 and 4, where the area% (i.e. cross-sections) and vol% (i.e. samples) of normal epithelium + lumen and cancer cells + lumen are presented, respectively.

Figures 3(a) and (b) show statistically significant linear relationships of the area% (a), R^2=0.67 $p<0.0001$, and vol% (b), R^2=0.67 $p<0.0002$, of normal glands (epithelium and lumen) as measured by CAIA, with the average of the pathologists' estimates of these values. When comparing CAIA (y-axis) with the pathologists' estimates (x-axis), both area% and vol% of normal glands indicated similarly sloping linear relationships, 0.46±0.03 and 0.49±0.10; that is, values from the human estimates amounted to about twice those determined by CAIA.

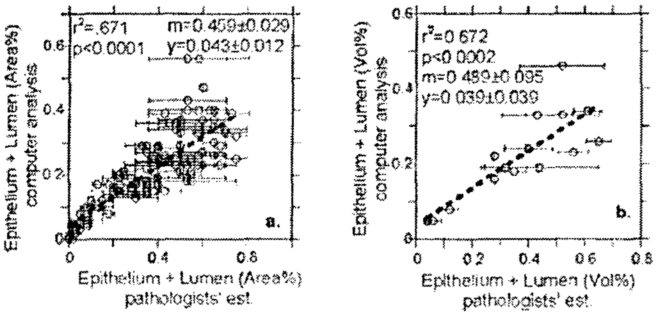

Figure 3: The observed linear correlations between both area% and vol% of normal glands from pathologists' estimations and area% and vol% of normal glands from "3Phases" computer analysis, (a) and (b) respectively. Similar slopes from (a), 0.459±0.029, and (b), 0.489±0.095, suggest that there tends to be approximately a two-fold difference of the percentages of normal epithelium and lumen between human pathological assessments and CAIA results.

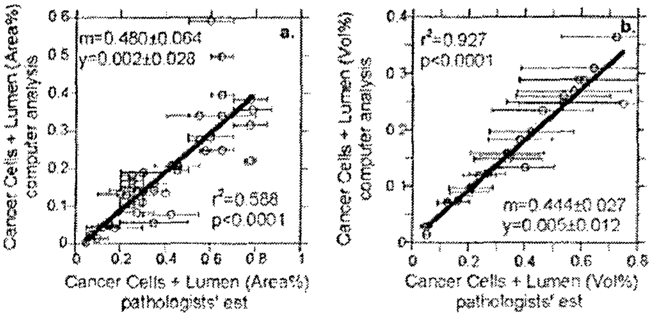

Figure 4: Statistically significant linear correlations observed between area% and vol% of cancer glands (cancer cells + lumen) as estimated by human pathological assessment and area% and vol% of cancer glands as detected using "cancer glands" classification scheme, (a) and (b) respectively. Slopes of 0.480±0.064 (a) and 0.444±0.027 (b) show two-fold difference between human assessments and CAIA results also exists for estimating the percentage of cancerous glands in human prostate tissue.

Similarly, Figure 4 shows linear relationships between the averages of the pathologists' estimates of both area% and also vol% cancer glands (cells and lumen), and the results generated by CAIA, R^2=0.59 $p<0.0001$ and R^2=0.93 $p<0.0001$, respectively. The slopes for area% and vol% of cancer glands were 0.48±0.06 and 0.44±0.03, respectively. Again, these statistically significant slope values suggest that there is a two-fold difference between visual assessment and computer quantification.

Correlation of Metabolite Intensities to Prostate Pathology

Since HRMAS proton MRS does not alter prostate tissue intactness and pathological architectures, subsequent pathological assessment can be performed on the same samples to evaluate the critical correlations between metabolite concentration and vol% of cellular pathologies. The spectrum in Figure 5 is an example of the metabolic region of interest (4.8 ppm to -0.2 ppm) with a number of tissue cellular metabolites labeled: citrate (Cit), polyamines including spermine, choline (Cho) and phospocholine (PCh). These metabolites were chosen because they have been shown to be associated with prostate cancer growth (14-18). The metabolic intensities for those four metabolites were normalized by the intensity of the water peak at ~5.0 ppm (from a fully-relaxed spectrum, not shown) in order to derive the absolute metabolic concentration. In Figure 6, metabolic concentrations for Cit and polyamines were plotted against

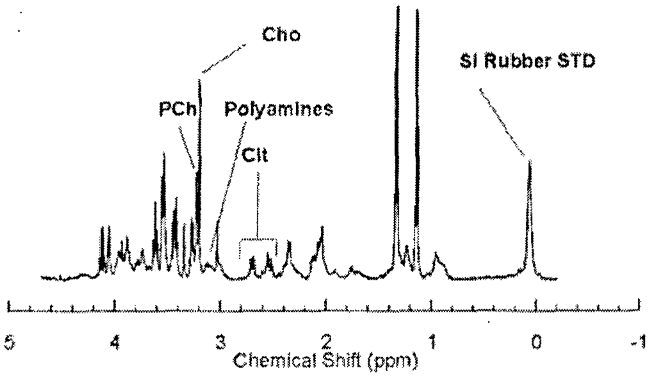

Figure 5: Proton HRMAS spectrum of a sample of cancerous human prostate tissue with metabolites of interest, as well as the SI Rubber STD, labeled. The spectrum was measured using a rotor-synchronized CPMG sequence with a total of 20ms delay after the 90° excitation pulse and with a spinning rate of 700Hz.

the vol% of epithelium with lumen (Fig. 6a), and without lumen (Fig. 6b) calculated by CAIA. Linear correlations were observed between concentrations of both Cit and polyamines and the vol% of epithelium with and without lumen. However there were no linear correlations observed between metabolic concentration and vol% lumen, which may suggest that both Cit and the polyamines, thought to be secreted metabolites, are secreted as a function of the amount of normal epithelia present in the tissue (19, 20).

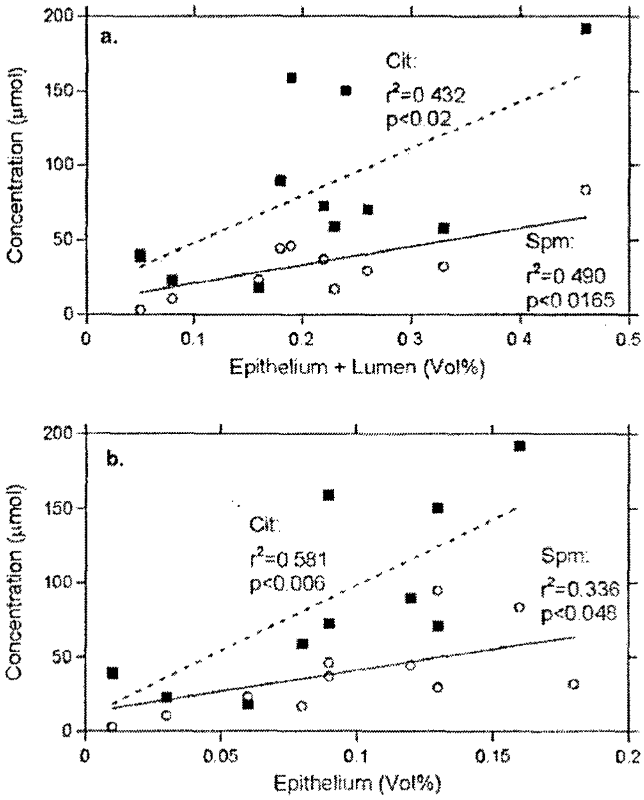

Figure 6: Linear correlations between concentration (μmol) of polyamines (Spm, ?) and citrate (Cit, ?) and vol% of normal glands (a) and of normal tissue epithelium only (b), measured from the same tissue sample after NMR measurement using "3Phases" computer analysis.

Figure 7 shows linear correlations observed between the vol% cancer (with and without lumen) calculated from CAIA, and Cho and PCh + Cho, respectively. Of importance, when the metabolic concentrations were plotted against the vol% cancer determined by human visual assessment, no correlations existed. Additionally, there was no correlation observed between vol% lumen and metabolic concentrations when vol% was determined by human estimation. Again, these observations suggest both that CAIA may be more sensitive than human visual quantification of pathological features and that the levels of Cho and PCh present in a tissue sample are intrinsically related and proportional to the amount of cancerous cells in that sample. This is consistent with the known fact that malignant transformation is connected to substantial geometric remodeling of the pore, or lumenal space (21).

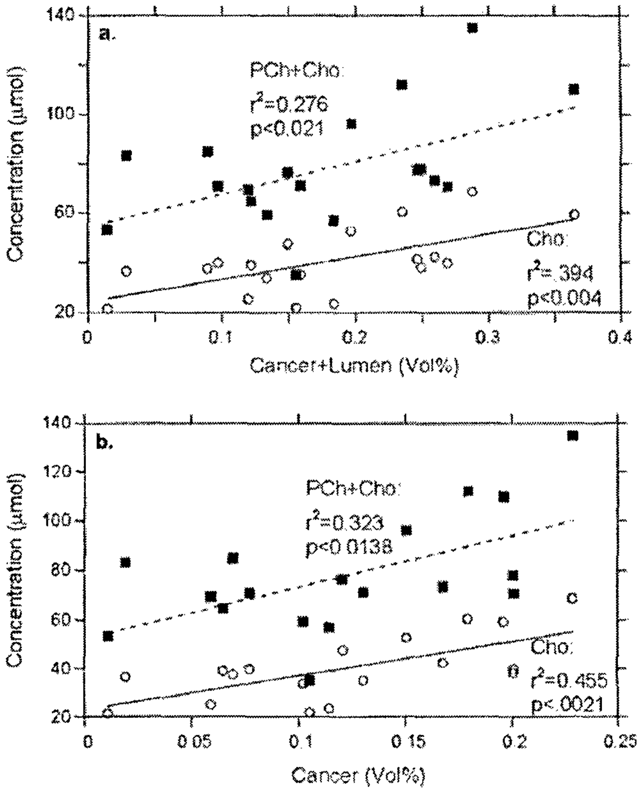

Figure 7: Linear correlations between the concentrations (μmol) of choline (Cho, ?) and the sum of phosphocholine plus choline (PCh + Cho, ?) and the vol% of cancer glands (a) and of cancer cells only (b) measured from the same tissue sample after NMR measurement using image analyzer MicroSuite™ and the "cancer glands" classification scheme. No correlation was identified when human pathologists' estimations were used in place of the computer-aided quantitative pathology measurements.

Discussions

The method presented, CAIA for quantitative pathology, has the ability to provide a powerful adjunct tool for metabolomic research using HRMAS proton MRS. Although this study was developed due to the necessity of performing tissue pathological quantification after HRMAS MRS measurements in order to identify potential biomolecular markers for disease diagnosis, its conclusions are generally applicable to other molecular pathology studies where both the presence and quantity of certain pathological features are of interest. Currently, human visual assessment of prostate pathology is used for comparison with metabolite concentration. However, human visual assessment introduces both inter- and intra- observer biases that may inhibit the determination of statistically significant correlations. The CAIA method described here provides a simple, reproducible, and reliable method of pathological assessment that is free of both inter- and intra-observer biases.

Validity and Current Limitations of Computer-aided Quantitative Pathology using MicroSuite™

Currently, limitations in the software available for CAIA necessitate a reliance on human visual assessment to distinguish normal from cancerous glands in clinic. This distinction is based on tissue architecture and cellular characteristics, and cannot be made simply based on the color of the H&E staining and the lumenal areas, as in CAIA. Therefore, it is essential that tissue undergoing CAIA be classified as cancer-negative or cancer-positive before CAIA, and that glands of images coded using "cancer glands" classification schemes be assessed after CAIA for the detection of any false positives, as was done in this study by the participating pathologists.

This limitation may be alleviated when other cancer cell specific immuno-stainings are incorporated. However, even at present, while the aid of expert pathologists is still necessary for the determination of normal versus cancerous glands, the computer classification protocols "3Phases" and "cancer glands" have shown the ability to produce objective results free of inter-observer bias. Since the computer classification schemes have fixed parameters that are used for every image, are the same for every tissue being studied, and are independent of the person performing the CAIA, inter-, as well as intra-, observer biases are not of concern. For instance, to determine whether CAIA is more consistent than human visual assessment, one sample of normal human prostate tissue containing 13 cross-sections was reanalyzed using the "3Phases" classification protocol. In addition, these cross-sections were also reread at a later date by one of the pathologists who initially read this sample. From the given results, the reproducibility of the CAIA is markedly better than inter-observer bias ($m=0.91\pm0.08$, y-intercept$=0.04\pm0.03$ versus $m=0.62\pm0.06$, y-intercept$=0.15\pm0.04$ for CAIA and visual, respectively), and slightly better than intra-observer bias for which both measurements approach unity and the origin, but for which $r^2_{\text{computer analysis}}$ is slightly more significant than $r^2_{\text{intraobserver bias}}$ ($r^2=0.92$ and $r^2=0.90$, respectively).

Potentially, technical advances in image analysis software will allow the fully automated detection of cellular components, including the detection of cancerous cells and/or glands with specific immunochemical stainings. However, with the minimal costs of H&E staining, the method used in this study, selecting for CAIA the cross-sections that represent large differences in area% of cellular components within a sample, is reliable based upon the correlations observed between vol% cancer and the metabolites Cho and PCh + Cho.

Correlations Between Tissue Pathology and Metabolite Concentrations

Using human visual assessment to estimate the vol% of tissue components for a sample, such as a prostate biopsy core, may be unreliable. Although calculating vol% is possible with the aid of a simple computer analysis to map the area of each tissue section within a sample, additional errors are introduced, making this method less reliable than the CAIA method presented in this report. Additionally, accurate determination of area% of epithelium or cancer without lumen is very difficult with human visual assessment due to the generally ring-like structures of the glandular epithelium and cancer cells. However, using the classification schemes presented in this report, determining the area% of such cellular components is facile. The ease and accuracy with which this determination is made allowed for the novel determination that the lumenal areas, both normal and cancerous, do not contribute to the correlations observed between metabolic concentrations and prostate pathologies. Such observations fuel metabolomics, which is concerned with metabolite levels that are continuously changing and evolving as a disease develops and progresses.

Pathologists do not often consider the area and volume percentages of each pathological structure as components of the whole tissue section or biopsy core, respectively. Rather, they rely on qualitative descriptions rather than quantitative data when making a diagnosis. Although quantitation is not of the interest of the traditional anatomic pathology, it has gained attention in the era of molecular pathology, in which both genomic expressions and proteomic profiles are presented quantitatively. Here we suggest that by comparing quantitative pathological data with metabolomic profiles, new diagnostic criteria may be established. However, as a preliminary evaluation, only the simple, linear regression method is used to demonstrate this principle. Such a simplified treatment of the complexity of cellular metabolism inevitably injects errors in the results, which likely explain the observed R^2 values presented in Figures 6 and 7 for metabolite correlations. Nevertheless, with the establishment of the principle and the implementation of sophisticated paradigms for tissue metabolite analyses, in the near future, metabolic criteria may be used in prostate biopsy to provide a more definitive diagnosis and allow for closer monitoring of suspicious foci than is currently possible.

Conclusions

The reported results indicate that CAIA for use in quantitative pathology may provide more reliable results than human visual assessment, and may allow for the observation of stronger correlations between prostate pathologies and metabolite concentrations measured with HRMAS proton NMR spectroscopy. In addition, this method is useful in the determination of certain technical aspects, such as the optimal frequency of pathology sections, and the determination of which specific components, for example epithelium or lumen, correlate with the measured metabolite intensities. Furthermore, the ease and efficiency with which different classification schemes can be created allow for future extension to other cancers, diseases, and types of tissue.

Acknowledgements

We wish to thank Ms. D. Ashley Feldman for editorial assistance. This work is supported in part by PHS/NIH grants CA095624 and EB002026; and in part by a DOD grant W81XWH-04-1-0190.

References

1. Dove, A. Proteomics: Translating Genomics into Products? *Nat. Biotechnol. 17*, 233-236 (1999).
2. Binz, P. A., Muller, M., Walther, D., Bienvenut, W. V., Gras, R., Hoogland, C., Bouchet, G., Gasteiger, E., Fabbretti, R., Gay, S., Palagi, P., Wilkins, M. R., Rouge, V., Tonella, L., Paesano, S., Rossellat, G., Karmime, A., Bairoch, A., Sanchez, J. C., Appel, R. D., and Hochstrasser, D. F. A Molecular Scanner to Automate Proteomic Research and to Display Proteome Images. *Anal. Chem. 71*, 4981-4988 (1999).
3. Steinert, R., von Hoegen, P., Fels, L. M., Gunther, K., Lippert, H., and Reymond, M. A. Proteomic Prediction of Disease Outcome in Cancer: Clinical Framework and Current Status. *Am J Pharmacogenomics 3*, 107-115 (2003).
4. Stenman, U. H., Leinonen, J., Alfthan, H., Rannikko, S., Tuhkanen, K., and Alfthan, O. A Complex Between Prostate-specific Antigen and Alpha 1-antichymotrypsin is the Major Form of Prostate-specific Antigen in Serum of Patients with Prostatic Cancer: Assay of the Complex Improves Clinical Sensitivity for Cancer. *Cancer Res. 51*, 222-226 (1991).
5. Catalona, W. J., Partin, A. W., Slawin, K. M., Brawer, M. K., Flanigan, R. C., Patel, A., Richie, J. P., deKernion, J. B., Walsh, P. C., Scardino, P. T., Lange, P. H., Subong, E. N., Parson, R. E., Gasior, G. H., Loveland, K. G., and Southwick, P. C. Use of the Percentage of Free Prostate-specific Antigen to Enhance Differentiation of Prostate Cancer from Benign Prostatic Disease: A Prospective Multicenter Clinical Trial. *Jama 279*, 1542-1547 (1998).
6. Israeli, R. S., Powell, C. T., Corr, J. G., Fair, W. R., Heston, W. D. Expression of the Prostate-specific Membrane Antigen. *Cancer Res. 54*, 1807-1811 (1994).
7. Ito, K., Yamamoto, T., Ohi, M., Takechi, H., Kurokawa, K., Suzuki, K., and Yamanaka, H. Natural History of PSA Increase With and Without Prostate Cancer. *Urology 62*, 64-69 (2003).
8. Carter, H. B. and Isaacs, W. B. Improved Biomarkers for Prostate Cancer: A Definite Need. *J. Natl. Cancer Inst. 96*, 813-815 (2004).
9. Zackrisson, B., Aus, G., Lilja, H., Lodding, P., Pihl, C. G., and Hugosson, J. Follow-up of Men with Elevated Prostate-specific Antigen and One Set of Benign Biopsies at Prostate Cancer Screening. *Eur. Urol. 43*, 327-332 (2003).
10. Draisma, G., Boer, R., Otto, S. J., van der Cruijsen, I. W., Damhuis, R. A., Schroder, F. H., and de Koning, H. J. Lead Times and Overdetection Due to Prostate-specific Antigen Screening: Estimates from the European Randomized Study of Screening for Prostate Cancer. *J. Natl. Cancer Inst. 95*, 868-878 (2003).
11. Etzioni, R., Penson, D. F., Legler, J. M., di Tommaso, D., Boer, R., Gann, P. H., and Feuer, E. J. Overdiagnosis Due to Prostate-specific Antigen Screening: Lessons from U.S. Prostate Cancer Incidence Trends. *J. Natl. Cancer Inst. 94*, 981-990 (2002).
12. Fiehn, O. Metabolomics – The Link Between Genotypes and Phenotypes. *Plant Mol. Biol. 48*, 155-171 (2002).
13. Defernez, M. and Colquhoun, I. J. Factors Affecting the Robustness of Metabolite Fingerprinting Using 1H NMR Spectra. *Phytochemistry 62*, 1009-1017 (2003).
14. van der Graaf, M., van den Boogert, H. J., Jager, G. J., Barentsz, J. O., and Heerschap, A. Human Prostate: Multisection Proton MR Spectroscopic Imaging with a Single Spin-echo Sequence – Preliminary Experience. *Radiology 213*, 919-925 (1999).
15. Males, R. G., Vigneron, D. B., Star-Lack, J., Falbo, S. C., Nelson, S. J., Hricak, H., and Kurhanewicz, J. Clinical Application of BASING and Spectral/Spatial Water and Lipid Suppression Pulses for Prostate Cancer Staging and Localization by *In Vivo* 3D 1H Magnetic Resonance Spectroscopic Imaging. *Magn. Reson. Med. 43*, 17-22 (2000).
16. Hahn, P., Smith, I. C., Leboldus, L., Littman, C., Somorjai, R. L., and Bezabeh, T. The Classification of Benign and Malignant Human Prostate Tissue by Multivariate Analysis of 1H Magnetic Resonance Spectra. *Cancer Res. 57*, 3398-3401 (1997).
17. Cheng, L. L., Wu, C., Smith, M. R., and Gonzalez, R. G. Non-destructive Quantitation of Spermine in Human Prostate Tissue Samples Using HRMAS 1H NMR Spectroscopy at 9.4 T. *FEBS Lett. 494*, 112-116 (2001).
18. Swanson, M. G., Vigneron, D. B., Tabatabai, Z. L., Males, R. G., Schmitt, L., Carroll, P. R., James, J. K., Hurd, R. E., and Kurhanewicz, J. Proton HR-MAS Spectroscopy and Quantitative Pathologic Analysis of MRI/3D-MRSI-targeted Postsurgical Prostate Tissues. *Magn. Reson. Med. 50*, 944-954 (2003).
19. Lao, L., Franklin, R. B., and Costello, L. C. High-affinity L-aspartate Transporter in Prostate Epithelial Cells that is Regulated by Testosterone. *Prostate* 22, 53-63 (1993).
20. Cohen, R. J., Fujiwara, K., Holland, J. W., and McNeal, J. E. Polyamines in Prostatic Epithelial Cells and Adenocarcinoma: The Effects of Androgen Blockade. *Prostate 49*, 278-284 (2001).
21. Mattfeldt, T., Schmidt, V., Reepschlager, D., Rose, C., and Frey, H. Centred Contact Density Functions for the Statistical Analysis of Random Sets. A Stereological Study on Benign and Malignant Glandular Tissue Using Image Analysis. *J. Microsc. 183*, 158-169 (1996).

Date Received: August 23, 2004

Dr. L. L. Cheng

From: MRM MRM [MRM@hmc.psu.edu]
Sent: Friday, January 28, 2005 9:30 AM
To: cheng@nmr.mgh.harvard.edu
Subject: Accepted MRM-104-6951

Copyright Agreement.pdf
6951 Accept Letter.pdf

Dear Dr. Cheng,

Congratulations! Your manuscript has been accepted for publication in MRM. Attached is the official acceptance letter in PDF.

***Please pay particular attention to the instructions in the attached letter for submitting the electronic version of the manuscript.

Also, please sign the attached Wiley copyright agreement form (which is also in PDF format) and send it to the publisher. Please be sure to fill in the manuscript number in the space indicated "ID #" in the upper right hand corner of the first page of the form. If you have trouble opening the attached PDF version of the copyright form, the ISMRM Copyright Transfer Agreement is also available for download at the following website: http://www.interscience.wiley.com/jpages/0740-3194/info.html .

Thank you for your cooperation.

Sincerely,
Shannon

PUBLISHER'S CONTACT INFO:

Andrea Ritola
Wiley and Sons, STM Division
111 River Street, 8th floor
Hoboken, NJ 07030
Phone# 201-748-6550
Email: aritola@wiley.com

Shannon Stepanian
Editorial Assistant
Magnetic Resonance in Medicine
Penn State College of Medicine
Radiology, NMR Building, H066
500 University Drive
Hershey, PA USA
Phone: 717-531-4305
Fax: 717-531-0684
mrm@hmc.psu.edu

Reduction of Spinning Sidebands in Proton NMR of Human Prostate Tissue with Slow High Resolution Magic Angle Spinning

Melissa A. Burns[1], Jennifer L. Taylor[1], Chin-Lee Wu[1], Andrea G. Zepeda[1],
Anthony Bielecki[3], David Cory[4], Leo L. Cheng[1,2,*]

[1]Department of Pathology, [2]Department of Radiology, Massachusetts General Hospital,
Harvard Medical School, Boston, Massachusetts;
[3]Francis Bitter Magnet Laboratory, [4]Department of Nuclear Engineering,
Massachusetts Institute of Technology, Cambridge, Massachusetts.

Running Title: Min(A, B,…, N) in Slow Spinning HRMAS ^{1}HNMR.

[*]**Correspondence to:** Leo L. Cheng, Pathology Research, CNY-7, 149 13th Street, Charlestown, MA 02129; 617-724-6593 (Phone); 617-726-5684 (Fax); E-mail: cheng@nmr.mgh.harvard.edu.

Abstract

High-resolution magic angle spinning (HRMAS) NMR spectroscopy has proven useful for intact tissue analysis, permitting correlations between tissue metabolites and disease pathologies. Extending these studies to slow spinning methodologies helps protect tissue pathological structures from HRMAS centrifuging damage and may permit the study of larger objects. Spinning sidebands (SSBs), produced by slow spinning, must be suppressed in order to prevent the complication of metabolic spectral regions. Human prostate tissues, as well as gel samples of a metabolite mixture solution, were measured with CW water presaturation on a 14.1T spectrometer, with HRMAS spinning rates of 250, 300, 350, 600 and 700 Hz, and 3.0 kHz. Editing spectra by means of a simple minimum function, Min(A, B, ..., N) for N spectra acquired at different but close spinning rates, produced SSB-free spectra.. Statistically significant linear correlations were observed for metabolite concentrations quantified from the Min(A, B, ..., N)-edited spectra generated at low spinning rates, with concentrations measured from the 3kHz spectra, and also with quantitative pathology. These results indicate the empirical utility of the scheme for intact tissue analysis, which as an adjunct tool, may assist pathology for disease diagnosis.

Key Words: HRMAS, Proton MRS, Human Prostate, Slow Spinning.

Introduction.

The utility of high-resolution magic angle spinning (HRMAS) proton NMR spectroscopy for the analysis of intact biological tissues has been acknowledged increasingly by spectroscopic laboratories in the field of medical MR (1-11). Correlations between tissue metabolites measured with this spectroscopic method and tissue pathologies have been identified, thus demonstrating the potential of the method to supplement the evaluation of histopathology. The most significant asset of this method is that it does not jeopardize the structural integrity of the tissue, and therefore makes it possible to evaluate tissue samples histopathologically, after they have been studied spectroscopically (12). Therefore, the investigation of slow spinning measurements for the optimal protection of tissue histopathological structures from the possible damages of high-rate spinning, has become a research interest, and studies in this area have also evaluated the possibility of conducting HRMAS measurements on objects larger than surgical specimens (13-15).

Magic angle spinning, a line-narrowing technique, has the potential to reduce line broadenings due both to homogeneous and inhomogeneous interactions. Homogeneous line-broadenings, the results of fast spin diffusions (e.g. dipolar couplings) and exchanges, generate the final isotropic line shape, and obscure the identification of contributions from individual spins. Inhomogeneous line-broadenings, in theory, can be traced to individual spins that either are oriented differently with the magnetic field (e.g. chemical shift anisotropy), or are experiencing a different field strength (e.g. magnetic susceptibility). With MAS on protons, homogeneous line-broadenings, particularly from dipolar interactions at natural abundance, are too large in scale to be narrowed with the currently achievable spinning rates. As a result, the proton signals from proteins and cell membranes cannot be detected with a HRMAS measurement, even for instance, at spinning rates of >5 kHz. The enhancements in the tissue measurements observed with HRMAS at a spinning rate of a few hundred Hertz, are the results of the averaging of inhomogeneous interactions, mostly magnetic susceptibility effects, in biological fluids and in cytoplasm. Experimental results have shown that a reduction in spinning rates with HRMAS does not interfere with the ability of HRMAS to reduce spectral line-broadenings due to inhomogeneous interactions (13-16). Furthermore, such reductions in the effects of these inhomogeneous interactions do not happen at a specific, determined spinning rate, but rather happen gradually with the increase of the spinning rate, and are maximized when all the interactions are experimentally accounted for.

Basic physics suggests that the probability of the occurrence of structural damage resulting from the centrifugal stress of spinning greatly decreases as the spinning rate is lowered. Therefore, there seems to be an optimal spinning rate below the maximum rate required for the complete reduction of inhomogeneous interactions. At this optimal point, the spinning rate is fast enough to produce tissue spectral resolution adequate for the identification of metabolites for pathology use, while slow enough to preserve tissue pathology structures. However, to study biological tissues at spinning rates <1 kHz, effective suppression of spinning side-bands (SSBs), particularly those from water signals, is essential in order to eliminate interference with metabolite peaks of interest.

Recently, results of a HRMAS proton NMR study of human prostate tissues obtained under spinning rates of 600 and 700 Hz, with the assistance of a rotor-synchronized DANTE sequence, were reported (16). A robust performance by the technique in terms of the reproducibility of SSB suppression and the simplicity of its concept and execution was observed. With this approach, spectral regions free of water SSBs were selected alternately between the

600 and 700-Hz generated spectra. The effectiveness of this approach for biological systems in which SSBs of metabolites other than water are negligible was demonstrated. However, it was acknowledged that the effectiveness of the approach would diminish for systems in which SSBs either from tissue metabolites or surgical alcohol contamination are present. In addition, the empirical selection of spectral regions, although effective, has elicited concerns regarding the objectivity of the procedure.

In the 1980's, Patt suggested that SSBs in solid state NMR could be removed with a novel mathematical scheme by editing two spectra (A, B), obtained at different spinning rates, with the formula: $(A+B-|A-B|)/2$ (17). However, the suggestion received little attention. Upon reviewing this mathematical scheme, it became apparent that the proposed formula is equal to the function of Min(A, B), the point-by-point minimum of spectra A and B. This recognition also led to a simple and critical extension of the scheme to Min(A, B,..., N). The results obtained from Min(A, B) and/or Min(A, B,..., N) on both gel samples of a metabolite mixture solution, and also human prostate samples, are presented in this report.

Methods.

Tissue Protocol. The NMR analysis of human prostate surgical specimens was approved by the Institutional Review Board (IRB) at the Massachusetts General Hospital. Tissue samples were snap-frozen in liquid nitrogen and stored at –80°C. Thirty-one prostate samples were used in the study. At the completion of the spectroscopic analysis, tissue samples were fixed in 10% formalin, embedded in paraffin, cut into 5-micron sections at 100 micron intervals, and stained with hematoxylin and eosin. Cross-sections of each sample were quantified from pathology slides using an Olympus BX41 Microscope Imaging System (Olympus American, Inc., Melville, NY) equipped with the image analyzer, MicroSuite™ (Soft Imaging System Corp., Lakewood, CO). The percentages of area representing cancer cells, normal epithelial cells and stroma in each cross-section were estimated visually to the nearest 5% by a pathologist who had no knowledge of the spectroscopic results. The reported vol% of each pathological presentation was calculated based on the sizes of the cross-sections and the corresponding area percentages of each pathological feature.

Preparation of a Standard Gel Mixture Solution of Common Metabolites. A mixture gel-solution of 10 commonly observed cellular metabolites was prepared to test the quantitative capability of HRMAS proton NMR spectroscopy and, in particular, the examined spectral editing scheme. The following compounds (approximately one milli-mole of each) were dissolved in 100 ml distilled water: phosphocreatine, L-glutamic acid, sodium citrate, L-glutamine, taurine, myo-Inositol, N-acetylaspartate, phosphorylcholine, glycerophosphorylcholine, and lactic acid. About 1.5 g of agarose was added to the mixture. The pH of the mixture solution was adjusted to ~7.0. The mixture was heated until the agarose dissolved, and then was cooled to form a gel solution. The gel of the mixture solution was kept at 4 °C. The measured concentrations determined from the spectroscopy data were between 6.7 and 26.2 mM based on the tested range of spinning rates.

HRMAS Proton NMR. The NMR experiments were carried out on a Bruker (Bruker BioSpin Corp., Billerica, MA) AVANCE spectrometer, operating at 600 MHz (14.1T). The HRMAS probe had three frequency channels: ^{1}H, ^{13}C (not used in these experiments), and ^{2}H. Samples were placed into a 4 mm zirconia rotor with Kel-F plastic inserts, which created a spherical sample space of ~10 μl located at the center of the detection coil. A small (~0.1 mg), silicone rubber sample was permanently fixed inside one of the Kel-F spacers, positioned within the detection coil but not in contact with the sample, to function as an external standard (STD) for both frequency (0.06 ppm from TMS) and quantification. Different amounts of the gel-solution sample (6-10 mg) were measured. Prostate tissue samples (8-10 mg) were obtained directly from freezers without further preparation. Tissue samples' weights were estimated based on the weight of the empty rotor and the weights of the rotor with the samples, before and after HRMAS measurements. Because of the weight difference between the rotor and the tissue samples (about 1000 times), and the apparent loss of sample weight after HRMAS measurements, (likely due to the water condensation on the outside wall of the rotor, which contained frozen tissue when weighed before HRMAS analysis), the error in weight is estimated generously as 0.5 mg. Approximately 1.0 µl of D_2O was added to each sample for ^2H field locking. The sample was introduced into the probe, which was pre-cooled to 3°C for NMR measurements at that temperature. The rotor spinning rate accuracy (±1.0 Hz) was controlled with an MAS controller and was verified with the positions of the SSBs in the spectra.

Spectra were acquired with the spectrometer frequency set exactly on the water resonance. Two types of spectra were acquired: 1) CW water presaturation, followed by a single 90° excitation pulse, used for both tissue and gel-solution samples, and 2) Rotor-synchronized CPMG, with a total of 20 ms delay after the 90° excitation pulse, used only with gel-solution samples. The CPMG sequence with a very short delay is used to reduce broad resonances caused by probe background. Metabolite concentrations may be estimated from such a CPMG spectrum by reference to the intensity of water signals, while estimations from water presaturated spectra rely on the simultaneous measurement of the external standard.

Ten gel-solution samples of different weights were measured at spinning rates of 600, 700 Hz and 3.0 kHz with both CW water presaturation and rotor-synchronized CPMG pulse sequences. Of these, three were measured at the following additional spinning rates, with only the rotor-synchronized CPMG pulse sequence: 250, 300, 350, 800, 900 Hz, and 1.0, 1.2, 1.4, 1.6, 1.8, 2.0, 2.4, 2.8, and 3.2 kHz. Of note, when total spectral absolute intensities of different spinning rates were compared, a decreasing trend was observed after 2.4 kHz. This reduction was likely the result of the sample leakage from the center of the rotor to the ends, due to spinning rate increase. Hence, data from 2.8 and 3.2 kHz spectra were not included in further calculations. The CW water presaturation sequence was used for human prostate tissue analysis. Of the reported 31 human prostate samples, two samples were measured at spinning rates of 250, 300, 350, 600, 700 Hz, and 3.0 kHz. Fourteen samples were measured at spinning rates of 600, 700 Hz and 3.0 kHz, and 15 samples were measured at spinning rates of 250, 300, and 350 Hz. Of note, the reported 17 samples measured at 250-350 Hz were the only samples analyzed thus far at those spinning rates, while the 16 samples evaluated at 600, 700 Hz and 3.0 kHz were the first samples from a series of studies involving 298 tissue specimens to date measured according to the Min(A, B) scheme.. Each spectrum was acquired with 32 transients and a repetition time of 5s.

Spectroscopic data were processed using the Nuts software (Acorn NMR Inc., Livermore, CA) according to the following procedures. All free induction decays were subjected to 0.5-1 Hz apodization before Fourier transformation, baseline correction, and phase adjustment. Min(A, B, ..., N) was applied to the data in the frequency domain using Nuts software after all individual spectra had been processed. Resonance intensities reported here represent integrals of curve-fittings with Lorentzian-Gaussian line-shapes, normalized by the STD intensity measured for each sample. All intensities reported here in the context of quantification refer to area integrated intensities. Tissue metabolite concentrations were calculated based on the integrated intensity ratios of metabolites over the STD, as explained in detail in the following Results section.

Results.

Evaluation of the Standard Gel Solution, and Calibration of the Silicone Rubber STD in the Sample Rotor. **Figure 1** shows a spectrum of the prepared metabolite gel solution measured at a spinning rate of 3.0 kHz with the CPMG sequence without water presaturation. Particularly, spectrum (a), which is a vertical expansion of the entire spectrum (b), clearly shows resonances of all the prepared metabolites, although the integrated intensity of citrate seems less than its expected concentration. In addition, a prominent $-CH_3$ resonance peak from a piece of silicone rubber STD (~0.1 mg) that was permanently fixed inside the sample rotor was observed. Since the physical nature of the STD is of a solid, its integrated intensity (at ~0 ppm) is heavily dependent upon the spinning rate, as shown in **Figure 2**. The relationship between the spinning rate and the STD absolute spectral integrated intensity has both linear, for the spinning rate region 250Hz to 700Hz, and logarithmic, for spinning rates above 700 Hz, components. Of particular interest to the present work, it was found that the STD's integrated intensity at 3.0 kHz was (3.06 ± 0.23) times higher than that measured at 600 Hz (16).

The overall quantitativeness of HRMAS measurements was tested by varying the sample weights of the metabolite gel-solution. A linear relationship was observed between sample weight and the ratio between the summed spectral integrated intensities of all metabolite peaks and those of the STD, measured at 3.0 kHz with the water presaturation sequence, as seen in **Figure 3**.

The relationship between the sample spinning rate and the measured metabolite integrated intensities in the gel samples, represented both by concentrations (calculated according to the integrated intensity of the water resonance measured from the CPMG sequence) and relative integrated intensities (Rel. Int., obtained as a ratio over the STD integrated intensity measured with the water presaturation sequence at 600 Hz), was examined. An example of this analysis applied to the lactate data (n=3) is shown in **Figure 4**. Both plots in the figure show a very similar logarithmic relationship of statistical significance between increased spinning rate and the evaluated integrated intensities. The apparent integrated intensities (both in concentration and in Rel. Int.) at different spinning rates (e.g. 600 Hz and 3.0 kHz) can be estimated for different metabolites according to these logarithmic curves. The linear relationship between metabolic Rel. Int. and metabolic concentration obtained from five measured metabolites both at 600 Hz and 3.0 kHz, is shown in **Figure 5**. This linear relationship is critical for the use of STD in the estimation of metabolite concentrations in intact tissue from spectra for which water presaturation is applied to improve the detectability of endogenous metabolites.

Measurement of Prostate Tissue at Low Spinning Rates. By varying the sample weight and spinning rate, spectroscopic analysis of standard gels was able to identify the relationships necessary for the quantification of individual metabolites from human prostate tissue spectra edited with the Min(A, B,..., N) mathematical scheme. **Figure 6** presents results from the human prostate tissue sample that had the largest residual water SSBs after presaturation. Spectra A (Fig. 6a) and B (Fig. 6b) were measured at spinning rates of 600 and 700 Hz, respectively, where SSBs from water and the external standard were clearly observed. Figure 6d is a spectrum of the same sample measured at the 3.0 kHz spinning rate, where all of the SSBs were pushed outside the region of interest (4.8 ppm – (-)0.2 ppm). However, (d) was plotted with a different vertical scale to make possible the comparison of the overall metabolite profiles with (c). Visual inspection reveals no difference between (d) and (c), where (c) represents the resulting spectrum after Min(A, B) editing. Additionally, Figure 6e represents the digital inspection of these spectra (c and d); differences between the two spectra, while observable, are minimal and can be neglected without compromising any resulting data. This Min(A, B) editing approach was further applied to three spectra, A, B, and C (**Figure 7**) generated at spinning rates of 250Hz, 300Hz, and 350Hz, respectively. All three spectra showed visible SSBs. However, after applying the Min(A, B, C) editing scheme to the three spectra, all SSBs were eliminated, as seen in Figure 7d.

Tissue metabolite concentrations were estimated based on their ratio integrated intensities over the STD, measured both at low spinning rates (600, 700 Hz) according to Min(A, B), and at 3.0 kHz. The comparison of metabolite concentrations measured with Min(A, B) to those obtained at 3 kHz is shown for the examples of polyamines and citrate in **Figure 8**. Comparisons for other metabolites are presented in **Table 1**. Results in the table are represented by linear regression analyses performed between the two sets of data collected from the 16 samples. These linear regressions were constructed with the 3.0 kHz data on the horizontal, and the Min(A, B) results on the vertical. Hence, if the Min(A, B) value of a particular metabolite is identical to that measured at 3.0 kHz, the slope of the linear regression will be 1 and the intercept will be 0. On the other hand, a slope less than 1 indicates that the integrated intensity of the metabolite measured at 3 kHz has a higher value than that determined with Min(A, B) at 600-700 Hz. For almost all of the evaluated metabolites, higher apparent concentrations were observed under the 3.0 kHz measurement conditions. This was not surprising because it is widely acknowledged that an increase in spinning rate can potentially increase the observable amount of a metabolite, effected by the greater minimization of bulk magnetic susceptibility effects and other physical, environmental effects, such as viscosity.

Two samples, measured at 250, 300, 350, 600, 700 Hz, and 3.0 kHz, demonstrated linear relationships both between the metabolic Rel. Int. at 600-700Hz and at 3kHz, and also between the metabolic Rel. Int. at 250-350Hz and at 3kHz obtained with 16 quantified metabolite resonances (32 data points) from the Min(A, B, ...,N)-edited spectra. Interestingly, while the Rel. Int. at 600-700Hz in **Figure 9** show a similar overall slope value (0.58) to those seen in Table 1 (avg. 0.79) for concentrations, the Rel. Int. at 250-350Hz indicates a slope of 0.31, suggesting that the apparent metabolic Rel. Int. measured at 250-350 Hz was much smaller than that measured at 3.0 kHz. Of note, the STD integrated intensities used in the figure were calibrated according to the STD-spinning rate relation curve presented in Figure 2.

Correlation of Prostate Metabolite Integrated Intensities, Measured at Low Spinning Rates, with Prostate Pathology. The utility of prostate metabolite data obtained with the Min(A, B, C) editing scheme at spinning rates 250, 300, and 350 Hz was evaluated by testing the data's correlation with the volume percent of tissue pathological structures. Statistically significant linear correlations between normal epithelium (Vol %) and polyamines and citrate are shown in **Figure 10.** These are in close agreement with previously reported results obtained at 9.4T (400 MHz) field strength, under a spinning rate of 2.5 kHz (*12*).

Discussion.

The goal of this work is to establish a simple, reproducible, and empirical spectroscopic scheme that can effectively evaluate intact tissue metabolite concentrations measured at slow spinning, which is desirable for the protection of tissue pathological structures from the damages of fast mechanical spinning, and the application of spinning to larger objects. This aim was conceived because of the need for tissue pathological evaluation after HRMAS analysis in order to gauge the potential of the metabolite measurements to aid disease diagnosis. As an empirical approach, the mathematic validity of the scheme from the precise concepts of NMR physics is beyond the scope of the current report.

Restrictions on Min (A, B,..., N). The principle of Min(A, B,..., N) will only work if the following experimental conditions are met: 1) the spectra (A, B,...,N) are obtained from the same sample under the same experimental conditions, other than spinning rate; 2) the line-width for an individual resonance is the same (within measurement error) in all spectra, i.e. there is no additional visible narrowing of either homogeneous or inhomogeneous broadenings at higher spinning rates; for instance, in this study, the line width at half maximum (LWHM) for creatine at 3.03 ppm in intact tissue was measured to be 3.73 ± 0.98 Hz at 600 Hz spinning, and 3.83 ± 0.95 Hz at 700 Hz spinning; 3) the spinning rates are decided such that there is no SSB overlap point present in the regions-of-interest in all N spectra; and 4) there are no negative resonances in the spectra. Therefore, the spectra should be identical when measured within a reasonable range of spinning rates (e.g. 600 and 700 Hz) if the integrated intensities of SSBs from metabolites can be neglected when compared with the isotropic resonance integrated intensity. The contributions of SSBs from any source (water, external standard, any metabolites, or even contamination) will result in the increase of local spectral integrated intensity.

Min(A, B,..., N) versus DANTE. Compared with the previously reported DANTE method that was optimized mainly for the elimination of SSBs from water and the external standard (STD), the Min(A, B,..., N) editing procedure can produce more accurate results than the DANTE approach for cases in which not only SSBs of water and/or STD, but also SSBs of either tissue metabolites or other contaminants are of concern as well (16). However, the DANTE approach still may be proven as a method of choice in the future application of HRMAS spectroscopy in clinic, where a defined metabolic marker(s) can be quantified with the measurement of one spectrum of an appropriately selected spinning rate. The advantages of the two-spectra Min(A, B) method are apparent, particularly during the research phases of surveying and discovering the marker(s). In addition, the Min(A, B) method can easily be extended to a general scheme of Min(A, B,..., N), as was demonstrated in this study using spinning rates of 250, 300, and 350 Hz. Future studies using this method may provide evidence for optimal spinning rates, where tissue degradation is minimized and metabolic integrated intensity maximized.

Quantitative evaluations of the relative metabolite integrated intensities (i.e. [metabolite]/[STD]) between the current analyses and those presented in the previous report of DANTE-CPMG measurements (16) have revealed that the previous method might result in the reduction of metabolite integrated intensities by approximately 43% compared with the current Min(A, B) measurements of a single excitation pulse without CPMG. The reductions were likely the result of T_2 losses due to the rotor-synchronized CPMG of 10 ms.

Metabolite Integrated Intensities. The data presented in Table 1 were collected from the linear regression analysis of metabolite integrated intensities measured at spinning rates of 600-700 Hz with Min(A, B) vs. those obtained at the 3.0 kHz spinning rate. Since the metabolite integrated intensities of both the high and low spinning rates were normalized by the STD integrated intensity from direct measurement or projection, respectively, these integrated intensities represented the concentrations of the measured metabolites. Hence, a slope of less than 1.0 indicates that the measured spectral integrated intensity at the higher (3.0 kHz) spinning rate was greater than that obtained at the lower (600-700 Hz) spinning rates. In general, it may be expected that the further the slope shrinks from 1.0, the more inhomogeneous the interactions experienced by the metabolite, for instance, as in viscosity-related limitation on molecular mobility. For instance, a recent study of human prostate indicates that polyamines are secreted in prostatic secretory granules of approximately 1 μm, a degree of spatial constriction which would result in the minimization of metabolite movements (18). If this is true, we may expect that the values of metabolic slopes vary with different tissue types. Study in this direction may have the potential to assist the understanding of the physical nature of these endogenous cellular metabolites; however, this is beyond the scope of the current evaluation. Nevertheless, this difference in the measured metabolite integrated intensities at different spinning rates is expected, and should not affect the accuracy of the application of the HRMAS method for disease diagnosis, as long as the metabolite data are acquired at the same spinning rate.

Correlation of Metabolite Integrated Intensity to Tissue Pathologies. Since the Min(A, B, ..., N) editing approach minimizes tissue degradation caused by high spinning rates, the same tissue samples can undergo pathological assessment, thereby, allowing for the study of any correlations between individual metabolite Rel. Int. and vol% of a specific tissue component, such as glandular epithelium or cancer cells. Expanding on this concept, the use of more detailed pathological assessments than vol% of a tissue component, such as immunohistochemical stainings, for comparison with metabolite integrated intensities may aid in disease diagnosis and patient prognosis.

Nonlinearity of Min(A, B,..., N) and Fitting of Min(A, B,..., N) Spectra with Lorentzian-Gaussian Functions. Careful consideration must be given to the nonlinear nature of the minimum function, Min(A, B,..., N), as it relates to measurement accuracy and statistical treatment of metabolite concentration. The validity of the Min(A, B,..., N) function relies heavily on the assumption that the component spectra differ only in the SSBs frequencies. It is easy to conceptualize that various instrument errors (e.g., baseline or phasing errors) and spectroscopic effects (e.g., changes in peak amplitude or line-width associated with MAS rate changes) may, after processing with Min(A, B,..., N), introduce errors in spectral integrated intensities, leading to errors in metabolite concentration estimates. Furthermore, the Min(A, B,..., N) function is not appropriate for processing spectra with negative peaks, unless additional nonlinear treatment (e.g., taking absolute value spectra) is executed.

The effects of the nonlinearity of Min(A, B,..., N) on spectral noise deserve special attention. In the presence of noise, spectra run at different spinning rates but which otherwise are identical will differ on a point-by-point basis. As Min(A, B,..., N) selects the lowest point, it introduces a negative bias which is uniform across the spectrum. If uncorrected, this will result in a negative bias in the metabolite measurement, with a magnitude that depends on the width and shape of the metabolite peak. The nonlinearity of the minimum function changes the noise statistics as well. A spectrum with normal (Gaussian) background noise, processed with Min(A, B,..., N), yields a spectrum with a non-Gaussian noise distribution, making statistical analysis more difficult, but not impossible(given certain treatments of numerical methods). However, these theoretical concerns may not impair the empirical utility of the scheme in biological tissue analysis. **Figure 11** illustrates that while there is some difference between the resulting Min(A, B,..., N) spectra (a region of Figure 7d) obtained from a sample (Fig. 11a), and that obtained through curve fitting(Fig. 11b) of the spectra, it is minimal and typical of any curve fitting process (Fig. 11c). Thus, the production of spectra with non-Gaussian noise distribution resulting from the application of Min(A, B,..., N) should not remarkably affect metabolite integrated intensities. Therefore, since the interests and the purpose of this report are focused on the application of this empirical spectroscopic method in medical pathology, any further discussion of the nonlinearity of Min(A, B,..., N) and its correction may exceed the intended scope of the paper.

Conclusions.

The reported results indicate that by editing two or three slow spinning tissue HRMAS spectra with a simple mathematical function Min(A, B, ..., N), the spinning sidebands can be eliminated to produce a SSB-free tissue NMR spectrum that may be sensitive enough for the purpose of disease diagnosis. Tests of the proposed scheme on both a standard gel solution of commonly observed tissue metabolites and intact human prostate tissue samples have revealed the empirical usefulness of the scheme. Results further suggest that metabolite integrated intensities thus observed can be correlated to quantitative histopathological data obtained from the same tissue after NMR measurement.

Acknowledgments.

This work is supported by PHS/NIH grants: CA77727, CA80901, CA095624 and EB002026, and in part by a DOD grant W81XWH-04-1-0190.

References:

1. Coen M, Lenz EM, Nicholson JK, Wilson ID, Pognan F, Lindon JC. An integrated metabonomic investigation of acetaminophen toxicity in the mouse using NMR spectroscopy. Chem Res Toxicol 2003;16(3):295-303.
2. Huster D, Schiller J, Arnold K. Comparison of collagen dynamics in articular cartilage and isolated fibrils by solid-state NMR spectroscopy. Magn Reson Med 2002;48(4):624-632.
3. Kurhanewicz J, Swanson MG, Nelson SJ, Vigneron DB. Combined magnetic resonance imaging and spectroscopic imaging approach to molecular imaging of prostate cancer. J Magn Reson Imaging 2002;16(4):451-463.
4. Sitter B, Sonnewald U, Spraul M, Fjosne HE, Gribbestad IS. High-resolution magic angle spinning MRS of breast cancer tissue. NMR Biomed 2002;15(5):327-337.
5. Waters NJ, Holmes E, Waterfield CJ, Farrant RD, Nicholson JK. NMR and pattern recognition studies on liver extracts and intact livers from rats treated with alpha-naphthylisothiocyanate. Biochem Pharmacol 2002;64(1):67-77.
6. Tzika AA, Cheng LL, Goumnerova L, Madsen JR, Zurakowski D, Astrakas LG, Zarifi MK, Scott RM, Anthony DC, Gonzalez RG, Black PM. Biochemical characterization of pediatric brain tumors by using in vivo and ex vivo magnetic resonance spectroscopy. J Neurosurg 2002;96(6):1023-1031.
7. Morvan D, Demidem A, Papon J, De Latour M, Madelmont JC. Melanoma tumors acquire a new phospholipid metabolism phenotype under cystemustine as revealed by high-resolution magic angle spinning proton nuclear magnetic resonance spectroscopy of intact tumor samples. Cancer Res 2002;62(6):1890-1897.

8. Chen JH, Enloe BM, Fletcher CD, Cory DG, Singer S. Biochemical analysis using high-resolution magic angle spinning NMR spectroscopy distinguishes lipoma-like well-differentiated liposarcoma from normal fat. J Am Chem Soc 2001;123(37):9200-9201.

9. Griffin JL, Walker L, Shore RF, Nicholson JK. High-resolution magic angle spinning 1H-NMR spectroscopy studies on the renal biochemistry in the bank vole (Clethrionomys glareolus) and the effects of arsenic (As3+) toxicity. Xenobiotica 2001;31(6):377-385.

10. Schiller J, Naji L, Huster D, Kaufmann J, Arnold K. 1H and 13C HR-MAS NMR investigations on native and enzymatically digested bovine nasal cartilage. Magma 2001;13(1):19-27.

11. Barton SJ, Howe FA, Tomlins AM, Cudlip SA, Nicholson JK, Bell BA, Griffiths JR. Comparison of in vivo 1H MRS of human brain tumours with 1H HR-MAS spectroscopy of intact biopsy samples in vitro. Magma 1999;8(2):121-128.

12. Cheng LL, Wu C, Smith MR, Gonzalez RG. Non-destructive quantitation of spermine in human prostate tissue samples using HRMAS 1H NMR spectroscopy at 9.4 T. FEBS Lett 2001;494(1-2):112-116.

13. Wind RA, Hu JZ, Rommereim DN. High-resolution (1)H NMR spectroscopy in organs and tissues using slow magic angle spinning. Magn Reson Med 2001;46(2):213-218.

14. Hu JZ, Rommereim DN, Wind RA. High-resolution 1H NMR spectroscopy in rat liver using magic angle turning at a 1 Hz spinning rate. Magn Reson Med 2002;47(5):829-836.

15. Hu JZ, Wind RA. Sensitivity-enhanced phase-corrected ultra-slow magic angle turning using multiple-echo data acquisition. J Magn Reson 2003;163(1):149-162.

16. Taylor JL, Wu CL, Cory D, Gonzalez RG, Bielecki A, Cheng LL. High-resolution magic angle spinning proton NMR analysis of human prostate tissue with slow spinning rates. Magn Reson Med 2003;50(3):627-632.

17. Patt S. Personal Communication.

18. Cohen RJ, Fujiwara K, Holland JW, McNeal JE. Polyamines in prostatic epithelial cells and adenocarcinoma; the effects of androgen blockade. Prostate 2001;49(4):278-284.

Table 1. Comparison of linear regressions (slow rates – vertical, vs. 3.0 kHz rate – horizontal) for selected metabolites[a].

Met. Reson. (ppm)	**P value**	**R^2**	**Slope**[b]		**Intercept**	
			Mean	SE	Mean	SE
Lac(4.10-4.14)	<0.0001	0.89	0.91	0.08	-0.24	0.17
mI(4.06)	<0.0001	0.77	1.00	0.14	**-0.18**[c]	**0.18**
3.60-3.63	<0.0001	0.70	0.79	0.13	**-0.07**	**0.34**
3.52-3.54	<0.0001	0.84	0.87	0.10	**-0.09**	**0.32**
Tau(3.41-3.43)	<0.0001	0.80	0.87	0.11	**-0.08**	**0.11**
sI(3.34)	<0.0001	0.84	0.73	0.08	**0.00**	**0.01**
Pch(3.22)	0.0002	0.59	0.83	0.18	**-0.03**	**0.04**
Chol(3.20)	<0.0001	0.81	0.65	0.08	**0.01**	**0.02**
PM(3.09-3.14)	<0.0001	0.66	0.53	0.10	**0.03**	**0.05**
Cr(3.03)	<0.0001	0.87	0.76	0.08	**0.02**	**0.03**
Cit(2.52-2.71)	<0.0001	0.91	0.93	0.08	-0.25	0.12
Glu(2.33-2.36)	<0.0001	0.80	0.86	0.11	**-0.02**	**0.04**
Ala(1.47-1.49)	<0.0001	0.77	0.44	0.06	0.04	0.02
Lac(1.32-1.34)	<0.0001	0.76	0.91	0.13	-0.47	0.32

[a] The comparisons were made based on the estimated metabolite concentrations.

[b] Statistically significant linear correlations with slopes deviating from unity are observed indicating that the 3.0 kHz spinning rate produces higher metabolite integrated intensities.

[c] Bold faced data in the table indicate the intercepts are indifferent from 0.

Figure Legends:

Figure 1. Proton HRMAS spectrum of the prepared standard gel solution of commonly observed tissue cellular metabolites (as labeled) at 3.0 kHz. The spectrum was measured with a rotor-synchronized CPMG sequence with a total delay time of 20 ms. Spectrum (a) represents a 360 times vertical expansion of the fully relaxed spectrum (b).

Figure 2. The center band peak area integrated intensity of a silicon rubber standard (STD) as a function of the rotor spinning rate. The STD (~0.1 mg) was permanently fixed inside one of the Kel-F spacers to function as an external standard for both frequency, and also metabolite quantification. It appears that the spinning rate and the STD integrated intensity follows a linear relationship in the spinning rate region of 250Hz to 700Hz, and then changes to logarithmic for spinning rates above 700 Hz.

Figure 3. The observed linear correlation between the sample weight (the mathematical average before and after spinning) and the total proton spectral integrated intensity measured between -0.2 to 4.8 ppm (excluding water signals) under the HRMAS spinning rate of 3.0 kHz from the prepared standard gel solution of metabolites measured with water presaturation.

Figure 4. Comparisons between the measured metabolite (lactate, n=3) integrated intensities in absolute concentrations and in relative intensities. (a) Absolute concentrations, measured from the CPMG sequence and according to the water resonance intensity; and (b) relative intensity measured from the water presaturation sequence and according to STD integrated intensity measured at 600 Hz) from the standard gel solution as functions of the HRMAS spinning rate.

Figure 5. Linear correlations observed between the relative metabolic integrated intensities as ratios over STD and the metabolite concentration estimated from the observed integrated intensities of water signals. These linear correlations were calculated based on the statistically

significant curve fitting results from the five measured metabolites as exemplified in Figure 4 for lactate.

Figure 6. Human prostate CW water presaturated spectra at spinning rates of (a) 600 Hz (A), and (b) 700 Hz (B). (c) is a spectrum that was edited, using (A) and (B), with Min(A, B) to be visually compared with (d), a spectrum obtained at a spinning rate of 3.0 kHz, plotted with a different vertical scale in order to produce (e), a digital analysis presents the differences between spectra (d) and (c). "*"is used to denote SSBs from tissue water and rubber standard signals.

Figure 7. Human prostate CW water presaturated spectra at spinning rates of (a) 250 Hz (A), (b) 300 Hz (B), and (c) 350 Hz (C). (d) is the resulting spectrum after the Min(A, B, C) editing scheme was applied to (A), (B), and (C). "*"is used to denote SSBs from tissue water and rubber standard signals.

Figure 8. Comparisons between concentrations of prostate metabolites, polyamines and citrate, measured with sample spinning at 3.0 kHz and those measured at 600 and 700 Hz and determined by Min(A, B) editing. If the Min(A, B) value of a particular metabolite is identical to that measured at 3.0 kHz, the slope of the linear regression would be 1 and the intercept would be 0. A slope of less than 1.0 indicates that the measured spectral integrated intensity at a higher (3.0 kHz) spinning rate is greater than that obtained at slower (600-700 Hz) spinning rates. It may be true that the more the slope falls below a value of 1.0, the more "solid-like" the physical state of the metabolite.

Figure 9. Linear correlations between relative metabolic integrated intensities determined at a HRMAS spinning rate of 3.0 kHz and those measured at slower spinning rates (as ratios over the

STD calibrated according to Figure 2); i.e. Min(A, B) measured at 600 and 700 Hz, and Min(A, B, C) at 250, 300 and 350 Hz, for 16 metabolites from two cases.

Figure 10. Linear correlations between relative metabolic integrated intensities of polyamines and citrate with the volume percentage of tissue epithelium measured from the same tissue samples after NMR measurements.

Figure 11. Example of Lorentzian-Gaussian curve-fitting results for a Min(A, B,..., N)-edited spectrum. (a) the 3.31-3.18 ppm spectral region from Figure 7d. (b) the Lorentzian-Gaussian curve-fitting results of (a). (c) spectrum representing the difference between (a) and (b). These differences are minimal and are typically observed with any curve fitting process.

Figure 1.

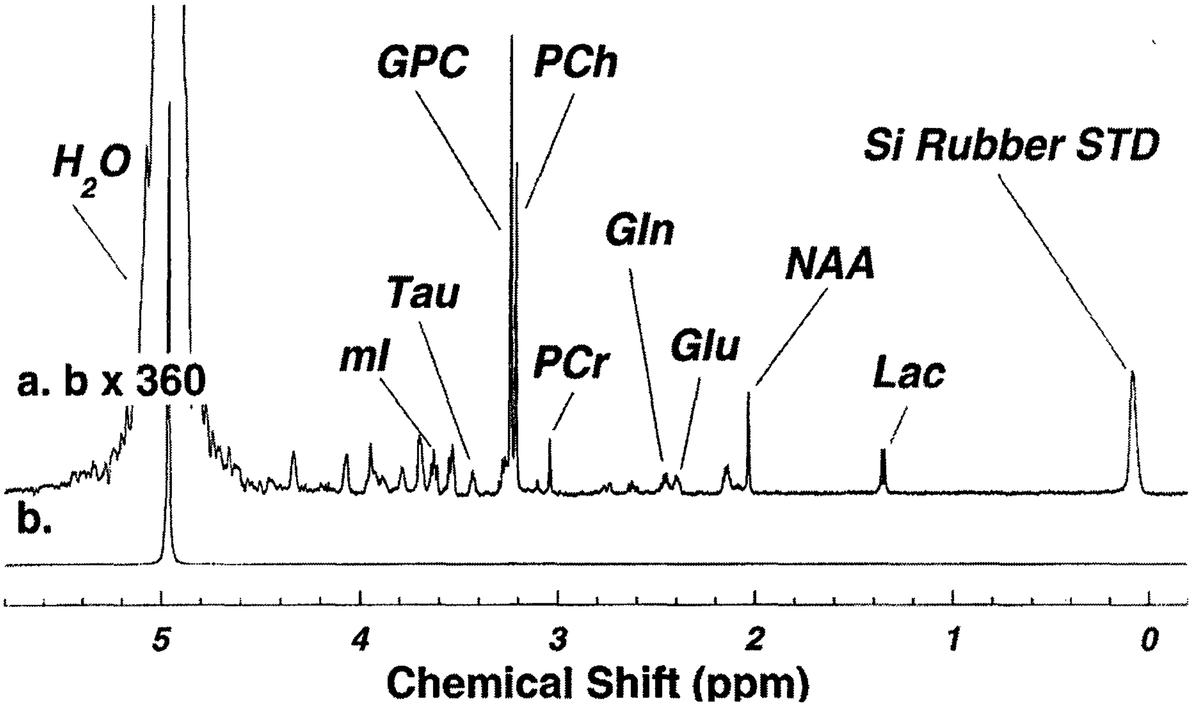
H2O
GPC
PCh
Si Rubber STD
Gln
NAA
Tau
Glu
mI
PCr
Lac
a. b x 360
b.
5
4
3
2
1
0
Chemical Shift (ppm)

Figure 2.

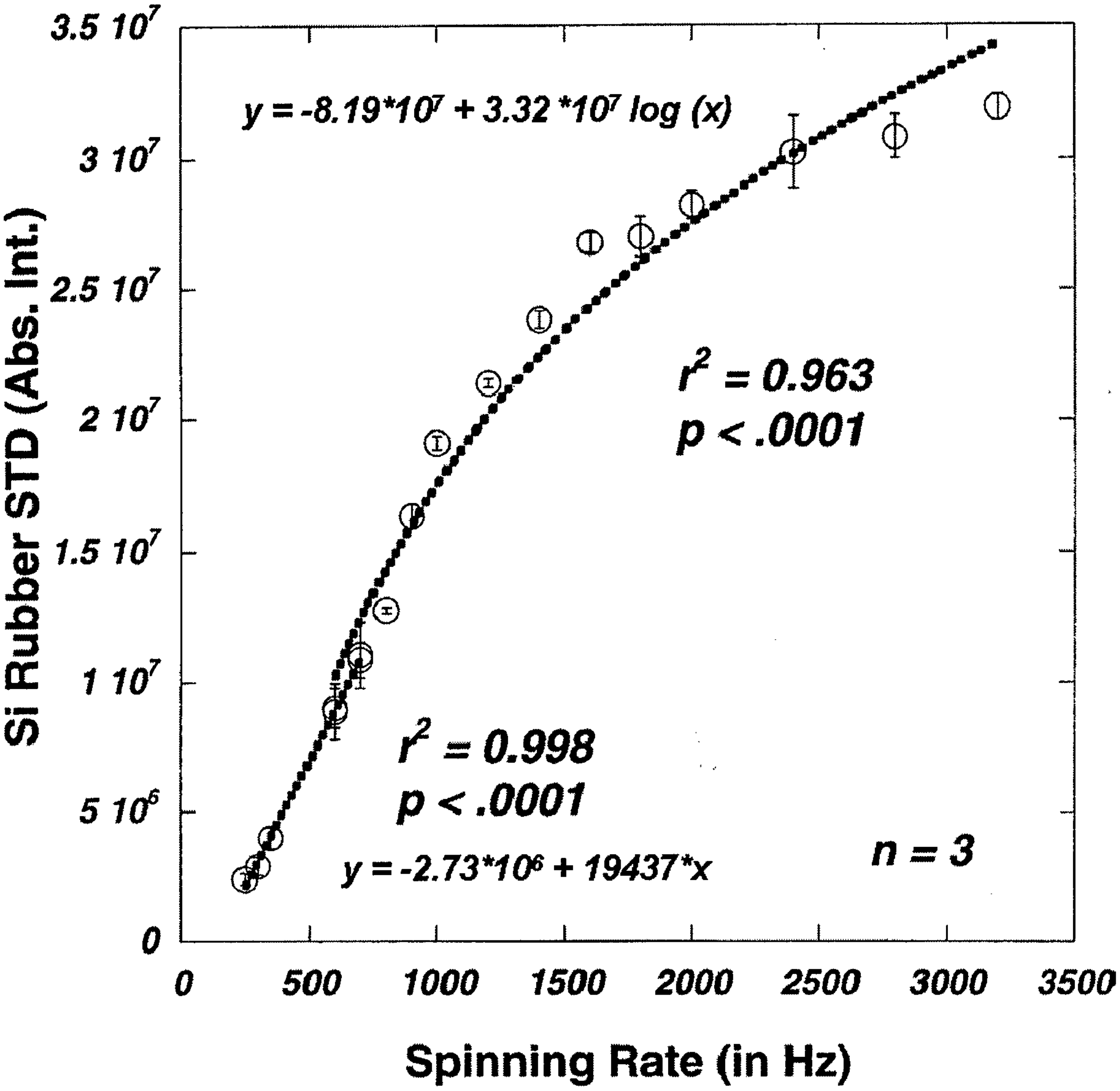

y = -8.19*10^7 + 3.32 *10^7 log (x)
r^2 = 0.963
p < .0001
r^2 = 0.998
p < .0001
y = -2.73*10^6 + 19437*x
n = 3
3.5 10^7
3 10^7
2.5 10^7
2 10^7
1.5 10^7
1 10^7
5 10^6
0
0
500
1000
1500
2000
2500
3000
3500
Si Rubber STD (Abs. Int.)
Spinning Rate (in Hz)

Figure 3.

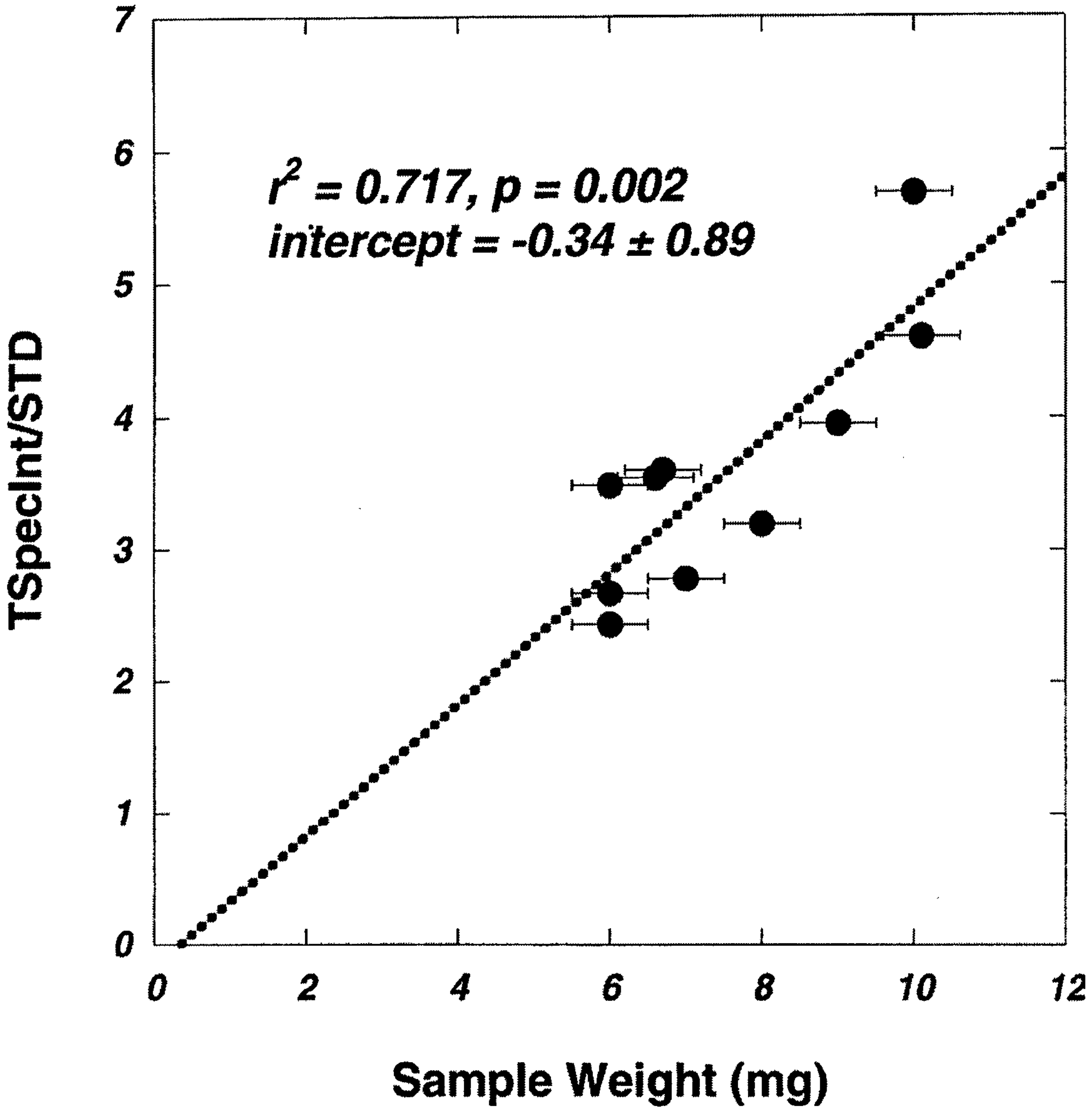

$r^2 = 0.717$, $p = 0.002$
intercept = -0.34 ± 0.89
TSpecInt/STD
Sample Weight (mg)
0
1
2
3
4
5
6
7
0
2
4
6
8
10
12

Figure 4.

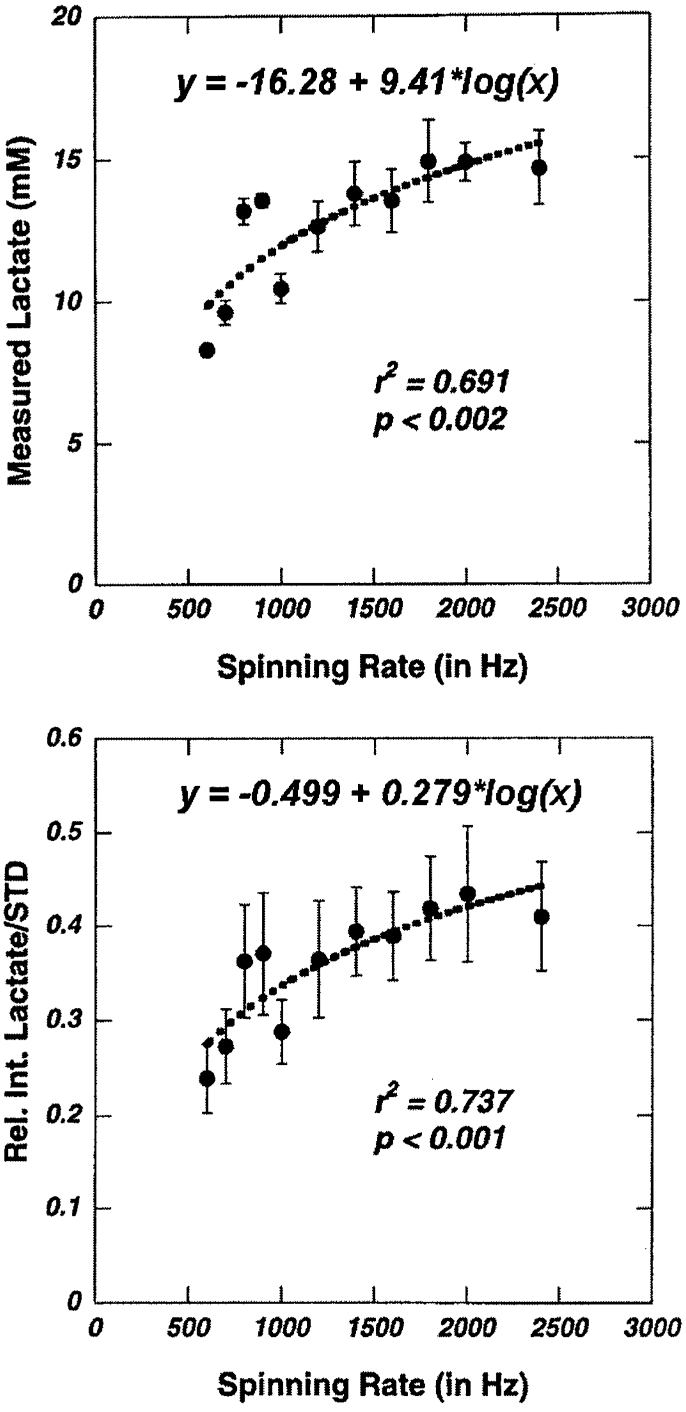
y = -16.28 + 9.41*log(x)
r² = 0.691
p < 0.002
Measured Lactate (mM)
0
5
10
15
20
0
500
1000
1500
2000
2500
3000
Spinning Rate (in Hz)
y = -0.499 + 0.279*log(x)
r² = 0.737
p < 0.001
Rel. Int. Lactate/STD
0
0.1
0.2
0.3
0.4
0.5
0.6
0
500
1000
1500
2000
2500
3000
Spinning Rate (in Hz)

Figure 5.

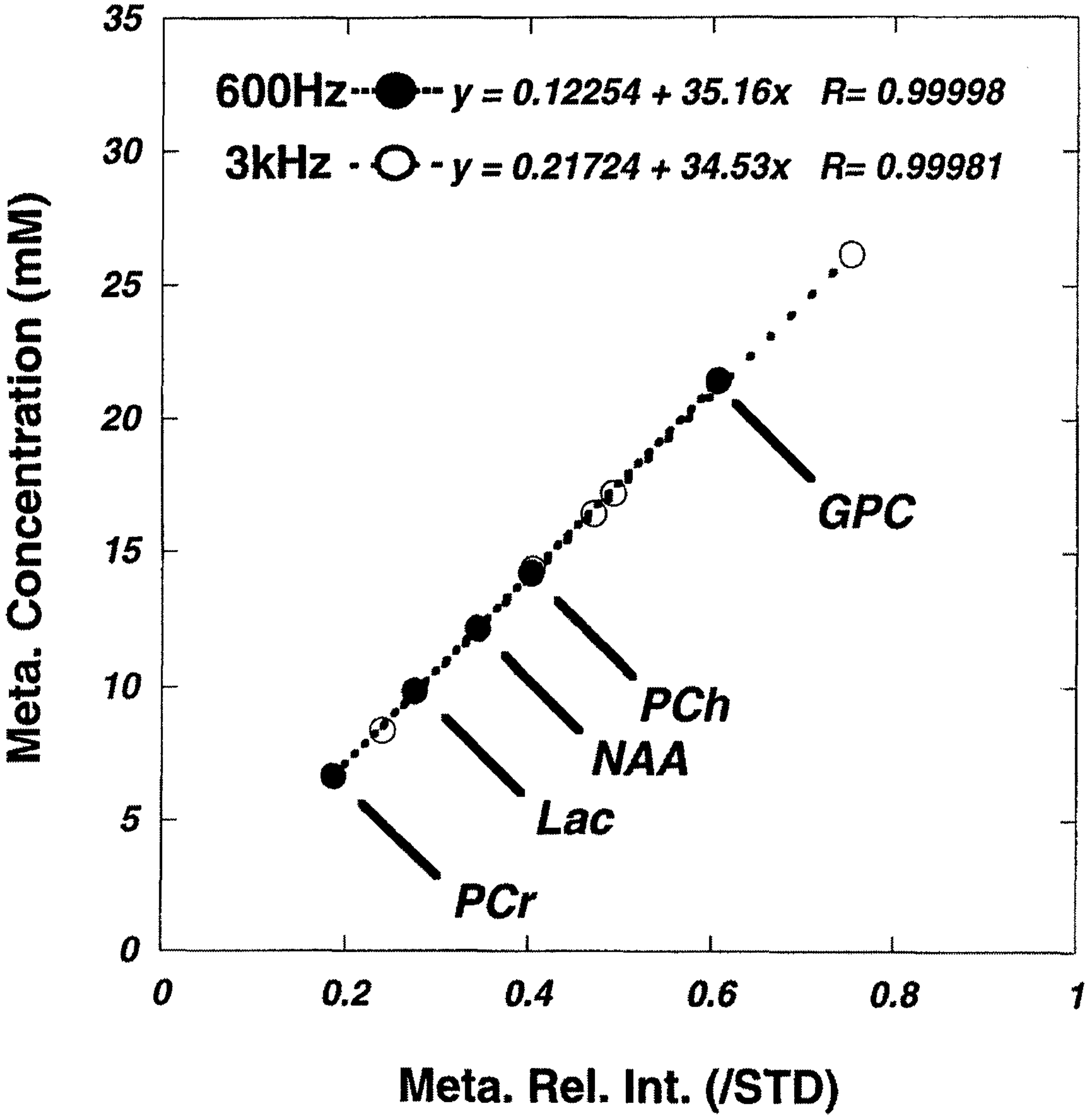
600Hz ● y = 0.12254 + 35.16x R= 0.99998
3kHz ○ y = 0.21724 + 34.53x R= 0.99981
GPC
PCh
NAA
Lac
PCr
Meta. Concentration (mM)
35
30
25
20
15
10
5
0
0
0.2
0.4
0.6
0.8
1
Meta. Rel. Int. (/STD)

Figure 6.

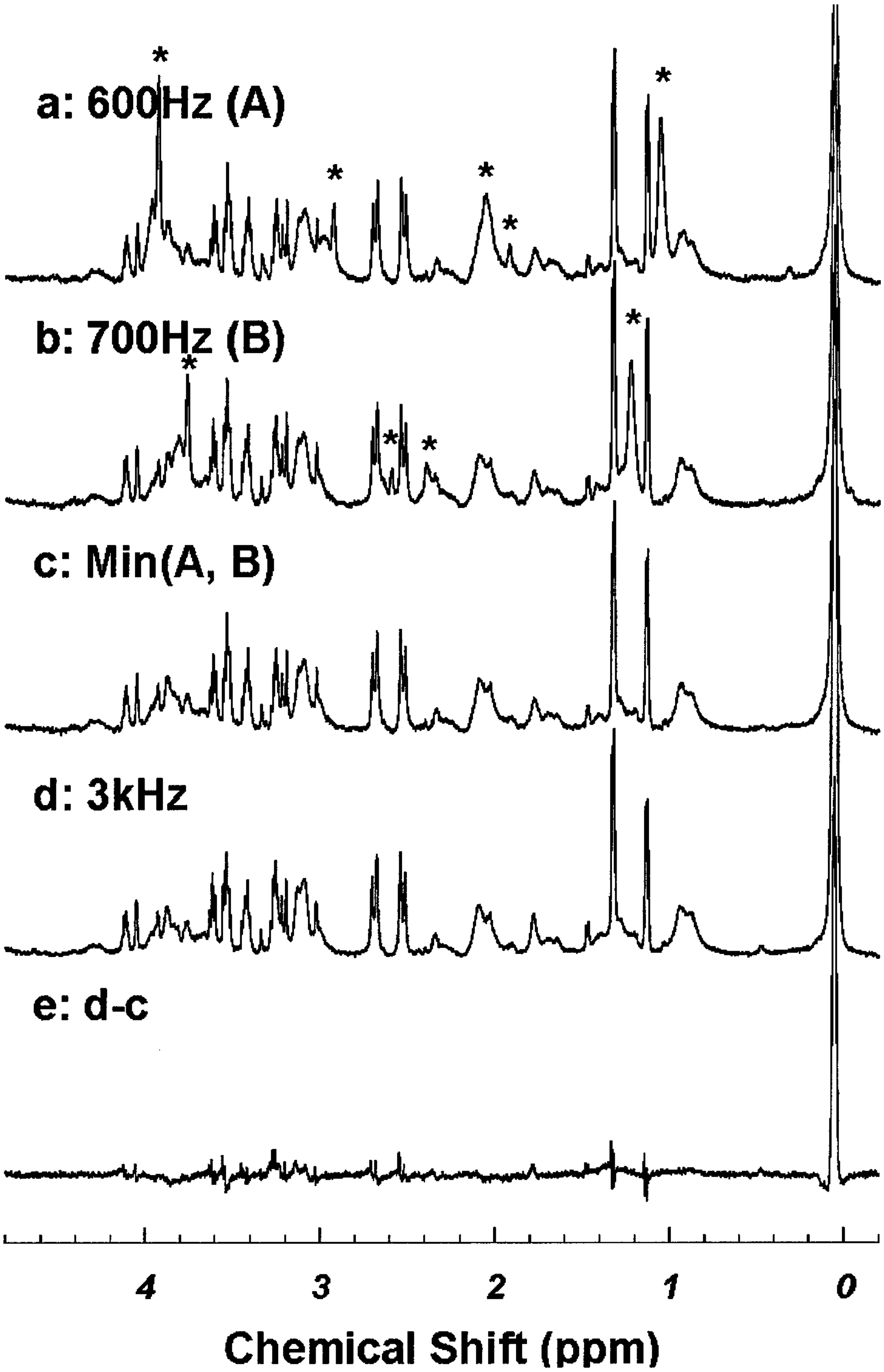

Figure 7.

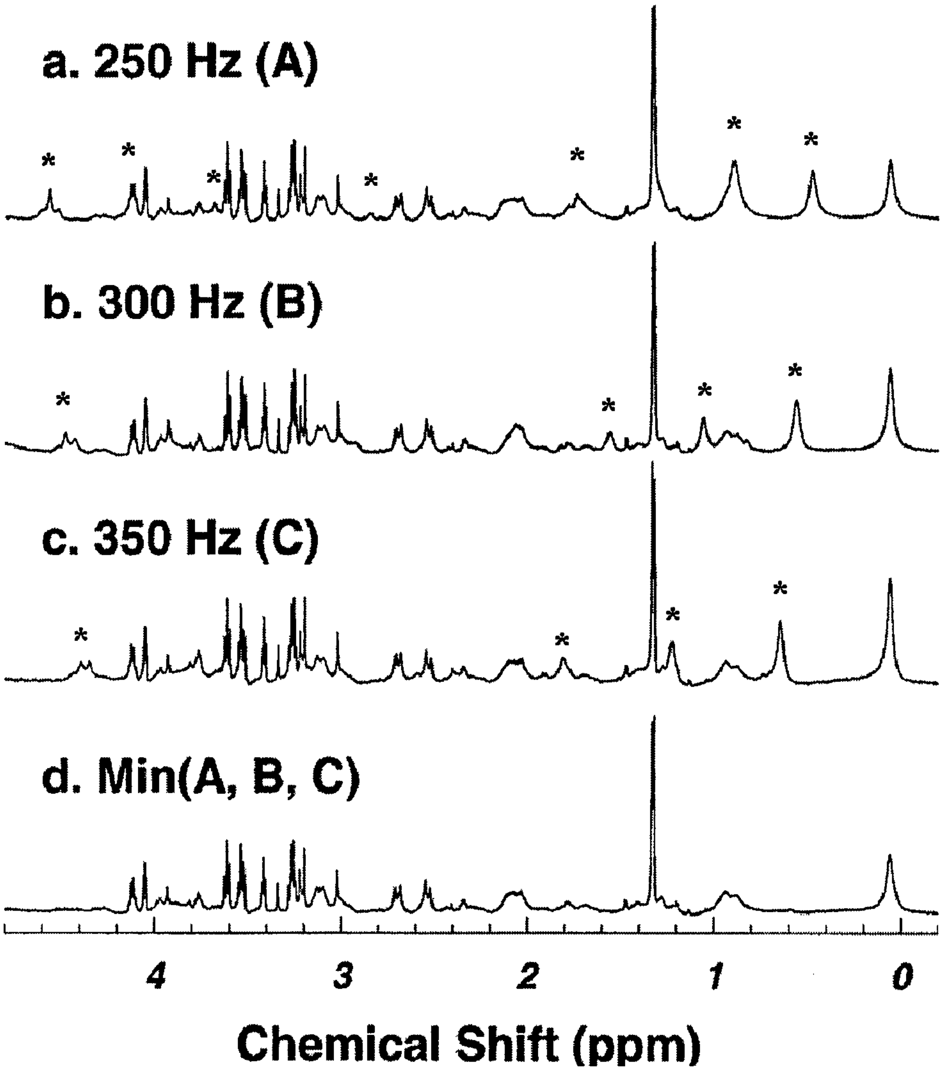

Figure 8.

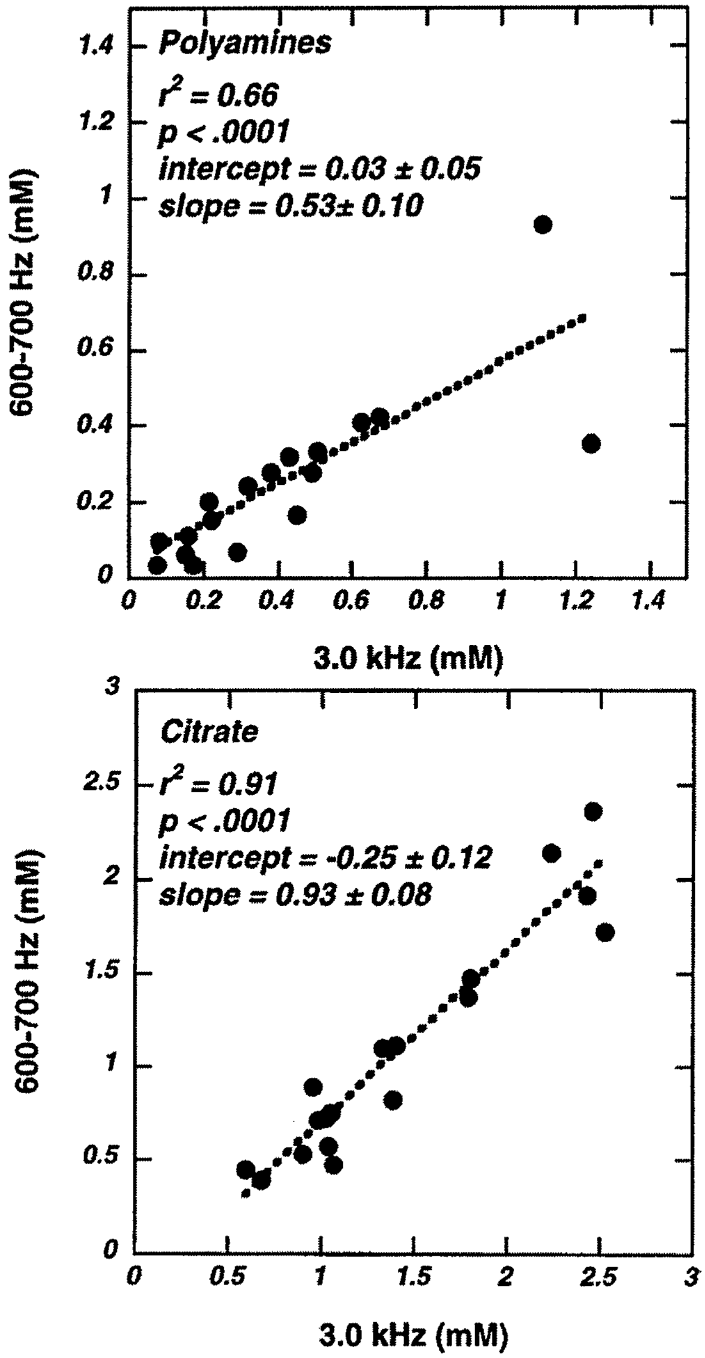
Polyamines
$r^2 = 0.66$
$p < .0001$
intercept = 0.03 ± 0.05
slope = 0.53± 0.10
600-700 Hz (mM)
1.4
1.2
1
0.8
0.6
0.4
0.2
0
0
0.2
0.4
0.6
0.8
1
1.2
1.4
3.0 kHz (mM)
Citrate
$r^2 = 0.91$
$p < .0001$
intercept = -0.25 ± 0.12
slope = 0.93 ± 0.08
600-700 Hz (mM)
3
2.5
2
1.5
1
0.5
0
0
0.5
1
1.5
2
2.5
3
3.0 kHz (mM)

Figure 9.

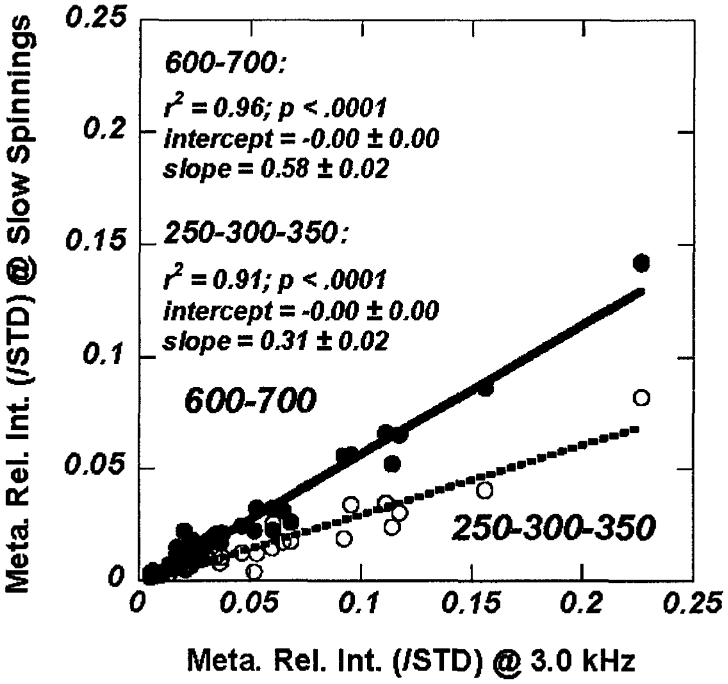
600-700:
$r^2 = 0.96$; $p < .0001$
intercept = -0.00 ± 0.00
slope = 0.58 ± 0.02
250-300-350:
$r^2 = 0.91$; $p < .0001$
intercept = -0.00 ± 0.00
slope = 0.31 ± 0.02
600-700
250-300-350
0
0.05
0.1
0.15
0.2
0.25
Meta. Rel. Int. (/STD) @ Slow Spinnings
Meta. Rel. Int. (/STD) @ 3.0 kHz

Figure 10.

C 3

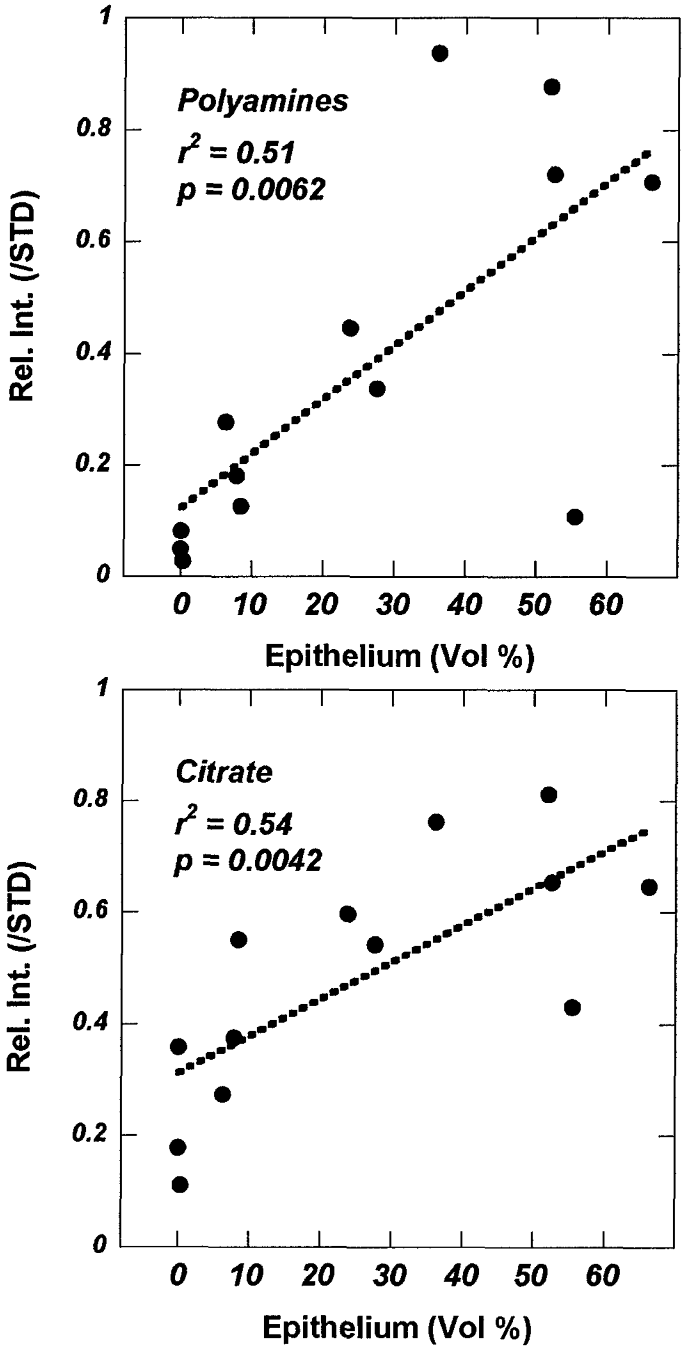
Polyamines
r² = 0.51
p = 0.0062
Rel. Int. (/STD)
0
0.2
0.4
0.6
0.8
1
0
10
20
30
40
50
60
Epithelium (Vol %)
Citrate
r² = 0.54
p = 0.0042
Rel. Int. (/STD)
0
0.2
0.4
0.6
0.8
1
0
10
20
30
40
50
60
Epithelium (Vol %)

Figure 11.

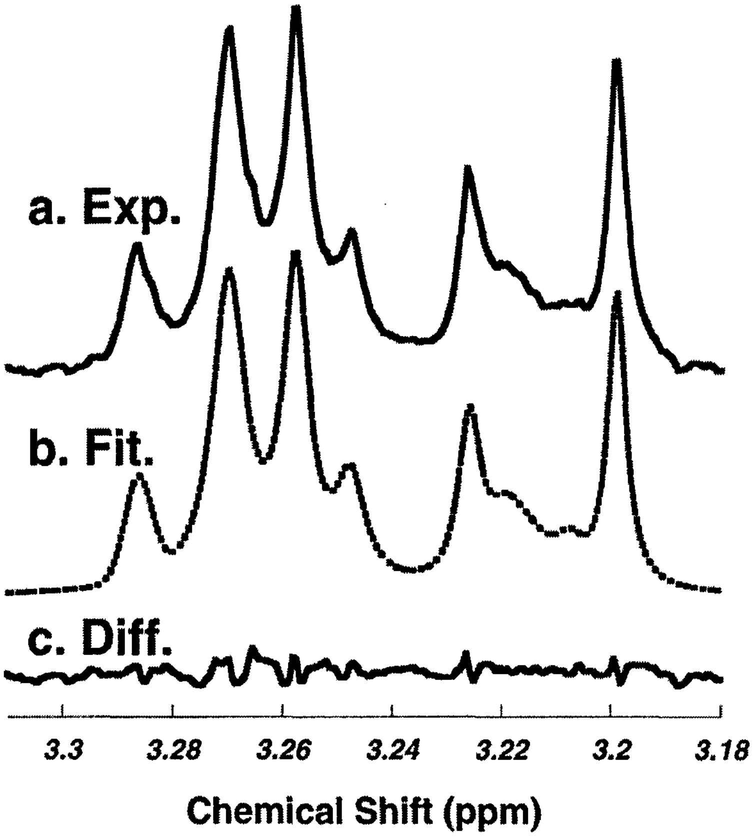

From:	cancerres@aacr.org
Sent:	Thursday, February 03, 2005 11:15 AM
To:	cheng@nmr.mgh.harvard.edu
Subject:	Cancer Research: Decision Rendered on Manuscript CAN-04-4106 Version 2

RE: CAN-04-4106 Version 2
Metabolic Characterization of Human Prostate Cancer with Tissue Magnetic Resonance Spectroscopy

Dear Dr. Cheng:

Your above-referenced revised manuscript has been found to be potentially acceptable for publication in Cancer Research, pending further satisfactory revision of the paper in accordance with the enclosed reviewer's comments. In addition to revising the manuscript as requested, the Editors ask that you shorten your presentation where possible to make it more concise for readers.

Manuscripts that have been accepted in principle must be revised and returned to the journal office within 4 weeks. Please note that a decision as to whether or not the revised manuscript requires further review will be made at the discretion of the Senior Editor. Please see the instructions appended below for information on preparing and resubmitting your revised manuscript.

We appreciate the opportunity to review your work, and we look forward to receiving your revised manuscript.

Sincerely yours,

Frank J. Rauscher, III, Ph.D.
Editor-in-Chief

INSTRUCTIONS FOR RESUBMISSION:
- Prior to resubmitting the manuscript, please consult the journal's Instructions for Authors at http://cancerres.aacrjournals.org/misc/ifora.shtml to ensure that the paper is written and formatted in accordance with the journal's policies.

- After carefully reviewing the Instructions for Authors, please submit the source files (programs in which the documents were created; not a PDF) of the electronic version of your revised manuscript at http://www.rapidreview.com/AACR2/author.html. Please note that electronic figures (both online and on disk) must be at least 300-dpi TIFF or EPS files in CMYK color format. RGB color format will compromise the integrity of your color images and, therefore, cannot be accepted. The following two websites will provide you with additional information about acceptable file formats:

http://rapidreview.com/AACR2/GUIs/moreaboutfileformats.htm
-OR-
http://cjs.cadmus.com/da/index.asp

- With your resubmission, please include a letter explaining, point by point, and clearly indicating on which pages of the manuscript changes have been made, how you have addressed each revision request or comment. Resubmissions that do not include this information will be returned unreviewed to the authors.

- A final decision will not be rendered on the revised manuscript unless we have a signed copyright transfer form on file from all authors on the manuscript.

- If your article contains a color figure(s), please be aware that color reproduction costs $750 per figure and it is the author's responsibility to assume this cost. Therefore, in the covering letter with your resubmission, please indicate whether you still want this figure printed in color or whether it can be reproduced in black and white.

REVIEWER 1:
Comments:
Although many of the concerns of the previous review have been adequately addressed, the authors are advised to make additional changes, considering the following:

1. Although PCA is now reasonably well explained, the meaning of "variance" in terms of PCA is still not obvious. For example, how does one interpret 16.5% and 1.54% variance for PC2 and PC14, respectively?

2. In the analysis showing the ability to differentiate cancer from histo-benign (page 8), the validity of using only the data from 13 of 20 cancer patients is questionable. In other words, how valid and meaningful is it to perform discriminant analysis (Fig 1c) and ROC curve analysis (Fig 1d) using only the data that showed "a separation between the cancerous and histo-benign groups on a plane of a three-dimensional plot of PC13 vs. PChol and Chol."

3. Page 8: "Further, both PCs were linearly correlated with vol% cancer cells". I couldn't find where the actual correlation coefficients are given.

4. Abstract, 3rd line: "sub-categorizing" should be replaced with sub-categorizes.

5. Page 5, last senctence of 4th paragraph: "complex" should be replaced with complexity.

6. Figure legend 1: "contained" is mispelled. Also, contrary to the text, the paired Student's t-test results for PC13, PChol and Chol don't seem to be in the figure.

Metabolic Characterization of Human Prostate Cancer with Tissue Magnetic Resonance Spectroscopy

Leo L. Cheng[1,2,*], *Melissa A. Burns*[1], *Jennifer L. Taylor*[1], *Wenlei He*[1,3]
Elkan F. Halpern[2], *W. Scott McDougal*[3] & *Chin-Lee Wu*[1,3]

Departments of Pathology[1], Radiology[2], Urology[3]
Massachusetts General Hospital
Harvard Medical School
Boston, Massachusetts 02114

Running Title: Ex vivo tissue MRS in characterizing human prostate cancer

[*]Correspondence should be addressed to L. L. Cheng, Ph.D.

Pathology Research CNY-7, 149 13th Street, Charlestown, MA 02129, USA
617-724-6593 (phone); 617-726-5684 (fax); cheng@nmr.mgh.harvard.edu

Abstract

Diagnostic advancements for prostate cancer have so greatly increased early detections that hope abounds for improved patient outcomes. However, histopathology, which guides treatment, often sub-categorizes aggressiveness insufficiently among moderately differentiated Gleason score (GS 6 and 7) tumors (>70% of new cases). Here, we test the diagnostic capability of prostate metabolite profiles measured with intact tissue magnetic resonance spectroscopy (MRS), and the sensitivity of local prostate metabolites in predicting prostate cancer statuses. Prostate tissue samples (n=199) obtained from 82 prostate cancer patients after prostatectomy were analyzed with high-resolution magic angle spinning (HRMAS) proton MRS, and afterwards with quantitative pathology. Metabolite profiles obtained from principle component analysis of MRS were correlated with pathology's quantitative findings by using linear regression analysis, and evaluated against patient pathological statuses by using ANOVA. Paired-t-tests show tissue metabolite profiles can differentiate malignant from benign samples obtained from the same patient (p<0.005), and correlate with patient serum PSA levels (p<0.006). Furthermore, metabolite profiles obtained from histologically benign tissue samples of GS6-7 prostates can delineate a subset of less aggressive tumors (p<0.008) and predict tumor perineural invasion within the subset (p<0.03). These results indicate that MRS metabolite profiles of biopsy tissues may help direct treatment plans by assessing prostate cancer pathological stage and aggressiveness, now possible to determine histopathologically only after prostatectomy.

Prostate specific antigen (PSA) screening has effectively increased detection of prostate cancer at early stages. However, histopathology cannot reliably direct treatment in the PSA testing era: more than 70% of the newly diagnosed tumors receive a Gleason score of (GS) 6 or 7, yet clinical outcomes for these patients differ markedly(1). The limited prognostic insight of such clinical measures as PSA, GS, and digital rectal exams often occasions either unnecessarily aggressive or dangerously conservative interventions(2-7). Prostate tumor heterogeneity further compromises histopathology in comprehensive evaluations, as prostate cancer cells often elude biopsy, producing false negatives(8-10). More reliable and informative prognostic tools are needed. Changes in tumor metabolism, downstream from genomic and proteomic transformations, are thought to reflect disease-related biochemical reactivity, to precede histologically observable changes in cell morphology, and thus to offer an early means for predicting tumor behaviors(11).

Recently, high-resolution magic-angle spinning (HRMAS), proton magnetic resonance spectroscopy (MRS) was developed for intact tissue analysis(12, 13). Magic-angle spinning, originally used to reduce resonance line-width in solid-state NMR, subjects samples to mechanical rotations (~kHz) at the magic-angle, (54°44') away from the direction of the spectrometer's static magnetic field while spectroscopy is recorded. Applied to intact tissues, HRMAS can produce highly-resolved spectra, allowing identification of individual metabolites, while preserving tissue pathological morphology.

We evaluated the diagnostic utility of prostate tissue metabolite profiles measured with high-field (14.1T), HRMAS proton MRS. Unaltered prostatectomy samples were analyzed spectroscopically, then histopathologically. Prostate metabolite profiles obtained from principle component analysis (PCA) of tissue spectra were correlated with pathology quantities and with patient serum PSA levels. Finally, the diagnostic potentials of tissue metabolite profiles in predicting pathological stage and tumor perineural invasion were investigated.

MATERIALS AND METHODS

Sample Collection

This study of human prostate tissue with MRS was reviewed and approved by the IRB at MGH. Samples (n=199, from 82 cancer prostatectomies) were collected from different prostate zones of the following patient population: A) Gleason score: 5 [2 Cases, 5 samples]; 6 [51, 126]; 7 [21, 53]; 8 [4, 9]; and 9 [4, 6]; and B) AJCC/TNM Stages (6^{th} ed.): T2ab [24 cases, 59 samples]; T2c [44, 112]; T3a [10, 17]; T3b [3, 5]; and T3ab [1, 6]. The few T3a, T3b and T3ab cases identified were combined and regarded in the study as T3. Surgical tissue samples were snap-frozen in liquid nitrogen and stored at -80°C until MRS. Patient clinical statuses were obtained from pathology reports.

HRMAS Proton MRS

A Bruker (Billerica, MA) AVANCE spectrometer operating at 600MHz (14.1T) was used for all MR experiments. Tissue samples were placed into a 4mm rotor with 10μl plastic inserts. 1.0μl D_2O was added for field locking. Spectra were recorded at 3°C with the spectrometer frequency set on the water resonance, and a rotor-synchronized DANTE experimental protocol was applied with spinning at 600 and 700Hz (±1.0Hz)(14). 32 transients were averaged at a repetition time of 5s.

Spectra were processed with AcornNMR-Nuts (Livermore, CA) according to the following procedures: 0.5Hz apodization before Fourier transformation, baseline correction, and phase adjustment. Resonance intensities used in the study were integrals of curve-fittings with Lorentzian-Gaussian line-shapes measured from either 600Hz or 700Hz HRMAS spectrum(14).

Quantitative Histopathology

Following spectroscopy, samples were fixed in 10% formalin, embedded in paraffin, cut into 5μm sections at 100μm intervals throughout the entire sample, and stained with hematoxylin and eosin.

An Olympus BX41 Microscope Imaging System (Melville, NY), in conjunction with the image analyzer SoftImaging-MicroSuite™ (Lakewood, CO), was used to quantify sample cross-sections. A pathologist with no knowledge of the spectroscopic results visually estimated, to the nearest 5%, the area% representing cancer cells, normal epithelial cells, and stroma in each cross-section. The vol% of these features was calculated from the sizes of the cross-sections and the corresponding area% of each pathological feature.

Statistical Analysis

The aim of the present work was to correlate spectral metabolite profiles with tissue pathologies and patient clinical statuses. Prior to investigating such correlations, the metabolite matrix was subjected to statistical data treatment – principal component analysis (PCA) to reduce the complexity of spectral data.

Since certain pathological processes can manifest simultaneous changes in multiple measurable metabolites, a change in a single metabolite may not represent the underlying process. PCA attempts to identify combinations (principal components or PCs) of the measured concentrations that may reflect distinct pathological processes if they exist in the set of the samples. A positive contribution of a certain metabolite indicates the elevation of the metabolite within the component (process), and a negative contribution suggests suppression.

The components are ordered by the extent to which they are associated with variability in the observed cases. The more metabolites affected by a process (the more associated with a PC), the greater the association. The stronger the change in the metabolites caused by a process, the greater the association. Additionally, the incidence of the process is a factor in the associated variability: extremely rare and extremely common processes cause little variability, while processes that are seen in 50% of the cases have the greatest associated variability.

Principal components may differ from the actual underlying processes in one important respect. PCs are required to be independent. Actual processes may affect some metabolites in common. For instance, one process might elevate metabolites A, B, C, and D, while suppressing E and F. A second process might elevate A and B, while suppressing C, D, E, and F. As both affect A, B, E and F in the same way, it is likely that the PCA results identify a strong component, expressing an elevation of A and B with the simultaneous suppression of E and F. Another, possibly weaker component might express metabolites C and D, and would distinguish the first process from the second.

The hypothesis that different prostate pathological features (vol% epithelia, cancer cells, stroma) possess different metabolite profiles can thus be tested by using linear regression analysis against these PCs. Paired Student t-tests were used to evaluate the ability of cancer-related PC13 and its major, contributing metabolites (phosphocholine, PChol and choline, Chol) to differentiate cancerous from histologically benign samples obtained from the same patient, while discriminant analyses were used to generate a canonical plot to achieve the maximum separation between the two groups, with accuracy being analyzed by receiver operating characteristic curves(15). Student t-tests were used to investigate the relationship between cancer-related PC14 and tumor perineural invasion. The abilities of PC2 and PC5 to differentiate between pathological stages were tested using ANOVA. Statistical analyses were carried out using SAS-JMP (Cary, NC).

RESULTS AND DISCUSSION

High-Resolution Tissue Proton MRS and PCA

HRMAS MRS permits the acquisition of high-resolution proton spectra from intact tissue, while preserving tissue architectures for subsequent histopathological analysis **(Figure 1a)**. To achieve high-resolution before HRMAS, tissue metabolites were analyzed in solutions of chemical extraction, so that results depended on the applied procedures and their completeness. Furthermore, tumor heterogeneity limits the usefulness of extraction approaches.

Histomorphological evaluations proved critical for the correct interpretation of spectroscopic data obtained from the same samples. In this study, 20/199 analyzed samples from prostate cancer patients contained cancerous glands, while the rest (n=179) represented histologically benign tissue obtained from cancerous prostates. This frequency reflects the infiltrative, heterogeneous nature of prostate cancer; producing no visible mass, its architecture precludes cancer-selective tissue removal, and thus accounts for the clinical complexity of prostate biopsy(8-10).

PCA was carried out on the concentrations of the 36 most intense resonance peaks or groups assigned to specific metabolites in order to generate PCs representing different variations of tissue metabolite profiles. Because of the existence of pathological variations among the samples, certain PCs may capture these variations. For instance, PC2, reflecting changes in polyamines, citrate, etc., was found to differentiate epithelia from stroma with statistical significance (16.5% of variance; epithelia: $r=0.381$, $p<0.0001$; stroma: $r=-0.303$, $p<0.0001$), in agreement with previous observation(16). Moreover, both PC13 and PC14 differentiate cancer from stroma (cf. PC14 represents 1.54% of variance; cancer: $r=-0.160$, $p=0.0243$; stroma: $r=0.217$, $p=0.0021$). The difference of variance representation (16.5% vs. 1.54% of the total variability of the standardized 36 metabolites for CP2 and PC14, respectively) agrees with the fact that only 10% of the samples were identified as cancer-positive, while >90% of them were designated epithelium-positive. Of note, not all PCs are related with the evaluated pathologies. Many of them may indicate intrinsic differences that are not evaluated, or variables, such as spectrometer instabilities, that are not the subjects of interest.

Differentiating Cancer from Histologically Benign Samples

By using histologically defined cancer-absent (histo-benign) samples from 13/20 patients from whom histologically cancer-positive samples were also analyzed, we observed a separation between the cancerous and histo-benign groups on a plane of a three-dimensional plot **(Figure 1b)** of PC13 vs. PChol and Chol. Both metabolites were found to be the major contributors to PC13 and PC14, in agreement with current *in vivo* and *ex vivo* MRS literature's descriptions of their relationship with malignancy(18). Further, both PCs were linearly correlated (p: 0.04, 0.02) with vol% cancer cells. Application of discriminant analysis to the three variables indicated a classification accuracy of 92.3% (**Figure 1c**). The overall accuracy of 98.2% for the identification of cancer samples was obtained from a receiver operating characteristic (ROC) curve generated from the three variables (**Figure 1d**).

Correlating with Patient Serum PSA Levels

From the 82 prostatectomy cases studied, we identified 59 cases for which patients' serum PSA levels prior to surgery were available. Among these, 111 histo-benign tissue samples from different prostate zones (central, transitional, and peripheral) were identified. We evaluated the relationship between PSA levels and tissue metabolite profiles, and found that PC2 was linearly correlated, with statistical significance, to PSA results **(Figure 2)**. Since PC2 is linearly correlated with the vol% of histo-benign epithelial cells, as previously presented, we verified that no coincidental correlation occurred between PSA levels and epithelial vol% among these measured samples.

Identifying Tumor Pathological Stages and Predicting Tumor Perineural Invasion

We examined correlations between PCs and tumor pathological stage [AJCC/TNM staging system (6th ed.)]. With all 199 samples, we observed that PC2 differentiated T2c cancer (prostate-confined; both lobes) from T3 (invading extraprostatic tissue, $p < 0.03$) and T2ab (prostate-confined; one lobe, $p < 0.005$). PC5 also differentiated T2ab cancer from T2c ($p < 0.003$) and T3 ($p < 0.00005$). Again, we verified that observed PC2 differentiation among tumor stages was independent of epithelial content (e.g. T2ab: 21.88±2.59%; T2c: 20.21±1.91%).

More interestingly, upon analysis of the histo-benign samples (n=179), similar differentiations persisted for both PCs (**Figures 3a** and **b**.). Furthermore, when the same PCs were applied to histo-benign samples of GS 6 and 7 tumors (n=162), both PCs identified the least aggressive tumor (i.e. GS 6 and T2ab tumors, n=42) from those in more aggressive groups (GS 6 T2c, GS 6 T3, and GS 7 tumors) (**Figures 3c** and **d**).

Tumor perineural invasion status, although not yet incorporated in AJCC/TMN staging, indicates prostate tumor aggressiveness and aids treatment planning(17). Unfortunately, tumor heterogeneity prevents the visualization of invasion in biopsy samples. Our evaluation yielded a statistically significant correlation between PC14 levels and invasion status for all 199 samples (126 "+" and 73 "-", $p < 0.01$), the 179 histo-benign samples (103 "+" and 71 "-", $p < 0.035$), and more interestingly, the 42 histo-benign samples from GS 6/T2ab tumors (13 "+" and 29 "-", $p < 0.028$). This last observation, combined with results shown in Figures 3e and 3f, may have great clinical significance in identifying and managing the less aggressive tumor group within the >70% newly diagnosed moderately differentiated tumors.

Our findings with respect to tumor pathological stages and perineural invasion present an important indication of the technique's potential to improve current pathology in prostate cancer diagnosis. Despite its significance in treatment planning, tumor pathological stage can now only be assessed only from resected prostate. Our observations indicate that metabolite profiles may provide a "second opinion" for prostate biopsy evaluation. They further suggest that an additional biopsy core, obtained to generate metabolite profiles, could help predict tumor stage for cancer-positive patients, even if the core itself is histo-benign.

In this report, we emphasize the phrase "histo-benign" to introduce the fact that the non-cancer status of these tissue samples was reached from histological examination. We also emphasize that currently our metabolite results are analyzed according to histopathology, which remains the "gold standard" for cancer diagnosis and treatment planning. However, evaluation of the metabolite paradigm presented, and its usefulness in the oncology clinic, may require reconsideration of the boundaries of histopathology and metabolites. Current wisdom concerning the development and progression of malignancy, such as the widely proposed stroma-effects, may assist this transformation(19, 20).

Our data leave unanswered questions. First, we cannot be certain from where, in proximity to cancer glands, our histo-benign samples were obtained. Therefore we cannot predict whether observed metabolite alterations are global or focal. Additionally, comparisons between cancer-positive and histo-benign samples rely entirely on tissue from prostate cancer patients, due to the lack of normal controls and the disqualifying metabolic degradation of tissue upon death. Our limited number of cancer-positive samples has also prevented determination of prostate pathological stage based exclusively on cancer-positive samples.

We have nevertheless shown that metabolites measured with tissue MRS correlate with histopathology findings, and that metabolite profiles reveal overall tumor clinicopathological status and aggressiveness before either is visible to histopathology. We believe the data presented here demonstrates the diagnostic and prognostic potential of the metabolite protocol. However, its clinical utility can be assessed only through longitudinal patient follow-up. Only correlations between tumor metabolites and patient outcome will allow us to establish the sensitivity and specificity of diagnostic and prognostic values for tumor metabolites, independent of current pathology.

ACKNOWLEDGEMENT:

We thank Dr. Kurt J. Isselbacher for encouragement, guidance and support. This work was supported in part by PHS/NIH grants, CA80901, CA095624 and EB002026; and by a DOD grant W81XWH-04-1-0190.

REFERENCES

1. Pound CR, Partin AW, Eisenberger MA, Chan DW, Pearson JD, Walsh PC. Natural history of progression after PSA elevation following radical prostatectomy. Jama 1999; 281: 1591-7.
2. Carter HB, Isaacs WB. Improved biomarkers for prostate cancer: a definite need. J Natl Cancer Inst 2004; 96: 813-5.
3. Incrocci L, Slob AK. Incidence, etiology, and therapy for erectile dysfunction after external beam radiotherapy for prostate cancer. Urology 2002; 60: 1-7.
4. Eton DT, Lepore SJ. Prostate cancer and health-related quality of life: a review of the literature. Psychooncology 2002; 11: 307-26.
5. Ko YJ, Bubley GJ. Prostate cancer in the older man. Oncology (Huntingt) 2001; 15: 1113-9, 23-4; discussion 24-6, 31.
6. Ransohoff DF, McNaughton Collins M, Fowler FJ. Why is prostate cancer screening so common when the evidence is so uncertain? A system without negative feedback. Am J Med 2002; 113: 663-7.
7. Smith RA, Cokkinides V, Eyre HJ. American Cancer Society guidelines for the early detection of cancer, 2003. CA Cancer J Clin 2003; 53: 27-43.
8. Zackrisson B, Aus G, Lilja H, Lodding P, Pihl CG, Hugosson J. Follow-up of men with elevated prostate-specific antigen and one set of benign biopsies at prostate cancer screening. Eur Urol 2003; 43: 327-32.
9. Mazal PR, Haitel A, Windischberger C, et al. Spatial distribution of prostate cancers undetected on initial needle biopsies. Eur Urol 2001; 39: 662-8.

10. Steiner H, Moser P, Hager M, et al. Clinical and pathologic features of prostate cancer detected after repeat false-negative biopsy in a screening population. Prostate 2004; 58: 277-82.

11. Mountford C, Doran S, Lean C, Russell P. Cancer pathology in the year 2000. Biophys. Chem. 1997; 68: 127-35.

12. Cheng LL, Lean CL, Bogdanova A, et al. Enhanced resolution of proton NMR spectra of malignant lymph nodes using magic-angle spinning. Magn Reson Med 1996; 36: 653-8.

13. Cheng LL, Ma MJ, Becerra L, et al. Quantitative neuropathology by high resolution magic angle spinning proton magnetic resonance spectroscopy. Proc Natl Acad Sci U S A 1997; 94: 6408-13.

14. Taylor JL, Wu CL, Cory D, Gonzalez RG, Bielecki A, Cheng LL. High-resolution magic angle spinning proton NMR analysis of human prostate tissue with slow spinning rates. Magn Reson Med 2003; 50: 627-32.

15. McNeil BJ, Keller E, Adelstein SJ. Primer on certain elements of medical decision making. N Engl J Med 1975; 293: 211-5.

16. Cheng LL, Wu C, Smith MR, Gonzalez RG. Non-destructive quantitation of spermine in human prostate tissue samples using HRMAS 1H NMR spectroscopy at 9.4 T. FEBS Lett 2001; 494: 112-6.

17. Beard CJ, Chen MH, Cote K, et al. Perineural invasion is associated with increased relapse after external beam radiotherapy for men with low-risk prostate cancer and may be a marker for occult, high-grade cancer. Int J Radiat Oncol Biol Phys 2004; 58: 19-24.

18. Podo F. Tumour phospholipid metabolism. NMR Biomed 1999; 12: 413-39.

19. Wong YC, Wang XH, Ling MT. Prostate development and carcinogenesis. Int Rev Cytol 2003; 227: 65-130.

20. Cooper CR, Chay CH, Gendernalik JD, et al. Stromal factors involved in prostate carcinoma metastasis to bone. Cancer 2003; 97: 739-47.

Figure Legends

Figure 1. (**a.**) High-Resolution Magic Angle Spinning (HRMAS) 1H MR spectrum of intact tissue obtained from the removed prostate of a 61 y.o. patient with Gleason score 6, T2b tumors. Histopathology analysis of the tissue sample (insert) after its spectroscopy measurement revealed that the sample contained 40% histopathologically defined benign epithelium and 60% stromal structures, with no identifiable cancerous glands. Cellular metabolites mentioned in the text are labeled on the spectrum. The 36 most intense resonance peaks or metabolite groups above the horizontal bars were selected for analyses, while the other regions were excluded from calculation, partly due to surgery-related alcohol contamination. (**b**) 3D plot of Principal Component 13 (PC13 correlates linearly with vol% of cancer cells in tissue samples) vs. phosphocholine (Pchol) vs. choline (Chol). Cancerous and histologically benign (histo-benign) tissue samples from 13 patients can be visually separated in observation plane. The paired Student's t-test (cancer vs. histo-benign from the same patients) results for PC13, PChol and Chol are: 0.012, 0.004, and 0.001. Only results from these 13 patients could be evaluated with paired tests, for other cancer positive samples were collected from patients with whom no histo-benign samples were analyzed. (**c**) The canonical plot resulting from discriminant analysis of the three variables in Fig. 1b. presents the maximum separation between the two groups. (**d**) The resulting receiver operating characteristic (ROC) curves indicates the accuracy of using the three variables in Fig. 1b. to positively identify cancer samples.

Figure 2. Statistically significant correlation between the patient serum PSA levels before prostatectomy and the metabolite profiles represented by Principal Component 2 (PC2), as measured from 111 histo-benign prostate tissue samples obtained from 59 prostatectomy cases

for prostate cancer. PC2 values plotted in the figure represent the linear combinations of metabolite concentrations according to the PC2 formula obtained from PCA.

Figure 3. Principal Component 2 (PC2) and Principal Component 5 (PC5) as predictors of tumor stage. (**a**) PC2 can differentiate T2c stage tumors from T2ab and T3 tumors; while (**b**) PC5 can differentiate T2ab from T2c and T3 stages, as defined by AJCC/TNM staging system (6th ed.) with with histo-benign samples; and with histo-benign GS 6 and 7 samples (**c, d**). In the latter, PC2 and PC5 can differentiate among three tumor groups: 1) GS 6, T2ab, 2) GS 6, T2c, and 3) GS 6, T3 plus GS 7 tumors.

Figure 1.

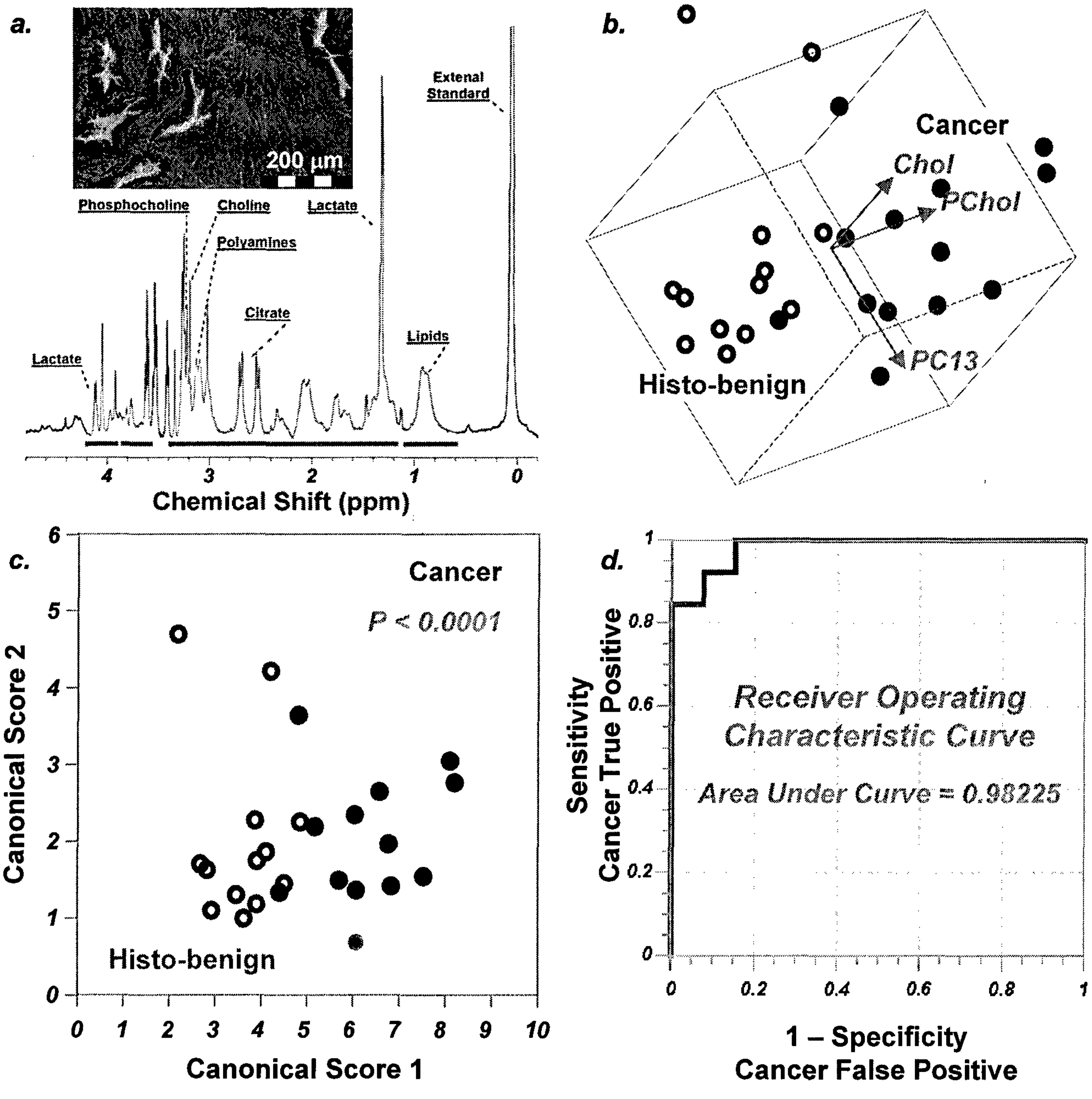
a.
200 µm
Extenal Standard
Phosphocholine
Choline
Polyamines
Lactate
Citrate
Lipids
Lactate
4
3
2
1
0
Chemical Shift (ppm)
b.
Cancer
Chol
PChol
PC13
Histo-benign
c.
Cancer
P < 0.0001
Histo-benign
Canonical Score 2
Canonical Score 1
0
1
2
3
4
5
6
7
8
9
10
d.
Receiver Operating Characteristic Curve
Area Under Curve = 0.98225
Sensitivity
Cancer True Positive
1 – Specificity
Cancer False Positive
0
0.2
0.4
0.6
0.8
1

Figure 2.

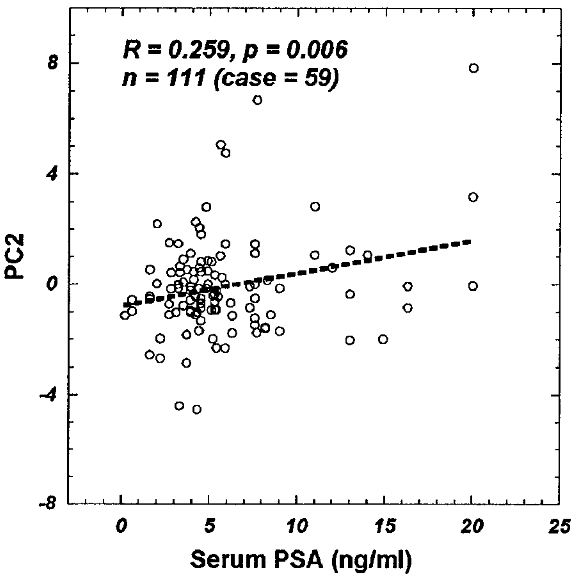
R = 0.259, p = 0.006
n = 111 (case = 59)
PC2
8
4
0
-4
-8
0
5
10
15
20
25
Serum PSA (ng/ml)

Figure 3.

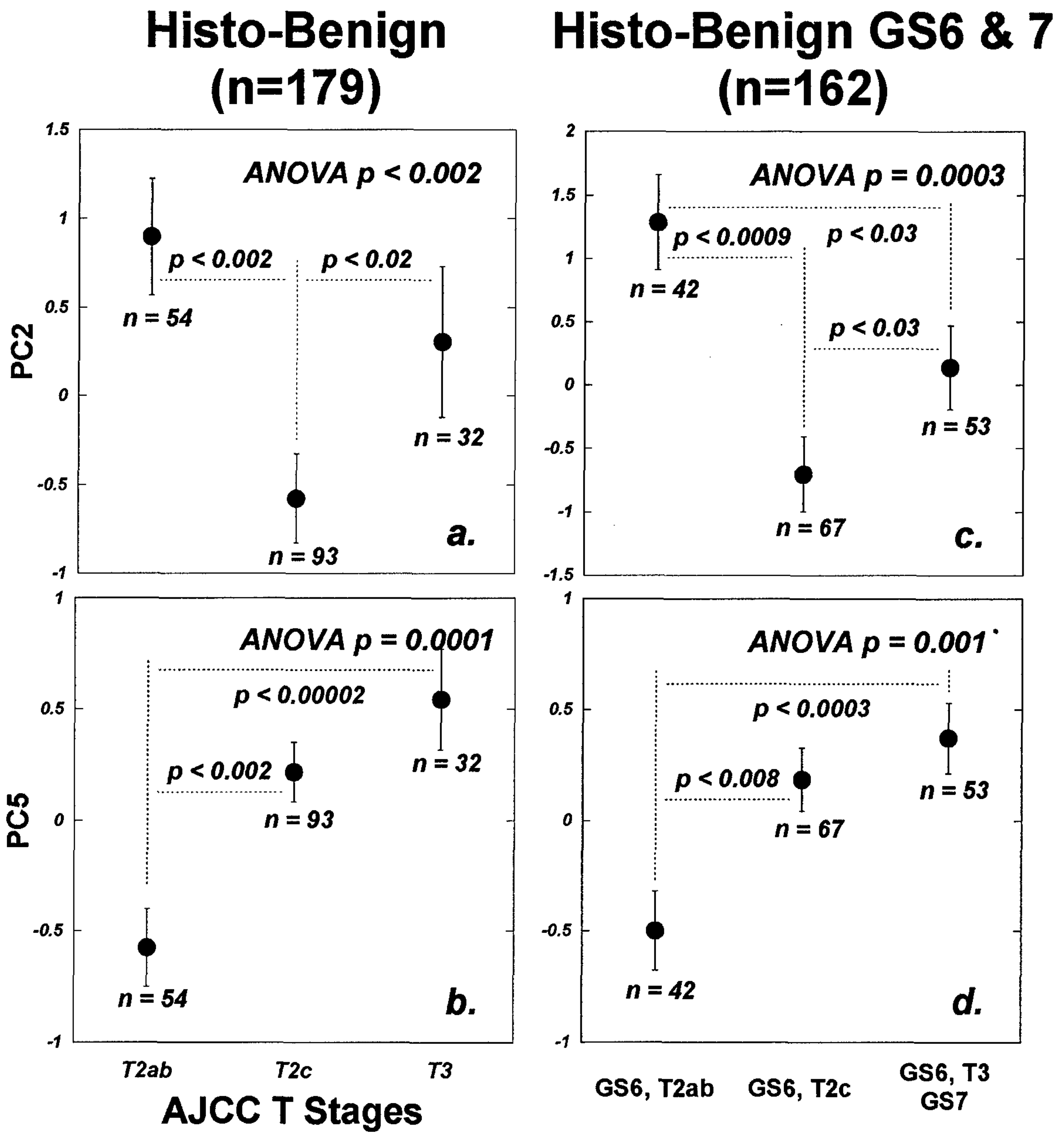
Histo-Benign
(n=179)
Histo-Benign GS6 & 7
(n=162)
PC2
1.5
1
0.5
0
-0.5
-1
ANOVA p < 0.002
p < 0.002
p < 0.02
n = 54
n = 93
n = 32
a.
2
1.5
1
0.5
0
-0.5
-1
-1.5
ANOVA p = 0.0003
p < 0.0009
p < 0.03
p < 0.03
n = 42
n = 67
n = 53
c.
PC5
1
0.5
0
-0.5
-1
ANOVA p = 0.0001
p < 0.00002
p < 0.002
n = 54
n = 93
n = 32
b.
1
0.5
0
-0.5
-1
ANOVA p = 0.001
p < 0.0003
p < 0.008
n = 42
n = 67
n = 53
d.
T2ab
T2c
T3
AJCC T Stages
GS6, T2ab
GS6, T2c
GS6, T3
GS7

Quantification of Phosphocholine and Glycerophosphocholine with ^{31}P edited ^{1}H NMR Spectroscopy

Nikolaus M. Loening,[1] Anne M. Chamberlin,[1] Andrea G. Zepeda,[2]
R. Gilberto Gonzalez,[3] Leo L. Cheng[2, 3,*]

[1]Department of Chemistry, Lewis & Clark College, 0615 SW Palatine Hill Road, Portland, Oregon 97219, USA.

Departments of [2]Pathology and [3]Radiology, Massachusetts General Hospital, Harvard Medical School, Boston, MA 02129, USA.

Running Title: ^{31}P Edited ^{1}H NMR Spectroscopy for PC and GPC.

[*]**Correspondence to:** Leo L. Cheng, Pathology Research, CNY-7, 149 13th Street, Charlestown, MA 02129; 617-724-6593 (Phone); 617-726-5684 (Fax); E-mail: cheng@nmr.mgh.harvard.edu.

Sponsors: N.M.L. thanks the National Institutes of Health for support via a National Research Service Award post-doctoral fellowship (F32 NS42425-01). This work is supported in part by NIH NCI grants CA77727, CA095624, CA83159 and by NIH NIBIB grant EB002026, and a DOD grant W81XWH-04-1-0190.

Abstract

Choline and the related compounds phosphocholine (PC) and glycerophosphocholine (GPC) are metabolites that are considered to be important in oncology. Past studies have demonstrated correlations linking the relative ratios and concentrations of these metabolites with the development and progression of cancer. Currently, *in vivo* and tissue *ex vivo* magnetic resonance spectroscopy methods have mostly centered on measurements of the total concentration of these metabolites and have difficulties in differentiating between them. Here, a new scheme that uses ^{31}P edited ^{1}H spectroscopy to quantify the concentrations of choline, PC, and GPC in biological samples is reported and its applicability is demonstrated using samples of human brain tumors extracts. This method is particularly well-suited for analytical situations where the PC and GPC resonances are not sufficiently resolved and/or obscured by other metabolites. Consequently, this scheme has the potential to be used for the analysis of choline compounds in *ex vivo* tissue samples.

Key Words: ^{31}P edited ^{1}H NMR, INEPT, Choline-compounds, Human Brain Tumor Extracts.

Abbreviations: phosphocholine (PC), glycerophosphocholine (GPC), insensitive nuclei enhanced by polarization transfer (INEPT)

Introduction

Choline and the related compounds phosphocholine (PC) and glycerophosphocholine (GPC) are essential nutrients that function as substrates in many major bio-metabolic pathways. These choline-compounds participate in a number of biological processes ranging from the normal development of the brain and liver in infants[1] to various pathological conditions such as the progression of neoplasm[2]. Although the biochemical functions of these compounds have been studied for decades, their unique importance has only come to light over the past 20 years with the application of NMR spectroscopy to medical science.

The relationship between the concentrations of choline-compounds and pathology has been measured and documented for many medical conditions, such as HIV infections[3], traumatic brain injuries[4], schizophrenia[5], neuro-degenerative[6] and neuro-genetic[7] disorders, chronic fatigue[8], and multiple sclerosis[9], as well as for the processes of normal development[10] and aging[11]. However, one of the most studied connections has been with cancer[12-18]. In general, the concentrations of choline-compounds are elevated in cancer and, more importantly, *ex vivo* studies of tissue extract samples suggest that the ratio of the phospho derivatives indicate the status of the disease[19-21]. The signals of the methyl (–$N(CH_3)_3$) protons has been used to differentiate choline (3.185 ppm) from PC (3.208 ppm) and GPC (3.212 ppm) in *ex vivo* analyses[22]. Unfortunately, present NMR based *in vivo* techniques cannot differentiate the methyl protons of choline from those of PC and GPC as their signals are separated by less than 0.03 ppm. For *ex vivo* samples of intact tissue, the methyl protons of choline can be differentiated from those of the other choline compounds using high-resolution magic angle spinning proton NMR spectroscopy. However, differentiating between the methyl protons of PC and GPC is a great challenge because the chemical shift separation between these PC and GPC protons is very small (0.007 ppm, see results below) [23,24] and therefore, even at moderate field strengths (e.g. 400 MHz), the resonances are difficult to resolve. As a result, it is currently almost impossible to quantify these metabolites simultaneously *in vivo*. Although *ex vivo* quantification of all three compounds is possible using the methyl proton signals, it is difficult and requires techniques such as peak deconvolution during post-processing or two-dimensional spectroscopy[25-28].

Here, we introduce a scheme that can efficiently differentiate and quantify choline, PC, and GPC, and demonstrate its applicability to both model compounds and extracts of human brain tissue. The crux of this method is the use of phosphorous (^{31}P) edited proton (^{1}H) NMR spectroscopy to measure signals from the $^{1}CH_2$ protons (see figure 1). These protons have a spectral separation that is about 20 times greater than that between the methyl protons (0.13 ppm versus 0.007 ppm). The ^{31}P editing is accomplished using the scalar couplings between the ^{31}P nucleus and the $^{1}CH_2$ protons in PC and GPC. Although the sensitivity of this technique suffers compared to the analysis of the methyl protons, the better resolution of the $^{1}CH_2$ protons allows for analysis in situations where the individual methyl proton resonances from the three choline compounds are not resolved. Consequently, we believe our approach can be applied to *ex vivo* analyses of biological specimens and, if sensitivity issues can be resolved, has the potential to be incorporated into *in vivo* examinations in which a multi-channel magnetic resonance scanner is available.

Experimental

The NMR experiments were carried out on either a vertical standard-bore Bruker AVANCE spectrometer operating at 600 MHz (14.1 T) equipped with a Bruker $^{31}P/^{13}C/^{15}N - ^{1}H$ inverse-geometry *z*-axis gradient probe, or on a vertical standard-bore Bruker AVANCE spectrometer operating at 300 MHz (7.05 T) equipped with a Bruker broadband inverse-geometry *z*-axis gradient probe. The pulse sequence developed for the experiment is shown in figure 2. It consists of two INEPT steps[29] that transfer the initial ^{1}H magnetization to ^{31}P and then back to ^{1}H. Inserted into these INEPT steps are selective 180° pulses that only affect the $^{2}CH_2$ protons and, consequently, refocus the scalar coupling between the $^{1}CH_2$ and $^{2}CH_2$ protons. These selective pulses are essential because the ^{1}H-^{1}H couplings are similar in size to the ^{31}P-^{1}H couplings. Without the selective pulses, the effect of the ^{1}H-^{1}H couplings during the INEPT delays would be to transform the single quantum coherences arising from the $^{1}CH_2$ protons into multiple quantum coherences. Pulsed field gradients are used in conjunction with phase cycling to eliminate unwanted signals in the ^{31}P edited ^{1}H spectra. The gradients G_1 and G_2 impart a phase label to the ^{31}P magnetization that is later refocused by the final coherence selection gradient, G_3, after the magnetization has been transferred to ^{1}H. Finally, a zero-quantum filter is included at the end of the sequence to further attenuate contributions from undesired coherence transfer pathways[30].

A recycle time of 10 seconds was used for both the regular and ^{31}P edited experiments to ensure that the sample magnetization was at equilibrium before every scan. During the recycle delay, the HOD resonance was saturated with a weak radio frequency field ($\gamma B_1/2\pi = 50$ Hz). Low power WALTZ-16 decoupling[31] ($\gamma B_1/2\pi = 625$ Hz) was used on the ^{31}P channel during acquisition to narrow the lines of the PC and GPC $^{1}CH_2$ resonances; this resulted in an increase (20%) in the sensitivity of the experiment. For the high power pulses, the radiofrequency field strength ($\gamma B_1/2\pi$) was 40 kHz for ^{1}H and 10 kHz for ^{31}P on the 14 T instrument, and 35 kHz for ^{1}H and 20 kHz for ^{31}P on the 7 T instrument. For experiments with ^{1}H decoupling a 2.5 kHz decoupling field was used.

In the ^{31}P edited experiments, Gaussian 180° pulses were used to selectively decouple the ^{1}H homonuclear scalar couplings during the INEPT steps. The selective pulses were 5 ms on the 14 T system and 10 ms on the 7 T system; for both systems the pulses were applied at 3.3 ppm. Consequently, these pulses refocused the $^{2}CH_2$ protons of choline, PC, and GPC, but left the $^{1}CH_2$ protons of these molecules unperturbed. The gradients G_1, G_2, G_3, and G_4 were set to 35, 15, 20, and 1 G cm^{-1} and were 2.47, 2.47, 1, and 10 ms in length, respectively. The first three gradients were shaped to a half-sine bell; the shape of the fourth gradient was constant over the central 80% of the pulse and was smoothly ramped on and off at the ends of the pulse.

The sample temperature was maintained at 10 °C with a cooling gas flow rate of 535 L hr^{-1} for the experiments at 14 T to minimize any potential problems due to sample degradation. The experiments at 7 T were performed at 25 °C. The temperature was controlled to better than ±0.2°C during the experiments; temperature stability is important for quantitation as the efficiency of the heteronuclear transfer steps varies with temperature.

Standards: For the standard samples, all spectra were acquired with 16 scans; each spectrum required three minutes to complete. The pH of each sample was adjusted to be in the range of 6 to 7.5 by adding small amounts of HCl or NaOH.

Solutions of Human Brain Tumor Metabolites: Eleven samples of human glioma (malignant brain tumor) extracts were prepared using the FastPrep™ and Speed Vac® systems (Thermo Savant, Holbrook, NY) according to the following procedure. Between 100 and 200 mg of frozen tissue samples from surgeries or autopsies were transferred into Lysing Matrix D tubes (Qbiogene, Carlsbad, CA) along with 1.2 mL of methanol. The sample tubes were then placed in the FastPrep™ system and processed for 35 seconds on speed dial 4.0. This was repeated at least three times and until no visible tissue pieces remained. Next, a modified methanol/chloroform extraction was carried out[32]. The resulting aqueous layer of brain metabolites was dried with the Speed Vac® system and redissolved in D_2O. The pH of these samples was adjusted to be in the range of 7 to 8. Since this preparation method is not a calibrated protocol for metabolite quantification, the evidence of loss in absolute metabolite concentrations was observed. For instance, the mean concentration for total choline was determined to be 0.31 ± 0.07 mM, which was about only 25% of the literature values (1.24 ± 0.10 mM) for extracts of tumor tissues of similar type [33-35]. However, this did not interfere with the aim of this work, which was to show that it is possible to correlate spectral results obtained from a ^{1}H spectrum to those from a ^{31}P edited ^{1}H spectrum for a single sample to determine the comparative, rather than the absolute metabolite concentrations of brain metabolites in an extract sample. The ^{1}H spectra for the brain extracts were acquired using 1024 scans, resulting in an experiment time of 3.2 hr. The ^{31}P edited ^{1}H spectra were acquired using between 3096 and 5192 scans, resulting in experiment times of between 9.8 and 16.3 hr.

Results

^{31}P Edited Spectra of the Standards: The proposed method concentrates on the measurement of signals from the $^{1}CH_2$ protons instead of the more intense signals that arise from the methyl protons. There are two main advantages associated with this approach. First, as seen in the regular ^{1}H spectrum shown in figure 3, the signals from the $^{1}CH_2$ protons are dispersed over a range of 0.13 ppm instead of the 0.007 ppm range of the methyl protons. This suggests that the measurement of the $^{1}CH_2$ protons is better suited for situations, such as *ex vivo* tissue analyses, where the spectral resolution is limited to the point that the individual methyl resonances can not be resolved. The second advantage is that the $^{1}CH_2$ protons for PC and GPC have observable (~6.1 and 6.3 Hz, respectively [22]) couplings to the ^{31}P nucleus, which allows the acquisition of ^{31}P edited spectra. This fact is important as, without ^{31}P editing, the ^{1}H signals of the choline-compounds (especially those from the $^{1}CH_2$ resonances) are mingled with signals from other metabolites, making them difficult to quantify or even to identify.

The main disadvantage of our method is that the signal intensity of the $^{1}CH_2$ protons is weaker than that of the methyl protons (note the separate scale used for the methyl region in figure 3). Nevertheless, the quality of the ^{31}P editing allows the relatively weak $^{1}CH_2$ peaks to be easily resolved and measured in a ^{31}P edited ^{1}H spectrum, as shown in figure 4. With ^{31}P editing, the only peaks that remain in the ^{1}H spectrum are those from the $^{1}CH_2$ protons of PC and GPC. The signal from the $^{1}CH_2$ protons of choline, which would have appeared at 3.95 ppm, is completely removed as are the intense methyl signals at ~3 ppm from all three choline-compounds. An artifact remains from the residual water signal at 4.7 ppm, but this is resolved from the peaks of interest and has an integral of nearly zero. The amount of PC and GPC can thus be quantified from the ^{31}P edited ^{1}H spectrum. Signals from choline are removed in the ^{31}P edited ^{1}H spectra, so it is not possible to determine its concentration directly from the edited spectrum. However, the quantitative relationship between the ^{31}P edited and the regular ^{1}H spectra can be exploited to determine the choline concentration. This is accomplished by determining the PC and GPC concentrations from the edited spectrum, and then using this information to subtract their contributions from the total integrated intensity of the methyl protons in the regular ^{1}H spectrum. The remaining intensity corresponds to the concentration of choline. As a result, it is possible to determine the relative concentrations of all three species without having to resolve the individual contributions to the total methyl signal in the regular ^{1}H spectrum.

Quantification of the amount of choline, PC, and GPC in a sample depends on the transfer efficiency of the INEPT steps. This means that the quantitative relationship between the conventional ^{1}H spectra and the ^{31}P edited ^{1}H spectra depends on the ^{31}P-^{1}H coupling constants, pulse imperfections, and the transverse and longitudinal relaxation rates. The coupling constants are largely insensitive to sample conditions and the INEPT steps are reasonably tolerant of variations in pulse calibration, so the main difficulty with establishing the transfer efficiency stems from variations in the relaxation rates. For the range of concentrations used in our standard samples, we found that the transfer efficiencies were mostly independent of the relative concentrations of choline, PC, and GPC. However, relaxation rates (and therefore the transfer efficiency) depend on temperature so it is important that the transfer efficiency is established for the temperature to be used for all the experiments. For our experiments with brain tissue samples (at 10° C) we observed signal intensities in the ^{31}P edited spectra that were 13.4% and 18.5% of the unedited signal intensities for PC and GPC, respectively. These results are 54% and 74% of the theoretical maximum transfer efficiency of 25% (see discussion section). At room temperature the transfer efficiency increases to close to the theoretical values (25%) for both PC and GPC, as would be expected based on the connection between temperature and relaxation rates for small molecules in solution.

Quantification of Choline, PC, and GPC for the Standards: To test the accuracy of the ^{31}P editing protocol, we compared the results measured from the ^{31}P edited ^{1}H spectra with those obtained directly from the regular ^{1}H spectra for a series of standard samples consisting of PC/GPC/choline in D_2O at 14 T. The top half of figure 5 shows the relationships between the concentrations of choline, PC, and GPC estimated from the ^{31}P edited ^{1}H spectra and those determined directly from the regular ^{1}H spectra. As previously discussed, the choline concentration for each sample was estimated by taking the integral of all three methyl resonances in the regular ^{1}H spectrum and then subtracting the PC and GPC contributions as calculated from the ^{31}P edited ^{1}H spectrum. The data show that there is a strong and quantitative correlation between these two methods for determining the concentrations.

Analyses of Human Brain Extracts: We tested the applicability of ^{31}P editing for the quantification of choline, PC, and GPC in biological samples using a series of 11 human glioma extract samples. Representative spectra for one of these samples are shown in figure 6. From the spectrum shown in figure 6b, it is clear that the $^{1}CH_2$ resonances are overlapped by peaks from other metabolites in the regular ^{1}H spectrum; this problem also affects the methyl resonances, although to a smaller extent. The complexity of the spectrum makes it very difficult to quantify the relative amounts of the choline-compounds based on just the regular ^{1}H spectrum. This problem would be greatly exacerbated using an instrument at lower field or in the analysis of *ex vivo* tissue samples. On the other hand, in the ^{31}P edited ^{1}H spectrum (figure 6c), the ^{1}CH$_2$ resonances are clearly resolved and the relative amounts of PC and GPC can be easily quantified. The additional peaks seen in the ^{31}P edited ^{1}H spectrum arise from other phosphorous containing brain metabolites may result from phosphoethanolamine (PE) and glycerophosphoethanolamine (GPE) [22], which may require further investigations. If these additional peaks are from PE and GPE, than the use of ^{31}P edited ^{1}H spectra instead of regular ^{1}H spectra for PC and GPC quantification will be even more advantageous. This is because the PE and GPE peaks that are observed in the ^{31}P edited ^{1}H spectra appear at different chemical shifts and therefore do not affect the quantification of the ^{1}CH$_2$ resonances from PC and GPC. This is in contrast to regular ^{1}H spectra where PE and GPE interfere with the quantification of the methyl peaks at around 3 ppm for PC, GPC, and choline [22].

The concentrations of the choline-compounds determined for the brain extract samples by fitting the methyl peaks in the regular ^{1}H spectra versus concentrations determined using the ^{31}P edited ^{1}H spectra are shown in the bottom half of figure 5. These graphs show a reasonable degree of correlation. The variation seen in these graphs is not surprising due to the general unreliability of results determined by fitting the methyl peaks from the regular ^{1}H spectra. This unreliability arises due to the lack of baseline resolution between the peaks and because of the presence of other components in the spectrum that overlap with the methyl peaks. These are the very issues that make the methyl peaks unsuitable for analysis in *ex vivo* tissue samples.

Discussion

^{31}P Spectroscopy versus ^{31}P edited ^{1}H Spectroscopy: As the ^{31}P resonances of PC and GPC differ from one another by ~4.5 ppm, it could be argued that a better approach for the quantification of PC and GPC concentrations would be to directly observe the ^{31}P signal[36-40]. In fact, with the development and availability of high field MR imagers, it has been demonstrated recently that PC and GPC can be observed from in vivo ^{31}P spectroscopy at 7 T from a voxel size of 27 ml [41]. However, it may be better to utilize the improved sensitivity of ^{1}H nuclei for detection due to the higher magnetogyric ratio of ^{1}H, especially if an inverse geometry probehead is in use (as is often the case for ex vivo studies). This is clearly demonstrated in figure 4. For these spectra, the signal-to-noise ratio for the PC and GPC $^{1}CH_2$ resonances in the ^{31}P edited ^{1}H experiment is approximately six times the signal-to-noise ratio of the PC and GPC resonances in the ^{31}P detected (^{1}H decoupled) experiment. The signal-to-noise ratio was calculated as the ratio of the PC or GPC peak *heights* (intensities) versus the root-mean-square noise of a region of the spectrum without signals. However, quantitation usually makes use of the peak *integrals*, so comparing signal-to-noise ratios underestimates the advantages of the ^{31}P-filtered ^{1}H experiment. This is because the ^{31}P signals are approximately 10 times narrower than the $^{1}CH_2$ resonances in the ^{31}P filtered ^{1}H experiment. Due to the longer relaxation times for ^{31}P versus ^{1}H nuclei, the signal-to-noise advantage of the ^{31}P edited ^{1}H experiment is even better when considering signal-to-noise per unit time for situations where extensive signal averaging is required.

Signal Intensities in ^{31}P Edited ^{1}H Spectra: The use of a ^{31}P filter for editing in these experiments significantly reduces the resulting signal intensity because of the added restrictions to the coherence transfer pathway. In theory, the edited spectrum should have 50% of the intensity of the unedited spectrum if only phase cycling is used for selecting the coherence transfer pathway. However, we found that it was useful to supplement the phase cycling with pulsed field gradients. The use of gradient selection greatly attenuates artifacts in the spectra but comes at the prices of an additional factor of two in signal intensity, resulting in a total theoretical transfer efficiency of 25%.

INEPT Transfer versus Hartman-Hahn Mixing: We note that we also attempted to use heteronuclear Hartman-Hahn mixing[42] for the heteronuclear transfer steps. However, the transfer efficiencies that we measured using these mixing sequences were much lower than with INEPT transfers; we observed that the signal intensities derived using heteronuclear Hartman-Hahn mixing were less than 3% of the unedited spectra. These inefficiencies are attributable to the longer periods needed to conduct heteronuclear Hartman-Hahn transfers and to interference from homonuclear Hartman-Hahn mixing.

Realistic Length of Experimental Time: Due to the extremely low metabolite concentrations that resulted from the use of a non-quantitative extraction procedure for the preparation of the human glioma samples used in this study, the ^1H spectra for the brain extracts were acquired using 1024 scans, resulting in an experiment time of 3.2 hr. Furthermore, the ^{31}P edited ^1H spectra were acquired using between 3096 and 5192 scans, resulting in quite lengthy experiment times of between 9.8 and 16.3 hr. Since the aim of the work was to correlate spectral results obtained directly from a ^1H spectrum with those from a ^{31}P edited ^1H spectrum using the same sample, rather than the determination of the absolute metabolite concentrations for the sample, these unusually low absolute metabolite concentrations do not interfere with the results of the study. Due to the low metabolite concentrations as well as other factors, the measurement times used for these experiments are much longer than what is actually needed. If samples were used with metabolite concentrations similar to those reported in the literature (which are about four times higher than the samples used for this study), then a SNR equivalent to the results shown in this paper could be achieved while reducing the experiment time by a factor of 16. In addition, the signal-to-noise ratio (SNR) shown in figure 6 is greater than what is actually needed for quantification. If half the SNR were used then the experiments could have been completed in 25% of the time. If these two changes are combined than the experiment time could easily be reduced by a factor of 64. This would turn our 9.8 *hour* experiments into 9.5 *minute* experiments. Finally, experiment times can be further shortened by using shorter recycle delays as long as care is taken to ensure that the results remain quantitative, or that all samples are analyzed using the same conditions if the goal of the study is disease diagnosis.

Conclusion

We have demonstrated a scheme that uses ^{31}P edited ^{1}H NMR spectroscopy to quantify the concentrations of choline, phosphocholine, and glycerophosphocholine in biological samples. This method is particularly well-suited for analytical situations in which the $^{1}CH_2$ resonances are obscured by other metabolites and the methyl resonances are not sufficiently resolved. We believe this method will be applicable for the analysis of choline compounds in *ex vivo* tissue samples. In addition, we believe that this method has potential for the *in vivo* non-destructive quantification of choline, PC, and GPC provided that the sensitivity of detecting the $^{1}CH_2$ resonances does not pose to great a challenge.

Acknowledgements.

The authors thank Profs. Robert G. Griffin and Franca Podo for useful discussion and Dr. Anthony Bielecki for assistance.

References

1. Holmes HC, Snodgrass GJ, Iles RA. Changes in the choline content of human breast milk in the first 3 weeks after birth. Eur J Pediatr 2000;**159**(3):198-204. 195: Podo F. Tumour phospholipid metabolis...[PMID:10654290]Related Articles, Links.
2. Podo F. Tumour phospholipid metabolism. NMR Biomed 1999;**12**(7):413-439. 416: Murphy PS, et al. Signal modulation in (411)H mag...[PMID:10571938]Related Articles, Links.
3. Chang L, Ernst T, Witt MD, Ames N, Walot I, Jovicich J, DeSilva M, Trivedi N, Speck O, Miller EN. Persistent brain abnormalities in antiretroviral-naive HIV patients 3 months after HAART. Antivir Ther 2003;**8**(1):17-26.
4. Brenner T, Freier MC, Holshouser BA, Burley T, Ashwal S. Predicting neuropsychologic outcome after traumatic brain injury in children. Pediatr Neurol 2003;**28**(2):104-114.
5. Delamillieure P, Constans JM, Fernandez J, Brazo P, Benali K, Courtheoux P, Thibaut F, Petit M, Dollfus S. Proton magnetic resonance spectroscopy (1H MRS) in schizophrenia: investigation of the right and left hippocampus, thalamus, and prefrontal cortex. Schizophr Bull 2002;**28**(2):329-339.
6. Firbank MJ, Harrison RM, O'Brien JT. A comprehensive review of proton magnetic resonance spectroscopy studies in dementia and Parkinson's disease. Dement Geriatr Cogn Disord 2002;**14**(2):64-76.
7. Brockmann K, Dechent P, Meins M, Haupt M, Sperner J, Stephani U, Frahm J, Hanefeld F. Cerebral proton magnetic resonance spectroscopy in infantile Alexander disease. J Neurol 2003;**250**(3):300-306.
8. Chaudhuri A, Condon BR, Gow JW, Brennan D, Hadley DM. Proton magnetic resonance spectroscopy of basal ganglia in chronic fatigue syndrome. Neuroreport 2003;**14**(2):225-228.
9. Arnold DL, De Stefano N, Narayanan S, Matthews PM. Proton MR spectroscopy in multiple sclerosis. Neuroimaging Clin N Am 2000;**10**(4):789-798 ,ix-x.
10. Filippi CG, Ulug AM, Deck MD, Zimmerman RD, Heier LA. Developmental delay in children: assessment with proton MR spectroscopy. AJNR Am J Neuroradiol 2002;**23**(5):882-888.
11. Sijens PE, den Heijer T, Origgi D, Vermeer SE, Breteler MM, Hofman A, Oudkerk M. Brain changes with aging: MR spectroscopy at supraventricular plane shows differences between women and men. Radiology 2003;**226**(3):889-896.
12. Galanaud D, Chinot O, Nicoli F, Confort-Gouny S, Le Fur Y, Barrie-Attarian M, Ranjeva JP, Fuentes S, Viout P, Figarella-Branger D, Cozzone PJ. Use of proton magnetic resonance spectroscopy of the brain to differentiate gliomatosis cerebri from low-grade glioma. J Neurosurg 2003;**98**(2):269-276.
13. Rijpkema M, Schuuring J, Van Der Meulen Y, Van Der Graaf M, Bernsen H, Boerman R, Van Der Kogel A, Heerschap A. Characterization of oligodendrogliomas using short echo time 1H MR spectroscopic imaging. NMR Biomed 2003;**16**(1):12-18.

14. Lindskog M, Kogner P, Ponthan F, Schweinhardt P, Sandstedt B, Heiden T, Helms G, Spenger C. Noninvasive estimation of tumour viability in a xenograft model of human neuroblastoma with proton magnetic resonance spectroscopy (1H MRS). Br J Cancer 2003;**88**(3):478-485.
15. Howe FA, Barton SJ, Cudlip SA, Stubbs M, Saunders DE, Murphy M, Wilkins P, Opstad KS, Doyle VL, McLean MA, Bell BA, Griffiths JR. Metabolic profiles of human brain tumors using quantitative in vivo 1H magnetic resonance spectroscopy. Magn Reson Med 2003;**49**(2):223-232.
16. El-Sayed S, Bezabeh T, Odlum O, Patel R, Ahing S, MacDonald K, Somorjai RL, Smith IC. An ex vivo study exploring the diagnostic potential of 1H magnetic resonance spectroscopy in squamous cell carcinoma of the head and neck region. Head Neck 2002;**24**(8):766-772.
17. Katz-Brull R, Lavin PT, Lenkinski RE. Clinical utility of proton magnetic resonance spectroscopy in characterizing breast lesions. J Natl Cancer Inst 2002;**94**(16):1197-1203.
18. Nakagami K, Uchida T, Ohwada S, Koibuchi Y, Suda Y, Sekine T, Morishita Y. Increased choline kinase activity and elevated phosphocholine levels in human colon cancer. Jpn J Cancer Res 1999;**90**(4):419-424. 418: Sabatier J, et al. Characterization of choline c...[PMID:10084669]Related Articles, Links.
19. Sabatier J, Gilard V, Malet-Martino M, Ranjeva JP, Terral C, Breil S, Delisle MB, Manelfe C, Tremoulet M, Berry I. Characterization of choline compounds with in vitro 1H magnetic resonance spectroscopy for the discrimination of primary brain tumors. Invest Radiol 1999;**34**(3):230-235.
20. Morvan D, Demidem A, Papon J, De Latour M, Madelmont JC. Melanoma tumors acquire a new phospholipid metabolism phenotype under cystemustine as revealed by high-resolution magic angle spinning proton nuclear magnetic resonance spectroscopy of intact tumor samples. Cancer Res 2002;**62**(6):1890-1897. 1893: Reo NV, et al. Kinetic analyses of liver pho...[PMID:11880242]Related Articles, Links.
21. Katz-Brull R, Margalit R, Degani H. Differential routing of choline in implanted breast cancer and normal organs. Magn Reson Med 2001;**46**(1):31-38. 31: Venkatesh SK, et al. Spectroscopic increase in cho...[PMID:11436208]Related Articles, Links.
22. Govindaraju V, Young K, Maudsley AA. Proton NMR chemical shifts and coupling constants for brain metabolites. NMR Biomed 2000;**13**(3):129-153.
23. Cheng LL, Ma MJ, Becerra L, Ptak T, Tracey I, Lackner A, Gonzalez RG. Quantitative neuropathology by high resolution magic angle spinning proton magnetic resonance spectroscopy. Proc Natl Acad Sci U S A 1997;**94**(12):6408-6413.
24. Sitter B, Sonnewald U, Spraul M, Fjosne HE, Gribbestad IS. High-resolution magic angle spinning MRS of breast cancer tissue. NMR Biomed 2002;**15**(5):327-337.
25. Ala-Korpela M, Posio P, Mattila S, Korhonen A, Williams SR. Absolute quantification of phospholipid metabolites in brain-tissue extracts by 1H NMR spectroscopy. J Magn Reson B 1996;**113**(2):184-189.

26. Moreno A, Lopez LA, Fabra A, Arus C. 1H MRS markers of tumour growth in intrasplenic tumours and liver metastasis induced by injection of HT-29 cells in nude mice spleen. NMR Biomed 1998;**11**(3):93-106.
27. Morvan D, Demidem A, Papon J, De Latour M, Madelmont JC. Melanoma tumors acquire a new phospholipid metabolism phenotype under cystemustine as revealed by high-resolution magic angle spinning proton nuclear magnetic resonance spectroscopy of intact tumor samples. Cancer Res 2002;**62**(6):1890-1897.
28. Morvan D, Demidem A, Papon J, Madelmont JC. Quantitative HRMAS proton total correlation spectroscopy applied to cultured melanoma cells treated by chloroethyl nitrosourea: demonstration of phospholipid metabolism alterations. Magn Reson Med 2003;**49**(2):241-248.
29. Morris GA, Freeman R. Enhancement of Nuclear Magnetic-Resonance Signals by Polarization Transfer. J Am Chem Soc 1979;**101**:760-762.
30. Davis AL, Estcourt G, Keeler J, Laue ED, Titman JJ. Improvement of z Filters and Purging Pulses by the Use of Zero-Quantum Dephasing in Inhomogenous B1 and B0 Fields. J Magn Reson 1993;**A 105**:167-183.
31. Shaka AJ, Keeler J, Freeman R. Evaluation of a New Broad-band Decoupling Sequence - WALTZ-16. J Magn Reson 1983;**53**:313-340.
32. Le Belle JE, Harris NG, Williams SR, Bhakoo KK. A comparison of cell and tissue extraction techniques using high-resolution 1H-NMR spectroscopy. NMR Biomed 2002;**15**(1):37-44.
33. Peeling J, Sutherland G. High-resolution 1H NMR spectroscopy studies of extracts of human cerebral neoplasms. Magn Reson Med 1992;**24**(1):123-136.
34. Sutton L, Wehrli S, Gennarelli L, Wang Z, Zimmerman R, Bonner K, Rorke L. High-resolution 1H-magnetic resonance spectroscopy of pediatric posterior fossa tumors in vitro. J Neurosurg 1994;**81**(3):443-448.
35. Kinoshita Y, Yokota A. Absolute concentrations of metabolites in human brain tumors using in vitro proton magnetic resonance spectroscopy. NMR Biomed 1997;**10**(1):2-12.
36. Ronen SM, Leach MO. Imaging biochemistry: applications to breast cancer. Breast Cancer Res 2001;**3**(1):36-40. 37: Moore CM, et al. Choline, myo-inositol and moo...[PMID:11249799]Related Articles, Links.
37. Leach MO, Verrill M, Glaholm J, Smith TA, Collins DJ, Payne GS, Sharp JC, Ronen SM, McCready VR, Powles TJ, Smith IE. Measurements of human breast cancer using magnetic resonance spectroscopy: a review of clinical measurements and a report of localized 31P measurements of response to treatment. NMR Biomed 1998;**11**(7):314-340.
38. Podo F. Tumour phospholipid metabolism. NMR Biomed 1999;**12**(7):413-439.
39. Bhujwalla ZM, Aboagye EO, Gillies RJ, Chacko VP, Mendola CE, Backer JM. Nm23-transfected MDA-MB-435 human breast carcinoma cells form tumors with altered phospholipid metabolism and pH: a 31P nuclear magnetic resonance study in vivo and in vitro. Magn Reson Med 1999;**41**(5):897-903.
40. Lehtimaki KK, Valonen PK, Griffin JL, Vaisanen TH, Grohn OH, Kettunen MI, Vepsalainen J, Yla-Herttuala S, Nicholson J, Kauppinen RA. Metabolite changes in BT4C rat gliomas undergoing ganciclovir-thymidine kinase gene therapy-induced

programmed cell death as studied by 1H NMR spectroscopy in vivo, ex vivo, and in vitro. J Biol Chem 2003;**278**(46):45915-45923.

41. Lei H, Zhu XH, Zhang XL, Ugurbil K, Chen W. In vivo 31P magnetic resonance spectroscopy of human brain at 7 T: an initial experience. Magn Reson Med 2003;**49**(2):199-205.
42. Ernst M, Griesinger C, Ernst RR. Optimized Heteronuclear Cross Polarization in Liquid. Mol Phys 1991;**74**:219-252.

Figure Legends:

Figure 1. Molecular structures of choline, phosphocholine (PC), and glycerophosphocholine (GPC). The ^{31}P edited ^{1}H experiment discussed in the text selectively refocuses the scalar couplings between the $^{1}CH_2$ and $^{2}CH_2$ protons during the INEPT transfers.

Figure 2. The pulse sequence used to acquire the ^{31}P edited ^{1}H spectra. For the ^{1}H and ^{31}P channels, solid rectangles correspond to 90° radiofrequency pulses, hollow rectangles correspond to 180° pulses, and Gaussian shapes represent selective 180° pulses. The spin-lock pulse is denoted by "SL". The phase of all the pulses is *x* unless indicated otherwise.

Figure 3. 300 MHz ^{1}H spectra for samples of choline, PC, and GPC. These spectra were acquired with ^{31}P decoupling. The lack of resolution in the methyl region (3.3 – 3.1 ppm) makes it hard to quantitatively interpret the integrals of the methyl peaks to determine the concentrations of the three constituents. The solvent consisted of 90%/10% H_2O/D_2O, and the concentrations of GPC, PC, and choline in the samples (in mM) are indicated by the numbers to the left of each spectrum. From downfield to upfield, the peaks correspond to the $^{1}CH_2$, $^{2}CH_2$, and methyl protons. The additional GPC peaks at 3.9 ppm and overlapping the $^{2}CH_2$ resonances at 3.65 and 3.6 ppm arise from the glycerol moiety. Note that the methyl region is not shown to scale with respect to the rest of the spectrum: the vertical scale reduced by a factor of 10 and the horizontal scale expanded by a factor of 3.

Figure 4. ^{31}P edited ^{1}H spectra acquired with ^{31}P decoupling (left) and ^{31}P spectra acquired with ^{1}H decoupling (right). The spectra highlight the benefit in signal-to-noise that the ^{31}P edited ^{1}H experiment has relative to directly acquired ^{31}P spectra. Each spectrum was acquired with 16 scans and the same total experiment time (3 minutes) on a 300 MHz spectrometer. The solvent consisted of 90%/10% H_2O/D_2O and the concentrations of GPC, PC, and choline in the samples (in mM) are indicated by the numbers to the left of each spectrum. The efficient filtration of choline, PC, and GPC signals other than the desired PC and GPC $^{1}CH_2$ protons is readily apparent in the ^{31}P edited ^{1}H spectrum; even the intense methyl peaks at 3.2 ppm are reduced to below the noise level of the spectrum. The artifact visible around 4.7 ppm in the ^{31}P edited ^{1}H spectrum is the residual water signal and has an integral close to zero.

Figure 5. The concentration of the choline-compounds determined using the ^{31}P edited ^{1}H spectra versus the regular ^{1}H spectra for standard samples (top) and brain extract samples (bottom) at 600 MHz. The standard samples consisted of 0 – 10 mM of PC, GPC, and choline in D_2O. The brain extract samples are as described in the text. From left to right, the graphs show the correlation for the concentrations of choline, PC, GPC, as well as for the total concentration of all three choline-compounds. For the results corresponding to the ^{31}P edited spectra, the estimated concentrations of PC and GPC were determined by dividing the peak intensity in the ^{31}P edited spectra by the transfer efficiency. The choline concentration was estimated by taking the integral of all three methyl resonances in the regular ^{1}H spectra and subtracting the PC and GPC contributions as described in the text. For the results determined from the regular ^{1}H experiments, the concentrations determined

for the standard samples were determined by integrating the ${}^{1}CH_2$ protons. For the brain extract samples, this was not possible due to spectral overlap. Instead, the concentrations of the individual components were determined by fitting the methyl resonances. For both sets of samples, the total choline concentrations were determined by summing the concentrations of the three choline compounds. The dotted lines indicate the results from linear regression analyses of the data; the result of each analysis is shown with the relevant graphs.

Figure 6. 600 MHz regular (a) and ${}^{31}P$ edited ${}^{1}H$ (c) spectra obtained for a human glioma extract sample. Spectrum (b) highlights two regions of the regular spectrum with the scale increased by a factor of four. The scale of the ${}^{31}P$ edited ${}^{1}H$ spectrum is increased by a factor of forty relative to spectrum (a). Peaks other than those from PC and GPC in the ${}^{31}P$ edited ${}^{1}H$ spectrum can arise from other phosphorous containing compounds in the samples such as adenosine monophosphate, phosphoethanolamine and glycerophosphoethanolamine.

Figure 1.

Choline

$$(CH_3)_3\overset{+}{N}-{}^2CH_2-{}^1CH_2-OH$$

Phosphocholine (PC)

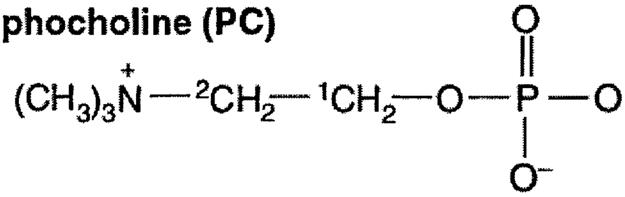

$$(CH_3)_3\overset{+}{N}-{}^2CH_2-{}^1CH_2-O-\underset{\underset{O^-}{|}}{\overset{\overset{O}{\|}}{P}}-O$$

Glycerophosphocholine (GPC)

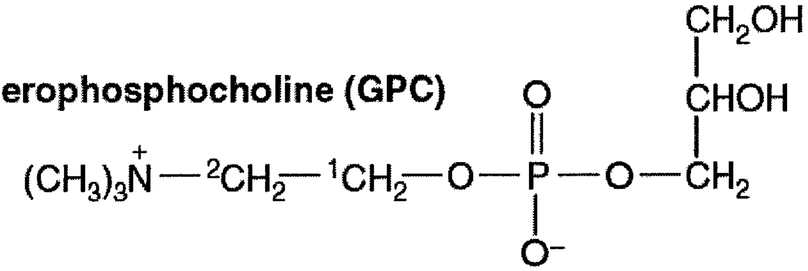

$$(CH_3)_3\overset{+}{N}-{}^2CH_2-{}^1CH_2-O-\underset{\underset{O^-}{|}}{\overset{\overset{O}{\|}}{P}}-O-\overset{\overset{\overset{CH_2OH}{|}}{\overset{CHOH}{|}}}{CH_2}$$

Figure 2.

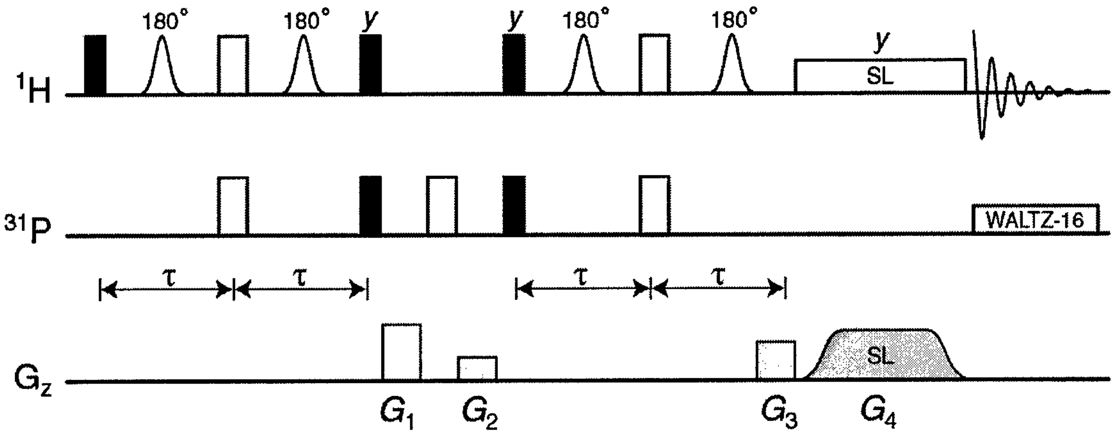

Figure 3.

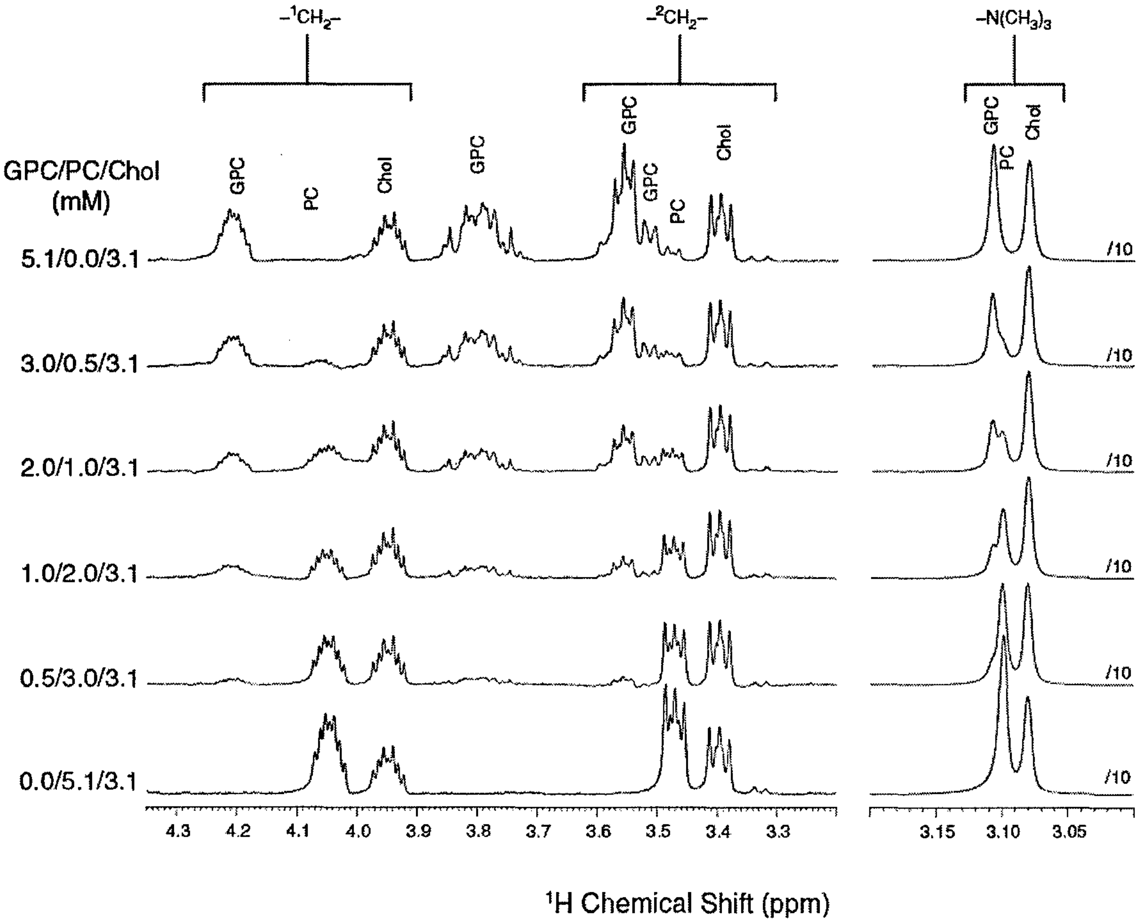

$-^1CH_2-$
$-^2CH_2-$
$-N(CH_3)_3$
GPC/PC/Chol (mM)
GPC
PC
Chol
GPC
GPC
GPC
PC
Chol
GPC
PC
Chol
5.1/0.0/3.1
3.0/0.5/3.1
2.0/1.0/3.1
1.0/2.0/3.1
0.5/3.0/3.1
0.0/5.1/3.1
/10
/10
/10
/10
/10
/10
4.3
4.2
4.1
4.0
3.9
3.8
3.7
3.6
3.5
3.4
3.3
3.15
3.10
3.05
^1H Chemical Shift (ppm)

Figure 4.

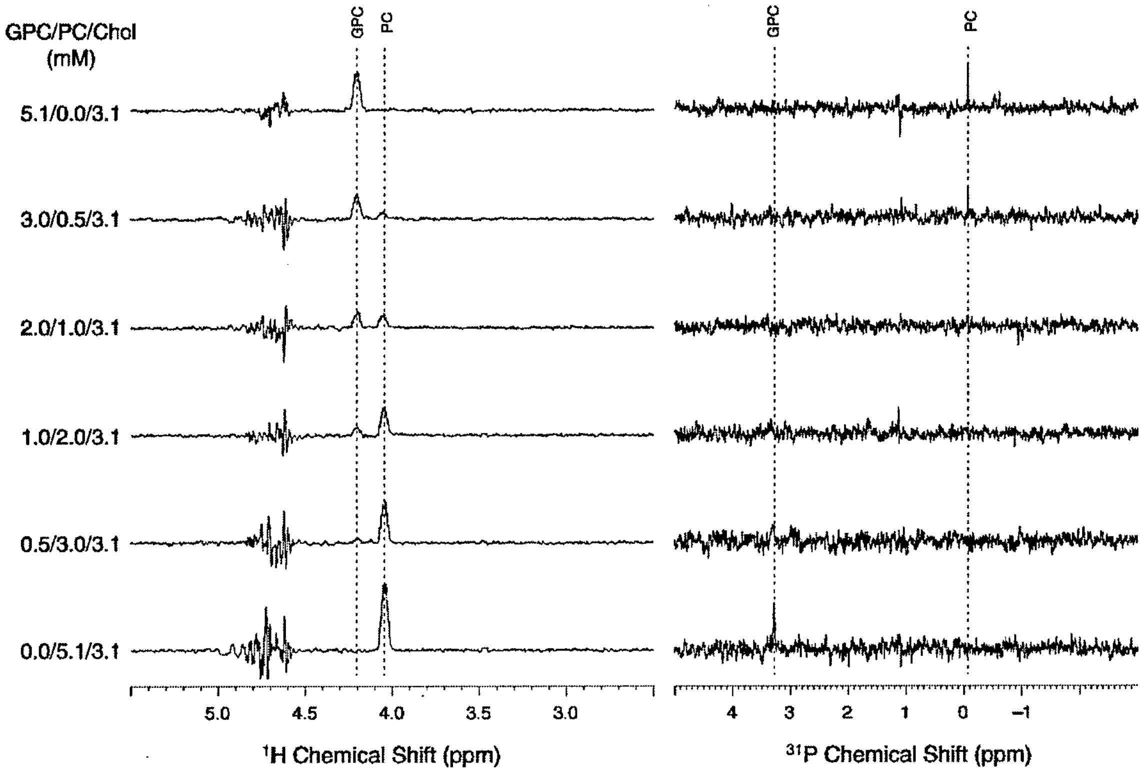
GPC/PC/Chol
(mM)
5.1/0.0/3.1
3.0/0.5/3.1
2.0/1.0/3.1
1.0/2.0/3.1
0.5/3.0/3.1
0.0/5.1/3.1
GPC
PC
GPC
PC
5.0
4.5
4.0
3.5
3.0
^{1}H Chemical Shift (ppm)
4
3
2
1
0
–1
^{31}P Chemical Shift (ppm)

Figure 5.

Standard Samples

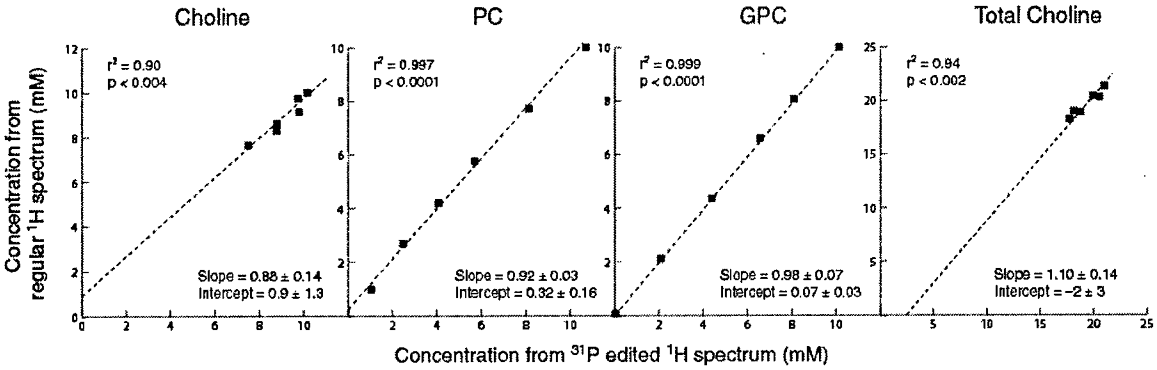

Brain Extract Samples

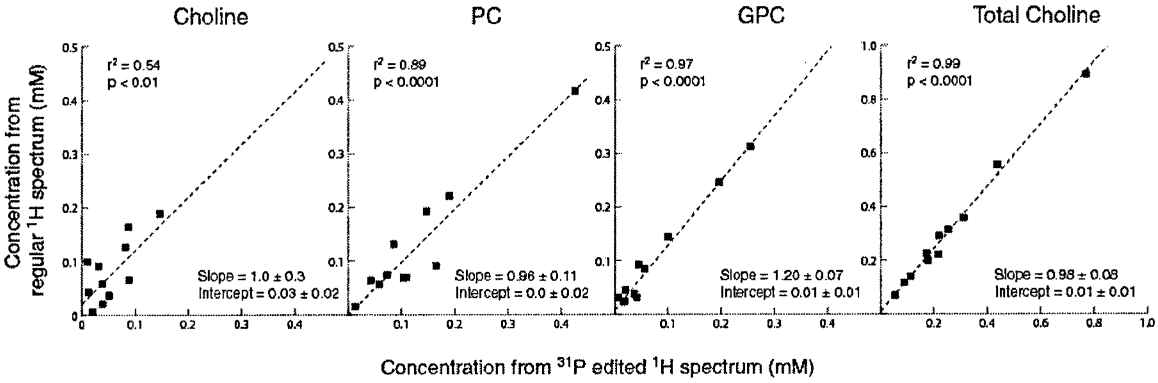

Figure 6.

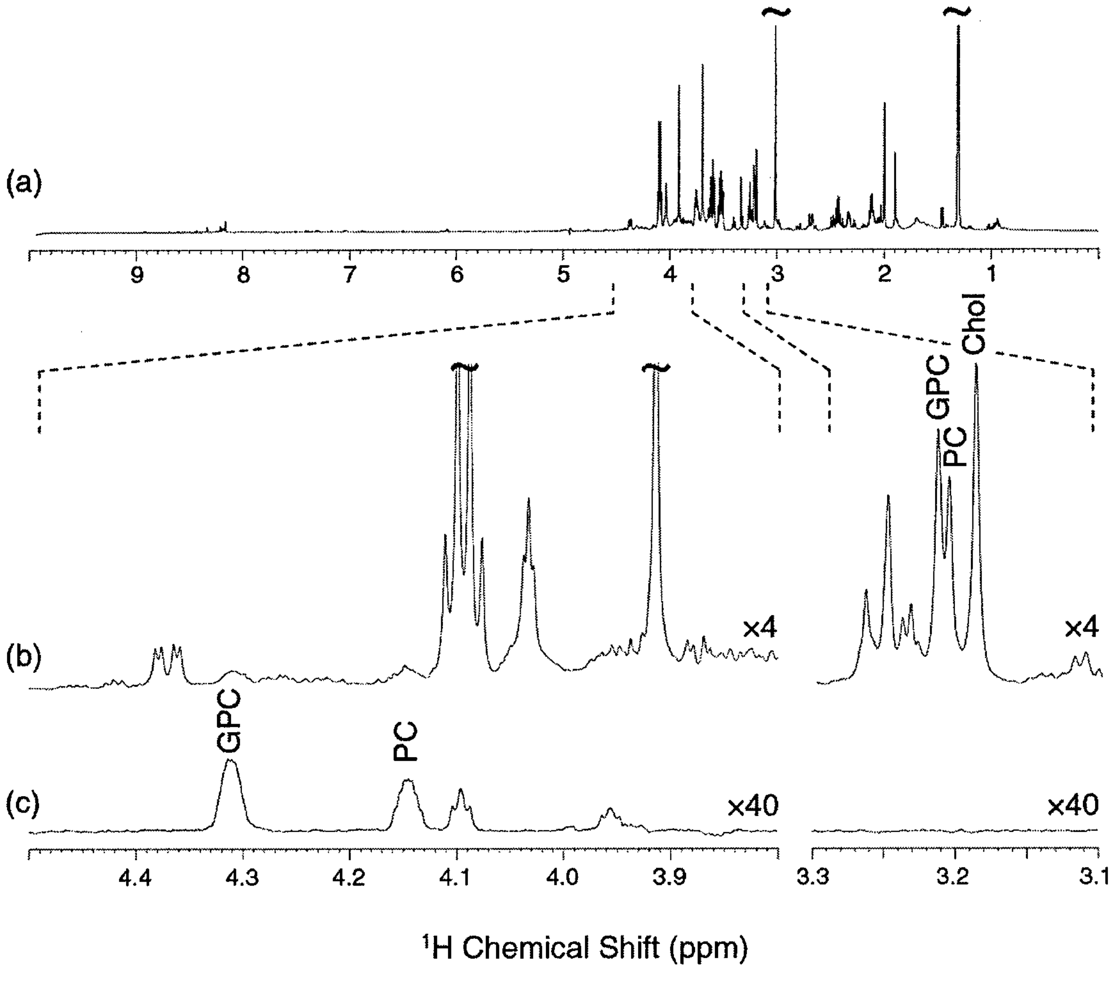

(a)
9
8
7
6
5
4
3
2
1
(b)
GPC
PC
Chol
×4
×4
(c)
GPC
PC
×40
×40
4.4
4.3
4.2
4.1
4.0
3.9
3.3
3.2
3.1
^{1}H Chemical Shift (ppm)